MICROELECTROMECHANICAL SYSTEM BASED PLATFORMS FOR MICROFLUIDIC AND SENSING APPLICATIONS

A Dissertation

by

ZHEYUAN CHEN

Submitted to the Graduate and Professional School of
Texas A&M University
in partial fulfillment of the requirements for the degree of

DOCTOR OF PHILOSOPHY

Chair of Committee,	Jun Kameoka
Committee Members,	Jun Zou
	Kamran Entesari
	Mike McShane
Head of Department,	Miroslav Begovic

December 2021

Major Subject: Electrical Engineering

ABSTRACT

Emerging microelectromechanical system (MEMS) based platforms show great prospects in bio-MEMS applications recently. Three platforms were proposed and demonstrated based on polymer, paper, and hydrogel substrates for microfluidic and sensing applications.

A size-selective microfluidic platform (ExoSMP) based on polydimethylsiloxane (PDMS) for EV isolation was proposed based on nanomembrane filtration and hydrodynamic properties of the particles. The isolation efficiency was investigated at different sample flow rates and demonstrated a high recovery rate of 94.2% and high reproducibility at an optimal sample flow rate with short processing time. Isolation of EV subpopulations were also demonstrated by altering the pore sizes of membrane filters. ExoSMP shows great potential in investigating the role of EVs in various point-of-care applications in disease monitoring, medical diagnosis, and drug delivery.

A low-cost and enzyme-free paper sensing platform was proposed and developed based on molecular imprinted polyaniline (MIP-PANI) electrode by a one-step synthesis method by co-polymerization of the aniline monomer with the template on paper. The sensing electrode with target binding sites and the signal-transducing electrode were created at the same time by MIP-PANI. Glucose concentration was determined in both aqueous and bovine blood solutions by the impedance change to evaluate the performance of the PANI paper sensors. This simple paper sensing platform provides low-cost and reliable chemical/biomarker analysis access to various applications such as disease diagnostics and environmental monitoring, especially in underserved communities.

A multiplexed barcode hydrogel platform was proposed with four discrete compartments containing two types of oxygen and glucose sensing domains to demonstrate multiplexed optical sensing. The fabrication process was developed and optimized for low-cost and mass production by soft lithography and molding. Multiplexed oxygen and glucose response test were characterized by phosphorescent lifetime change of the sensing assays and it demonstrated minimal crosstalk between the nearby oxygen and glucose responsive compartments. The barcode hydrogel sensors were exposed to 10 consecutive cycles of 0 mg/dL glucose and 200 mg/dL glucose and demonstrated a good glucose response stability. This multiplexed and implantable barcode hydrogel platform has great potential in the diagnosis, monitoring, management, and treatment of various pathological conditions and can be a valuable tool in personalized medicine.

DEDICATION

This dissertation is dedicated to my parents and family for their support and love throughout my life.

ACKNOWLEDGEMENTS

I would like to thank my advisor, Dr. Jun Kameoka, for his guidance and support throughout my doctoral studies. I also would like to thank my committee members, Dr. Mike McShane, Dr. Jun Zou, and Dr. Karman Entesari for their valuable guidance and support on my research.

I would like to express my warm and sincere gratitude to all my lab buddies for their help and friendship during my research. I would also like to thank my collaborators from other departments and universities.

I wish to extend my gratitude to the department staff and faculty members that helped me. I also would like to thank the staffs at AggieFab Nanofabrication Facility, Microscopy Imaging Center (MIC) and Materials Characterization Facility (MCF), who provided helpful training and suggestions during my experiments.

I wish to thank my family for encouraging and supporting me. I will always cherish their courage and love throughout my life.

CONTRIBUTORS AND FUNDING SOURCES

Contributors

This work was supervised by a thesis dissertation committee consisting of Professor Jun Kameoka, and Professor Jun Zou and Professor Karman Entesari of the Department of Electrical and Computer Engineering, and Professor Mike McShane of the Department of Biomedical Engineering.

The EV preparation and western blot in chapter 2 was conducted by Dr. Yi Yang of The University of Texas MD Anderson Cancer Center. The microparticles and lifetime response test in chapter 4 were provided by Tokunbo Falohun of the Department of Biomedical Engineering at Texas A&M University.

All other work conducted for the dissertation was completed by the student independently.

Funding Sources

Graduate study was supported by a research assistantship from Texas A&M University, College Station.

This work was also made possible in part by Bill and Melinda Gates Foundation under Grant Number OPP1199456, and by National Science Foundation (NSF) The Precise Advanced Technologies and Health Systems for Underserved Populations (PATHS-UP) Engineering Research Center (ERC) under Grant Number 1648451.

NOMENCLATURE

IC	Integrated Circuits
MEMS	Microelectromechanical Systems
EV	Extracellular Vesicles
PDMS	Polydimethylsiloxane
PC	Polycarbonate
UV	Ultraviolet
DLS	Dynamic Light Scattering
NTA	Nanoparticle Tracking Analysis
SEM	Scanning Electron Microscopy
WB	Western Blot
RT	Room Temperature
MIP	Molecular Imprinting
PANI	Polyaniline
CRP	C-Reactive Protein
MMA	Methylmalonic Acid
LOD	Limit of Detection
PEGDA	Poly(ethylene glycol) diacrylate

TABLE OF CONTENTS

Page

LIST OF FIGURES

Page

LIST OF TABLES

Page

1. INTRODUCTION

1.1. Development of MEMS and BioMEMS

Since the early 1960s, the fabrication techniques developed for standard silicon integrated circuits (IC) processing have been extended to fabricate nontraditional silicon devices. Based on the advantages of semiconductor processing, the advent of microelectromechanical system (MEMS) has enabled dramatic changes in diverse technological areas.[1] In the late 1980s, MEMS techniques were applied to precise control and manipulation of fluids that are geometrically constrained to a small scale,[2] which leads to great prospects of biomedical microelectromechanical system (BioMEMS). In terms of control and distribution of fluids and gases, MEMS-based devices offer great opportunities to achieve improved device performance, high levels of integration, at lower cost, with decreased size and increased reliability.[1] Various BioMEMS applications mainly consisting of lab-on-a-chip (LOC) and micro total analysis systems (μTAS) have been developed. LOC is concerned with miniaturization and integration of lab processes and experiments into a single chip/platform, which often can be extended to specific applications such as microarrays, organ-on-a-chip, lab-on-your-palm, and lab-in-your-wrist platforms.[3] Similarly, μTAS are usually applied to various chemical analysis, such as single cell detection, molecular diagnostics, and point-of-care diagnostics.[4]

1.2. Overview of Fabrication Techniques

Traditional MEMS fabrication processing includes lithography, physical vapor deposition, chemical vapor deposition, wet etching, dry etching, and bonding takes advantage of the same techniques that are widely used in semiconductor industries for mass production.

Lithographic processes are widely used for nano/micro structure fabrication, followed by etching steps and then sealing or bonding processes of the patterned substrate to a cover layer.[5] The dimension of the channel is lithographically defined by the pattern of resist. For microstructures such as microchannels, micropillars, and microgrooves, photolithography is commonly used to create micron patterns. However, this process generally requires high resolution lithography techniques such as e-beam lithography,[6] proton-beam lithography,[7] X-ray lithography,[8] and extreme ultraviolet lithography[9, 10] for submicron or nano structure manufacturing.

Etching is an essential step to transfer the lithographic pattern on the resist to a substrate such as silicon or fused silica. The height of a microstructure is generally controlled by the parameters of the recipe during etching. Wet etching and dry etching are the two major types of etching techniques.[11] The advantages of wet etching are simple, relative fast, high etch rate, and high selectivity. However, wet etching is generally isotropic, which means the etchant chemicals remove substrate materials under the mask material at the same rate.[12] Dry etching often refers to plasma etching. Unlike wet etching, the dry etching process typically etches directionally or anisotropically. [13] Common types of dry etching are reactive ion etching (RIE) and ion milling. The advantages of dry etching include creating high aspect ratio structures and particularly useful for materials that are chemically resistant and could not be wet etched.

Sealing or bonding steps are used to enclose the etched structure including holes, wells, trenches and so on. Many approaches have been developed to achieve a seal, such as adhesive bonding, anodic bonding, eutectic bonding, and fusion bonding.[14] The substrate material is the key factor to determine the sealing method. Adhesive bonding is widely used to bond various materials including polymers, adhesives, epoxies and UV curable compounds.[15] Anodic bonding is often

used to bond silicon and ionic glass substrates.[16] Eutectic bonding is specifically applied to bond materials to form eutectic compound.[17] Fusion bonding is a common approach to bonding silicon, silica, quartz, compound semiconductors, as well as oxide materials.[18]

Other techniques such as physical vapor deposition, chemical vapor deposition, ion implantation and annealing are also widely used in MEMS-based device fabrication, depending on the need and application. Common types of physical vapor deposition include sputtering, e-beam evaporation and pulse-laser deposition. Common types of chemical vapor deposition include plasma enhance chemical vapor deposition, low pressure chemical vapor deposition, and atomic-layer chemical vapor deposition.

Recently, MEMS-based technology has broadened their applications in various fields, such as civil engineering, materials engineering, chemical engineering, neuron science, tissue engineering, biology and medicine. Much attention has been attracted in multidisciplinary applications, especially in biomedical and healthcare areas, which often needs electrical, material, mechanical, chemical, optical, and biomedical knowledges to develop low cost and high accurate MEMS-based integrated platforms to solve various biomedical issues.

Apart from the conventional approaches that are suitable for patterning, etching and bonding bulk inorganic substrate materials such as silicon and glasses, many methods suitable for organic substrate materials have been developed and widely used in BioMEMS applications such as microfluidics chips, molecular analysis, and miniaturized sensors. Polymers, papers, and hydrogels are among the most used types of substrate materials.

Polymer-based microfluidics was introduced in the 1980s and viewed as the second birth of MEMS technology, compared to conventional MEMS-based devices using silicon and glass substrates, such as micromotors, micropumps and microvalves. The wide variety of polymers

grants great flexibility in choosing a suitable substrate material for specific applications. Polymers offer attractive advantages as they are easy to access, usually cost efficient, and with good overall physical properties and biocompatibility.[19] Various polymers can be used to build chips, such as polydimethylsiloxane (PDMS),[20] polymethylmethacrylate (PMMA),[21] polystyrene (PS),[22] polycarbonate (PC),[23] and polyvinyl chloride (PVC).[24]

PDMS is the material of choice for fast prototyping, and thus it is commonly used in laboratories, especially in the academic field. The most popular fabrication method for fabricating PDMS chip is soft lithography. In this approach, a PDMS prepolymer solution is mixed with a curing agent to crosslink the polymer. The hardness of the final product is determined by the ratio of the curing agent. Normally, a prepolymer to a curing agent ratio of 1:10 is used. The whole precursor solution is subsequently cast onto a master mold and then placed in an oven to allow crosslinking. Many methods are available to produce the master mold such as conventional photolithography, three-dimensional (3D) printing, and two-photon polymerization. Once cured, open channels are obtained by the pattern transferred from the master mold and the PDMS can be easily peeled off from the master mold. Finally, the PDMS needs to be bonded to another surface to form enclosed channels, such as glass or PDMS itself. This is usually done by performing an oxygen plasma treatment on the surfaces to be bonded.

Paper, as one of the cheapest materials, is widely studied and used in microfluidic and sensor applications. For instance, commercially pregnancy test kits work by having a slip of paper that reacts by changing color when human chorionic gonadotropin (HCG) is present. Many methods have been developed for paper-based microfluidics and sensors including wax printing, inkjet printing, flexographic printing, screen printing, paper cutting, and even photolithography.[25, 26] Most fabrication methods are relatively simple, flexible, convenient and low cost. Wax printing

is commonly used for paper-based microfluidic devices. In a wax printing process, a filter paper is patterned with microchannels using a wax printer, or simply by a wax pen and a template ruler. The patterned paper is subsequently placed in an oven, causing the wax to melt and penetrating the paper, hence forming the hydrophilic channel areas confined by the hydrophobic wax walls.[27] The microchannel made of paper can act as passive pump dispenser without the need of external power components.[28] Paper-based microfluidic devices are promising in portable and low-cost personalized diagnostics, especially for unrepresented populations and underserve communities.

Hydrogels 3D hydrophilic polymer networks that can swell in water and hold a large amount of water while maintaining the structure due to chemical or physical cross-linking of individual polymer chains.[29] Several methods have been developed for the patterning and integration of hydrogels including a soft lithography-based approach with sacrificial or reusable templates, photopolymerization, and local integration.[30] Over the past decades, various hydrogels, such as agarose, Matrigel, poly(ethylene glycol) diacrylate (PEGDA), alginate, and gelatin methacryloyl (GelMA), have been frequently used for different applications such as microfluidic devices, implantable/insertable sensors, and tissue engineering. The reusable template refers to the master mold in the soft lithography-based approach, which can be produced by conventional lithography methods or 3D printing. In the photopolymerization method, a ultraviolet (UV) light is used to construct gel structures by crosslinking with high spatial resolution.[31] High spatial resolution and high aspect ratio features can be achieved using this method.[32] In the local integration method, the creation of gel structures is performed in a microfluidic device.[33, 34] Due to the laminar nature of flow in microfluidic systems, various gels can be co-polymerized in the same microchannel.

1.3. Significance of Research

MEMS-based platforms offer numerous advantages over conventional experimental and analytical devices. MEMS-based platforms often have extremely low sample consumption. Due to the low internal micro/nano channel volume, the use of fluid sample is therefore reduced to microliter or even smaller. This could bring a huge benefit to the applications with expensive samples or volume-limited samples. MEMS-based platforms also enable LOC with automated and fast operation. Multi-functional devices can be integrated on a single chip. Hence, sample preparation, reaction, sample analysis, and waste collection can be done sequentially. Additionally, MEMS-based platforms can improve signal-to-noise ratio, sensitivity and stability. Finally, using industrial fabrication and assembling techniques make it simple for future mass production consideration with low cost.

In this dissertation, three types of MEMS-based platforms using PDMS, paper, and hydrogel substrates were proposed and demonstrated for various applications. Firstly, a size selective microfluidic platform for EV isolation is introduced in chapter 2. High particle recovery and yield with specific size were achieved by this automated, rapid, and reliable platform. Secondly, a low-cost and enzyme-free paper-based sensing platform is introduced in chapter 3. Various biomarkers detection was demonstrated by this cost-effective disposable paper sensor paltform. Thirdly, a barcode hydrogel platform for multiplexed optical sensing is introduced in chapter 4. A multiplexed an implantable barcode hydrogel platform was developed and demonstrated for continuous oxygen and glucose monitoring. Finally, summaries of the studies of these three platforms are concluded and the future plans are pointed out in chapter 5.

2. SIZE SELECTIVE MICROFLUIDIC PLATFORM*

2.1. Introduction

2.1.1. Significance of Extracellular Vesicles Isolation

Among translational and clinical researchers, there is significant interest in extracellular vesicles (EVs) as potential diagnostic biomarkers and therapeutic vehicles that can be fast-tracked to clinical evaluation and precision medicine applications.[35, 36] EVs refer to a heterogenous population of particles with lipid bilayer membranous structures that hold information in the form of proteins, lipids, or nucleic acids, thereby physiologically and pathologically influencing the intercellular communication of both the recipient and parent cells.[37] EVs are released by most viable cells. These particles can be isolated and collected from various bodily fluids such as blood, saliva, urine, lymph, and milk. The existing criteria adopted to discriminate among the subpopulations are based on size, density, function, and molecular cargo.[38]

In the past decades, there are at least three main subgroups that have been identified and termed as: exosomes, microvesicles and apoptotic bodies.[39, 40] The physical properties of EVs contribute to distinct biological functions and organ distribution patterns. A unique cancer-derived EV population was recently identified and termed as "large oncosomes", due to their atypical size. They transport oncogenic material and are more specific to cancer cells.[41] Exosomes are nano-

* Part of this chapter is reprinted with permission from "Isolation of cancer-derived extracellular vesicle subpopulations by a size-selective microfluidic platform" by Chen, Z., Yang, Y., Yamaguchi, H., Hung, M. C., Kameoka, J., 2020. *Biomicrofluidics*, 14 (3), 034113. Copyright 2020 by American Institute of Physics. "Development of size-selective microfluidic platform" by Chen, Z., Yamaguchi, H., Kameoka, J., 2019. *Annu Int Conf IEEE Eng Med Biol Soc*, *2019*, 5661-5664. Copyright 2019 by Institute of Electrical and Electronics Engineers.

sized populations of EVs that are released by most viable cells. Two exosome subpopulations were recently identified as large exosome vesicles (Exo-L, 90-120 nm) and small exosome vesicles (Exo-S, 60-80 nm), and a population of non-membranous nanoparticles was newly discovered and termed "exomeres" (~35nm).[42] Proteomic profiling of these three nanoparticle subsets has revealed that each subgroup contains unique protein cargoes. These proteins participate in different signaling pathways and have distinct biological functions.[42] Increasing evidence has revealed the underlying heterogeneous nature of exosomes within intensively distinct particulate secretomes.[43] EVs display a diverse range of sizes in terms of diameter, but the terms of exosomes and microvesicles tend to cause inaccuracy and confusion by both manifold.

Therefore, the three main subgroups of EVs can be categorized and named based on size and in this chapter: small EVs (< 120 nm, sEVs), medium EVs (120 nm-200 nm, mEVs) and large EVs (> 200 mm, lEVs). Tremendous attention has recently been focused on sEVs, which play a vital role in tumorigenesis, tumor microenvironments, cancer metastasis, and chemotherapeutic resistance.[42, 44, 45] Thus, the molecular properties and cargo information of various subpopulations of EVs must be dissected in order to investigate their clinical potential as diagnostic, prognostic, and therapeutic candidates in liquid biopsies.

2.1.2. Conventional Isolation Methods

To unravel the mystery of EVs, several conventional approaches have been developed such as ultracentrifugation (UC),[46-48] precipitation,[49-51] and membrane filtration,[52-54] and immunoaffinity-based separation.[55]

UC is currently the most common approach for isolating EVs. This gold standard method differentiates among sizes with a sequence of centrifugations from low to high rotation speeds.

The key barriers to implementing this approach in a clinical setting are the lengthy operating time (more than 5 h), low EV recovery, purity, and reproducibility, and poor specifications. There is also evidence that the high centrifugal force (100,000 to 200,000 g) can cause EV fusion and coagulation, and may damage their structure, properties, and function.[56, 57]

Precipitation approaches have drawbacks such as small sample volumes and low purity. The polymer matrix used for precipitation can influence the biological activity of the EVs. Therefore, precipitation approaches have some difficulty in isolating intact EVs for cancer research and biomarker discovery.[49, 50]

Membrane filtration method usually utilizes multiple nanoporous membrane filters to separate EVs by the pore size. The challenges accompanying membrane-based filtration include difficulties with operation optimization, low specificity, and poor reproducibility due to membrane fouling.[58]

A major drawback of immunoaffinity-capturing based method is the low yield due to limitations in specific EV-antibody interactions.[55] This approach also requires pre-treatment and lengthy processing times.

Size-selective EV isolation has also been demonstrated by the asymmetric flow field-flow fraction (AF4) method[42] and multiple nanomembrane filter devices.[59] These two approaches have been proven to further isolate EV subgroups based on size. However, the equipment for AF4 is expensive, not user friendly, and bulky, and the method requires a lengthy processing time. The drawback of multiple nanomembrane filtration is the irregular liquid pressure distribution through five nanomembranes (the first to fifth membrane pressure applications are not same), which reduces reproducibility.

Other approaches such as nanowire trapping,[60, 61] acoustic separation,[62, 63] lateral displacement,[64, 65] viscoelastic flow separation,[66] electrophoretic separation,[67] and dielectrophoretic separation[68] have been implemented. However, these methods are unable to efficiently separate EVs based on the size of the subpopulation and suffer from limitations such as additional reagents/labels, pre-treatment steps, lengthy processing times, low reproductivity, low EV recovery and low purity.

In this chapter, EV isolation on a single size-selective microfluidic platform (ExoSMP) that targets an automated, consistent, and reliable isolation method was reported.[69] This method is based on a size-selective process accomplished via nanomembrane filtration and the hydrodynamic properties of nanoparticles. This unique platform enables the identification and harvesting of size-specific EVs (i.e., sEVs and mEVs) with the additional advantage of being label-free and featuring low cost, short processing times, and convenient integration with other on-chip technology and downstream analysis. In this work, intact sEV isolation based on size from mEVs, lEVs, proteins, and other bio-fragments was firstly demonstrated with a short processing time of less than one hour. Then, isolation of subpopulations of EVs was investigated by simply altering the pore sizes of nanomembrane filters. Quantitative analysis of the isolated EVs by nanoparticle tracking analysis (NTA) was shown to confirm high recovery from the cancer cell derived EVs.

2.2. Design and Working Principle

As shown in Figure 1 and 2, the microfluidic platform consists of three horizontally aligned polydimethylsiloxane (PDMS) microchannels and two polycarbonate (PC) nanoporous membranes (with the pore sizes of 30 and 100 nm) sandwiched between the microchannels. A through-hole is punched in the center microchannel to form an enlarged fluid exchange area

through the top to the bottom microchannels. Gold electrodes are connected to the top and bottom microchannels to induce the electrophoretic force through the two nanoporous membranes. An optical image of the microfluidic platform is presented in Figure 1c.

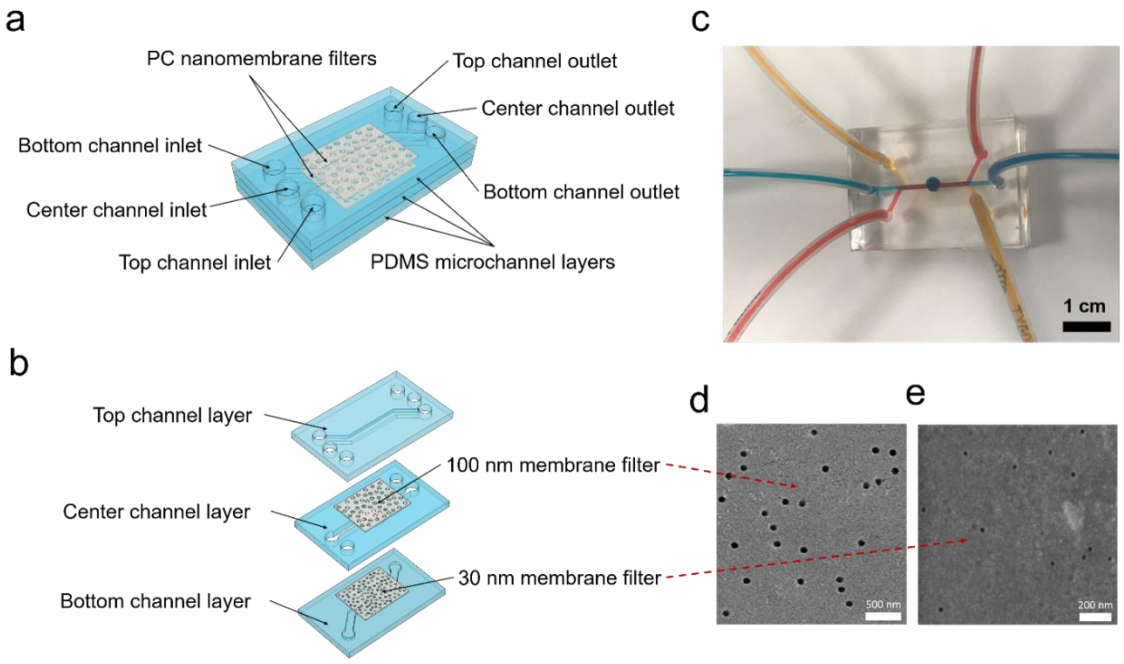

Figure 1 Schematics of the size-selective microfluidic platform device. (a) Schematic diagram of the three-layer microfluidic device. (b) 3D explosive view of the microfluidic device. The nanomembrane filters are sandwiched by three microchannel layers. (c) An optical image of the microfluidic device with 30 and 100 nm membrane filters. Deionized (DI) water with different color dyes was pumped into the top (red), center (blue) and bottom (orange) microchannels, respectively. SEM images of the nanomembrane filters with pore sizes (in diameter): (d) 100 nm and (e) 30 nm.

The scanning electron microscopy (SEM) images of the 30 and 100 nm nanoporous membranes are shown in Figures 1d and e, respectively. The entire sample solution is pumped into the top microchannel (red) through the top inlet, and the extraction buffer solutions (PBS) are pumped into the center (blue) and bottom (yellow) microchannels at optimum flow rates.

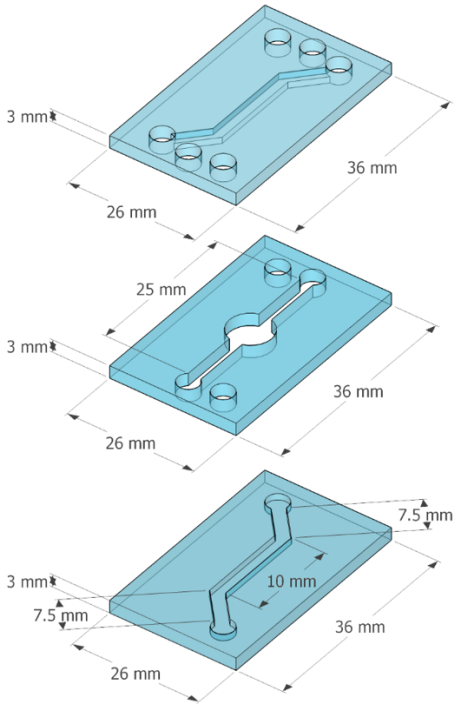

Figure 2 Computer aided design (CAD) layout of the microchannel layers.

The top and bottom microchannels are symmetrically designed. The dimensions of the top, the center and the bottom microchannels are the same with 25 mm in length, 1000 μm in width and 200 μm in height. The inlets, outlets, and through-hole (in the center layer) are 2 mm in diameter. Through-holes are created with 2.5 mm in diameter.

The flow direction in the microchannels is perpendicular to the vertical electrophoretic force acting through the top to bottom microchannels. Less particle fouling can be expected using ExoSMP because the transportation direction of the sample flow and electrophoretic force are perpendicular, as compared to other membrane-filtration approaches.[52-54]

In the present study, there were two perpendicular forces on the particles: fluidic flow and electrophoretic force (see Figure 3). The fluidic flow was induced in the horizontal direction, while

the electrophoretic force was prompted by the applied electric field in a vertical direction. The forward velocity (V_F) was equal to the flow rate of the fluid, while the electrophoretic velocity (V_E) was calculated based on Equation (1) under a laminar flow condition:[70]

$$V_E = \frac{QE}{6\pi\mu R} \quad (1)$$

where Q is the surface charge of the particle, E is the applied electric field, μ is the dynamic viscosity of the fluid, and R is the hydrodynamic radius of the particle. With the applied voltage and fluid, the electrophoretic velocity was therefore inversely proportional to the radius and surface charge of the particle. According to the Grahame equation, the zeta potential of the particle could be converted to the surface charge,[71] as shown in Equation (2):

$$\mathrm{Q} = \frac{\varepsilon \cdot \zeta}{\lambda} \quad (2)$$

where ε is the dielectric constant, and ζ and λ are the zeta potential and Debye screening length, respectively. The zeta potential of the proteins was approximately two times larger than that of the EVs at their maximum.[60, 72, 73] Thus, the most dominant factor for determining the electrophoretic velocity was the hydrodynamic radii of the proteins (5-10 nm) and sEVs (30-100 nm).

Particles of various sizes under fluidic flow have the same forward fluidic velocity (V_F). However, particles with smaller hydrodynamic radii (R) tend to have larger electrophoretic velocity. The variables R_1, R_2, and R_3 represent particles with three different hydrodynamic radii. If $R_1 > R_2 \gg R_3$, we have $V_{E1} < V_{E2} \ll V_{E3}$ according to Equation (1), as shown in Figure 3a. Smaller dimensional particles tend to have faster vertical motion. That is to say, the vertical velocity of the proteins was much faster than that of the EVs under the applied electric field. Moreover, the vertical electrophoretic velocity of the larger EVs was much slower than that of the

smaller EVs and proteins, thereby enabling the proteins and smaller EVs to pass vertically through the nanoporous membrane.

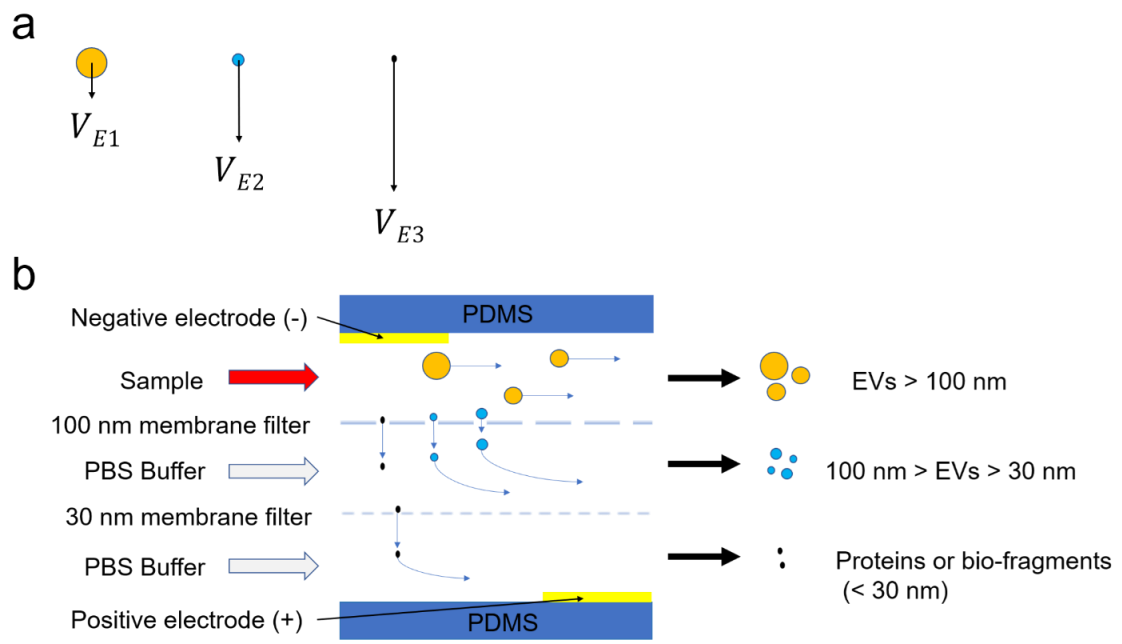

Figure 3 Schematic diagrams for theory and working principle of the ExoSMP device. (a) Negatively charged particles with different dimensions are subject to the electrophoretic force by the applied electric field in vertical direction. They have different vertical velocity profiles due to their dimensions. (b) Working principle of size-selective isolation of EVs using the ExoSMP device with 30 and 100 nm membrane filters in the side view. Schematic particle trajectories are labeled in blue arrows.

The workflow of the EV isolation is shown in Figure 3b. EVs, including sEVs, mEVs and lEVs, are negatively charged particles.[60, 74] ExoSMP can separate particles based on the pore sizes of nanomembrane filters and hydrodynamic properties of the particles. Particles larger than the pore size are retained by the fluidic force in the same microchannel. Negatively charged particles such as apoptotic cells and microvesicles are attracted to the cathode but retained in the top channel outlet due to their dimensions and slow vertical velocity. Positively charged molecules such as certain proteins are retained and attracted to the gold anode electrode located in the top

microchannel. Nanovesicles and negatively charged proteins can pass vertically through the 100 nm nanoporous membrane due to the electrophoretic force. EVs with dimensions between 30 and 100 nm are retained in the center microchannel and collected at the center channel outlet. Negatively charged proteins are quickly guided into the bottom microchannel through the 30 nm membrane filter.[75]

2.3. Device Fabrication and Assembly

2.3.1. Microchannel Layer Fabrication

The microfluidic device consists of three PDMS microchannels and two track-etched nanoporous polycarbonate (PC) membranes (Whatman, GE Healthcare Life Sciences). There are two approaches to the fabrication of the microchannel master molds: photolithography and 3D printing. Photolithography is a conventional IC fabrication process for precise patterning, and 3D printing can be used for micro-size structures with the advantages of easy modifying and fast prototyping.

The fabrication process of the maser mold by photolithography is conducted and illustrated in Figure 4. In brief, SU-8 2075 photoresist (MicroChem) was spin-coated on a silicon wafer. Then, the wafer was soft baked on a hotplate at 65°C. SU-8 photoresist was patterned by photolithographic process as the top-, center-, and bottom- microchannel layer master molds through UV exposure, hard bake, and developing process. The wafer was then hard-baked overnight to improve mechanical properties.

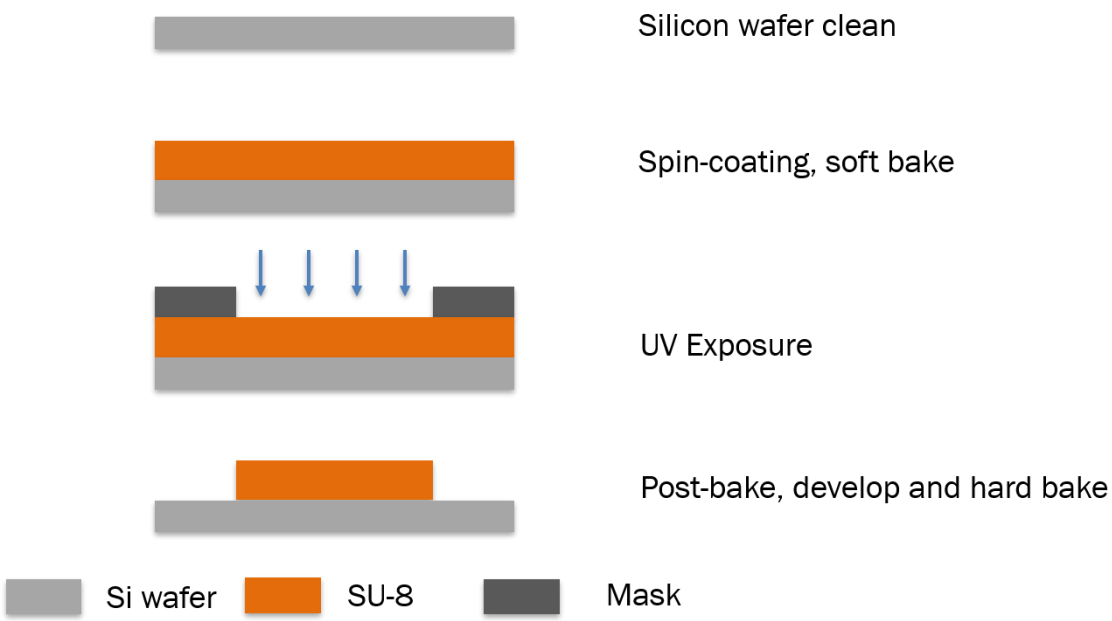

Figure 4 Fabrication process of the master mold by photolithography.

The master mold for each layer can be also simply fabricated by a 3D printer (EnvisionTEC). The layout of each master mold was created by a computer-aid design software. After printing, the printed molds were exposed to UV light for 5 min and cured at 65°C for at least 24 h.

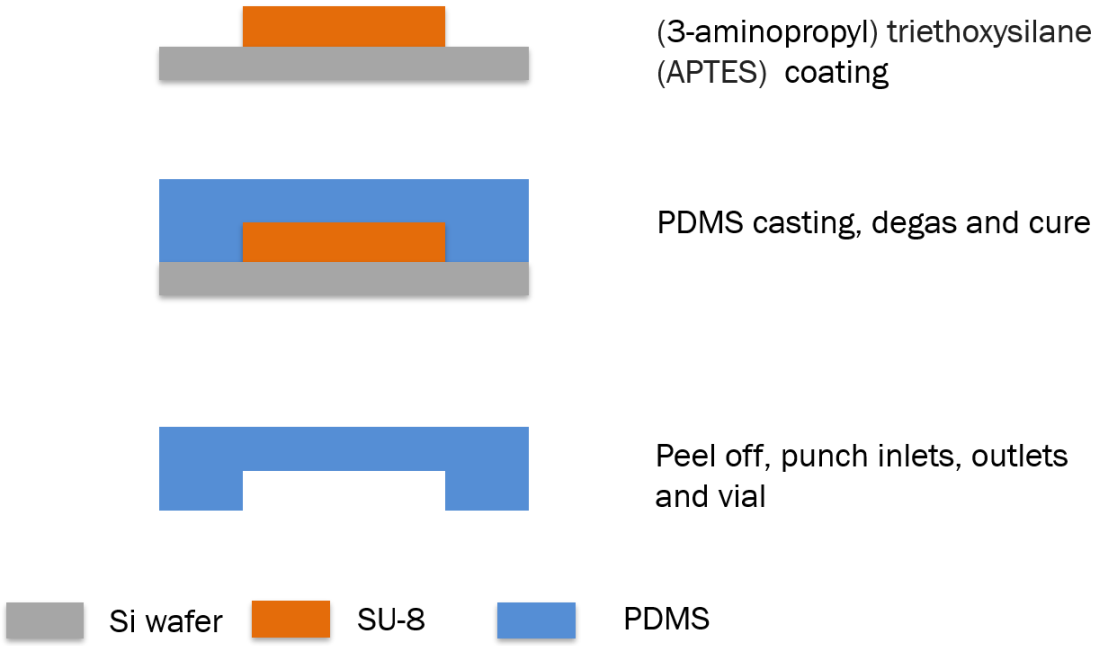

Figure 5 Fabrication process of the PDMS microchannel layers.

The fabrication process of the PDMS microchannel layers is shown in Figure 5. A Sylgard 184 Silicone Elastomer (Dow Corning) curing agent and base solution were thoroughly mixed at a weight ratio of 1:10, followed by a degassing process in a desiccator with a mechanical vacuum pump to remove any air bubbles and ensure a thorough mix of the two liquids. Then, a prepolymer mixture was cast on top of the master molds and cured at 65°C for 4 h. After curing, the PDMS replicates were peeled off from the master molds. The top layer was punched with three inlets and three outlets, and the center layer was punched with two holes to connect the bottom microchannel inlet and outlet. A large through-hole was also punched in the center layer.

2.3.2. Device Assembly

The microchannel layers were bonded by oxygen plasma pre-treatment. The methyl groups on the surface of the PDMS layers were oxidized to hydroxide groups under oxygen plasma

exposure. In the bottom/center layer bonding process, the channel side of the bottom layer and flat side of the center layer were treated with oxygen plasma for 2 min. A piece of PC membrane filter was sandwiched between these two layers. A uniform pressure was applied to the top of the device for 60 s. Then, the device was baked in the oven at 65°C for 2 h. After baking, the device was taken out for a second bonding process with the top layer. Another piece of PC nanomembrane was sandwiched between the bonded bottom/center layers and the top layer. After applying the appropriate pressure on top of the device to form pre-bonding, the three-layer device was baked at 65°C for 2 h to improve bonding quality. Microfluidic devices with four groups of nanomembrane combinations were fabricated. The pore-size combinations were: (1) 50 and 100 nm, (2) 30 and 100 nm, (3) 30 to 200 nm, and (4) 30 and 50 nm.

After removing the device from the oven, six pieces of tubing (Tygon 3350) were cut at the same length and connected to the inlets and outlets of the device. The free ends of the inlet tubing were connected to syringes, while the free ends of the outlet tubing were connected to containers that collected the separated solutions. Gold wires were employed as electrodes and pinned at the same position of the top inlet and bottom outlet tubing. A well-mixed epoxy was applied around each tube to prevent any leakage from the electrode points. Then, the device was baked at 65°C for 30 min to completely cure the epoxy glue. A photograph of the assembled microfluidic platform is shown in Figure 6.

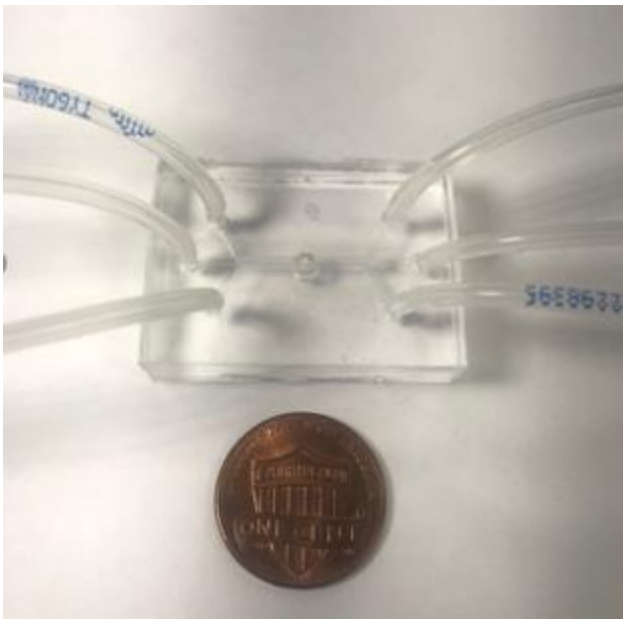

Figure 6 A photo image of the assembled microfluidic platform with tubing.

2.4. Experiment and Characterization

2.4.1. Sample Preparation and Experimental Set-up

For liposome isolation, the sample solution was prepared by mixing three particles with different diameters including polystyrene beads, liposomes, and antibodies. The stock solution of polystyrene beads stock solution was purchased from Sigma Aldrich. The mean particle size of polystyrene beads is 1 μm. The fluorescent dye (DHPE) labeled liposome stock solution was purchased from FormuMax, California, USA. The excitation wavelength is 496 nm and the emission wavelength is 519 nm. The mean particle diameter of liposomes is 100 nm with range of 90-120 nm. The goat anti-mouse immunoglobulin G (IgG) secondary antibody stock solution was purchased from Life Technologies with a concentration of 2 mg/mL. The antibody was used to represent proteins.

The initial solution was prepared by mixing 1 μL the liposome stock solution, 1 μL of the antibody (IgG) stock solution, and 1 μL of the polystyrene beads stock solution with phosphate-buffered saline (PBS) solution added to a total volume of 1 mL. 0.5 mL of the initial solution was pumped into the top microchannel at a flow rate of 5 μL/min, and the PBS buffer solutions were pumped into the center and bottom microchannels at flow rates of 10 and 20 μL/min, respectively. The applied voltage was kept at 200 V. The total processing time for isolation was less than 2 hours. The rest of the initial solution and isolated solutions were kept in the refrigerator at 4 °C for the following quantification analysis.

For EV and EV subgroups isolation, the MDA-MB231 cell line was obtained from the American Type Culture Collection (Manassas, VA). It was independently validated using STR DNA fingerprinting at MD Anderson Cancer Center. Tests for mycoplasma contamination were negative. Cells were grown in a DMEM medium supplemented with 10% fetal bovine serum at 37°C in 5% CO_2.

EV sample was prepared from the cell culture media with the following steps. Cells were cultured for 72 h. EVs were collected from their culture media after sequential ultracentrifugation as described previously.[76] In brief, cells supernatants were collected and centrifuged at 300 g for 10 min. The supernatants were collected for centrifugation at 2,000 g for 10 min, then collected again for another centrifugation at 10,000 g for 30 min. Finally, the supernatants were ultra-centrifuged at 100,000 g to pellet the EVs. The pellets were washed in a large volume of PBS to eliminate contaminating proteins and centrifuged one last time at the same high speed. The final pellets containing EVs were re-suspended in PBS and stored at −80°C. The total EV protein concentrations were determined using a BCA protein assay.

The initial sample cell culture media solution was prepared by diluting 1 μL stock EV solution with a PBS solution, for a total volume of 1 mL. To isolate sEVs with 30 and 100 nm membrane filters at different sample flow rates, 0.5 mL of the initial solution was pumped into the top microchannel at flow rates of 20, 10, and 5 μL/min, and the PBS buffer solution was pumped into the center and bottom microchannels at flow rates of 40 and 5 μL/min. Gold wires were connected to the positive and negative ends of a power supply and the applied voltage was set at 500 V. The outlets of the tubing were connected to containers to collect the solutions containing EVs. The total processing time was 50 min (less than 1 h). The rest of the initial and isolated solutions were kept in a refrigerator at 4℃ for a subsequent quantification analysis. The experiment setups were the same for the EV subgroup isolations using nanomembrane combinations of (1) 50 and 100 nm, (2) 30 and 100 nm, (3) 30 to 200 nm, and (4) 30 and 50 nm.

2.4.2. Extracellular Vesicle Characterization

The diameters of the particles were studied by dynamic light scattering (DLS) apparatus (Zetasizer nano, Malvern). The size distribution and total number of the particles in the original sample and isolated solutions were also measured by nanoparticle tracking analysis (NTA). Before measurement, the sample solution was diluted 10 times to fit the suggested particle concentration range for the instrument. The center channel solution was also diluted 2.5 times. The top outlet channel solution was also diluted 10 times before characterization. The measurement was conducted at room temperature using a NanoSight LM10 system (Malvern, Worcestershire, UK) with an emitting laser $\lambda = 405$ nm. Samples were manually introduced from a syringe and video images were recorded and analyzed by NTA software version 3.2. Particle distributions were measured at least three times. The average results of the particle size distributions were then

plotted; the dilution factors were considered when plotting the figures and calculating the total number of particles.

Scanning electron microscopy (SEM) images of the EVs were acquired by a Tescan scanning electron microscope. The isolated EVs were first filtered through a cellulose membrane (Whatman) to remove the PBS buffer, followed by washing with serial concentrations of ethanol to fully dehydrate the isolated EVs. The concentrations of ethanol were set at 50%, 60%, 70%, 80%, 90%, 95%, and 100%. Each washing was conducted three times. A 5-nm-thick Pt/Pd thin film was deposited on the surface of the isolated EVs on the filter membrane to increase the sample's conductivity for SEM imaging. The pore size distributions of the PC nanoporous membranes were also studied by SEM. The nanoporous membranes with different pore sizes (30, 50, 100, and 200 nm) were cut into small pieces and sputtered with a 5-nm-thick Pt/Pd film for SEM imaging.

Western blot analysis was used to identify the CD63 biomarker on EVs. EV samples were re-suspended in a 5 × SDS loading buffer (0.25 M Tris-HCl pH 6.8, 10% SDS, 50% glycerol, 0.5M dithiothreitol, 0.25% Bromophenol blue) and boiled at 95℃ for 10 min. Then, the samples were separated by 10% SDS-polyacrylamide gel electrophoresis (100 V, 2 h) and transferred to polyvinylidene fluoride (PVDF) membranes (90 V, 2 h). The membranes were blocked in a 5% milk solution at room temperature (RT) for 1 h and incubated with the CD63 primary antibody (BioLegend, mouse anti-human) diluted with the blocking solution overnight at 4℃. After washing three times with TBST, the membranes were incubated with a secondary antibody (anti-mouse IgG-HRP) at RT for 1 h. After washing the membrane three times with TBST, signals were detected using a chemiluminescent substrate (Thermo Fisher).

2.5. Results and Discussion

2.5.1. Isolation of Liposomes from Mixed Solutions

To study the feasibility and evaluate isolation efficacy of the proposed ExoSMP, isolation of liposomes from mixed solution containing three types of particles polystyrene beads, liposomes (representative of exosomes) and antibodies were demonstrated at the first step.[77]

Similarly, the microfluidic platform has three horizontally aligned microchannels and two nanomembrane filters with pore sizes of 30 and 200 nm sandwiched between the three microchannels as shown in Figure 7. Gold electrodes were connected to the top and bottom of the microchannels to induce the force through the two nanoporous membranes. Particles are separated based on pore sizes of the membrane filters. Due to the electric field between the top and bottom microchannels, proteins and particles less than 200 nm in size are forced to pass through the 200 nm membrane filter and transported into the center channel. Particles larger than 200 nm are separated from particles less than 200 nm and guided to the top outlet. All proteins are quickly guided into the bottom channel through the 30 nm membrane filter. Here, sample solutions containing 1 μm diameter polystyrene beads (representative of large particles), 100 nm diameter liposomes (representative of exosomes) and antibodies (<10 nm, representative of proteins) are used to validate the feasibility of the proposed isolation process and evaluate the separation efficacy.

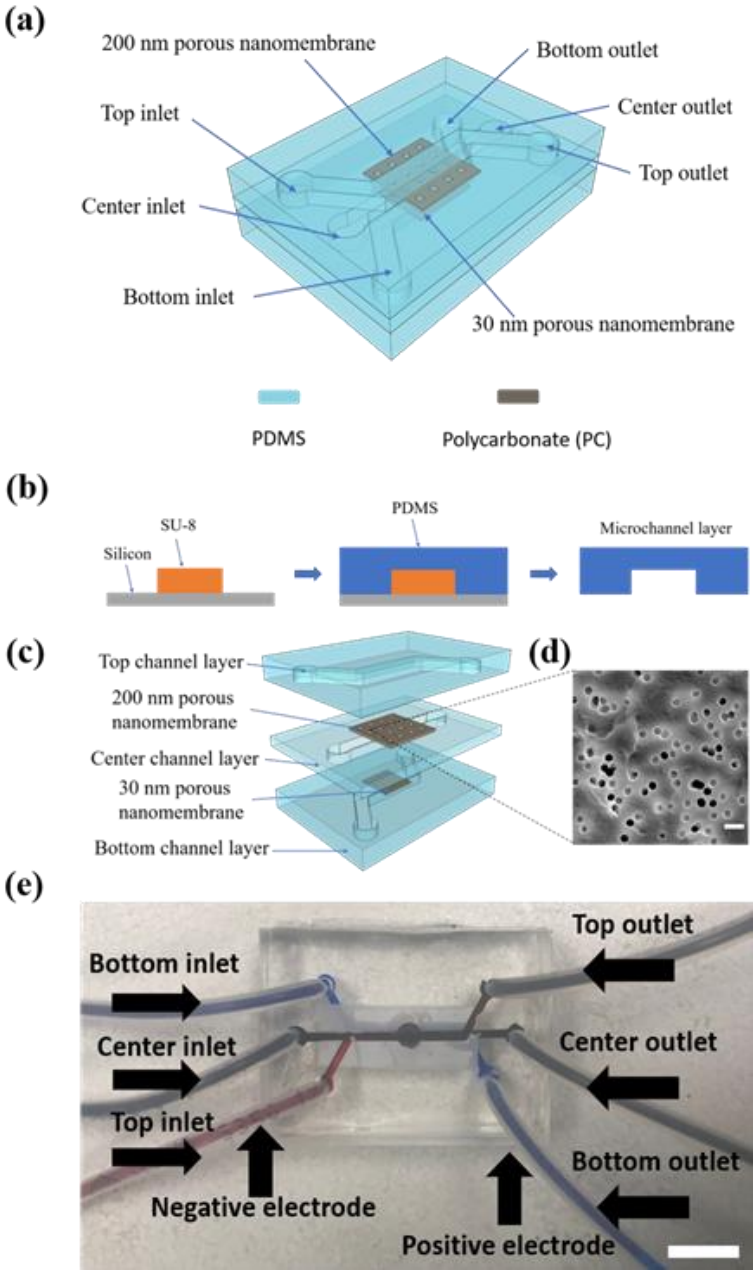

Figure 7 Schematic illustration of the size-selective microfluidic device for liposome isolation. (a) Schematic diagram of the microfluidic device. (b) Fabrication process of microchannel layers. (c) Assembly process of the microfluidic device. (d) SEM image of 200 nm PC membrane, scale bar: 500 nm. (e) A photo image of an actual device, scale bar:1 cm.

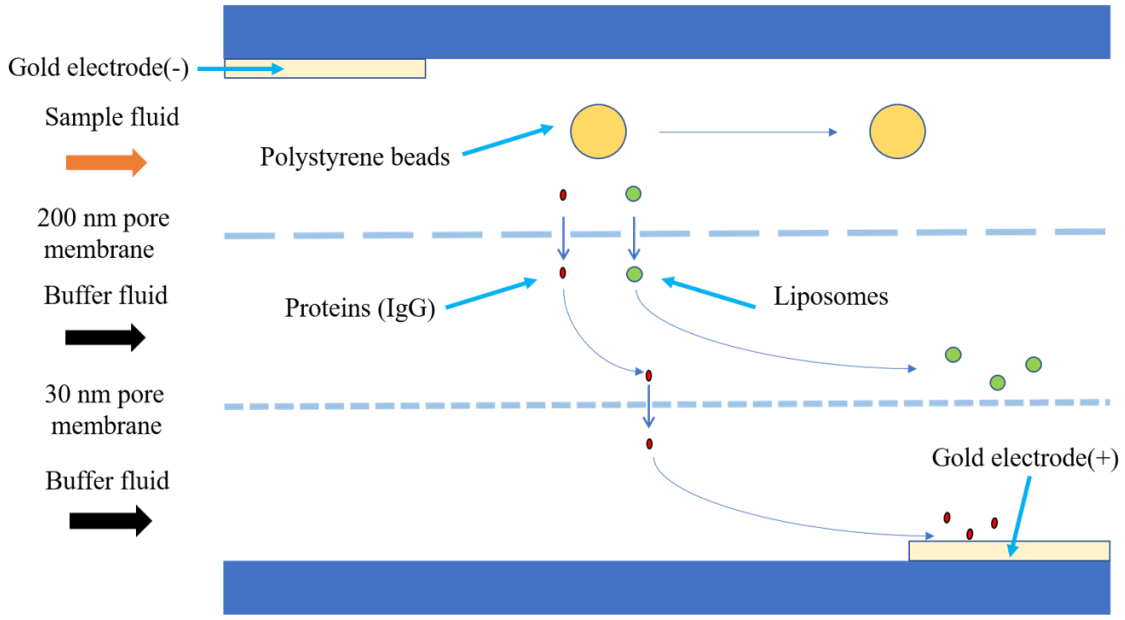

Figure 8 Schematic working principle of the size-selective microfluidic platform for liposome isolation.

During the separation process shown in Figure 8, fluorescence images were taken at the center outlet of the device. Figure 9 was the microscopic fluorescent image of the center channel outlet before the separation process was activated. Fluorescent microscopic image of the center channel outlet after the separation process was activated, was shown in Figure 9b. It was concluded that the DHPE labeled liposomes were continuously guided to the center outlet. When the initial solutions were pumped into the top channel, liposomes passed through the 200 nm nanomembrane to the center channel due to the electrophoretic force and flowed to the center outlet.

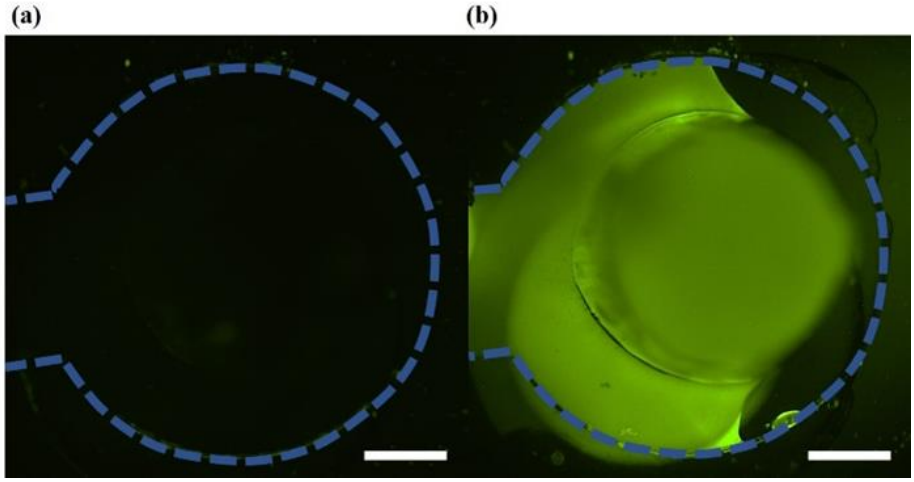

Figure 9 Fluorescent microscopic images at the center outlet, scale bar: 500 mm. (a) Fluorescent image of the outlet before isolation as control, and (b) after the isolation process. Obvious fluorescent image was acquired after the electric field application.

The initial solution and the isolated solutions were collected and then diluted by PBS solution to align with testing requirements for DLS measurement. As shown in Figure 10a, the initial solution that was pumped into the top inlet had two obvious peaks: about 100 nm and 1 μm, which contained mainly liposomes and polystyrene beads, respectively. No obvious peak in the range of 1 to 10 nm was detected although the IgG antibody was included in the initial solution. This was because the initial solution was polydisperse and the intensity of the IgG antibody was not strong enough to be detected compared to particles with larger diameters. The DLS analysis of the center isolated solution was shown as the graph in Figure 10b. This distribution graph had a visible peak at around 100 nm, which contained mainly liposomes. No peaks were detected at around 10 nm and 1 μm. Meanwhile, the particle distribution graph from the bottom isolated solution was shown in Figure 10c. This graph had a peak at around several nanometers, which contained proteins (IgG) mainly. No peaks were detected at around 100 nm and 1 μm. Thus, the results suggested that the liposomes in the initial solution were successfully separated from the mixture solution and

guided to the center microchannel. The IgG antibodies, representative of proteins, were also separated and guided to the bottom microchannel.

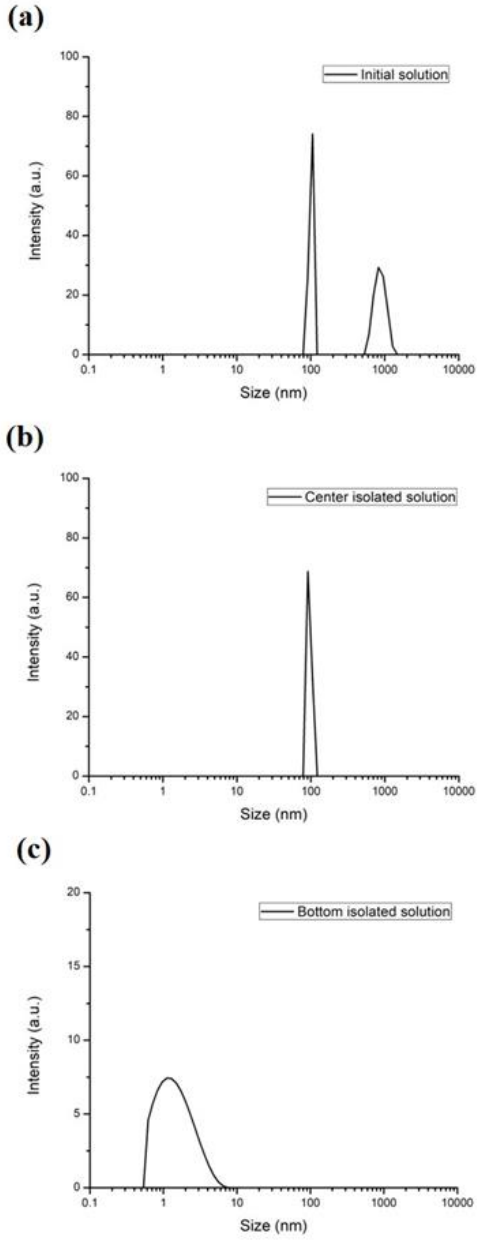

Figure 10 DLS analysis results for the initial and isolated solutions. (a) Initial solution. (b) Center isolated solution. (c) Bottom isolated solution.

The size distribution and total numbers of liposomes in the initial solution and isolated solution in the center outlet were analyzed by NTA. As shown in Figure 11, liposomes in both initial and center isolated solutions showed similar size distribution profiles. The peaks at around 250 nm could be aggregations of multiple liposomes. The center isolated solution exhibited a size distribution with a single peak at 98 nm. The initial solution showed a broad size distribution with a single peak at 106 nm, which represented a slight shift from the one acquired from the center outlet. This difference could be attributed to the resolution limits of NTA when testing highly heterogeneous samples.[63]

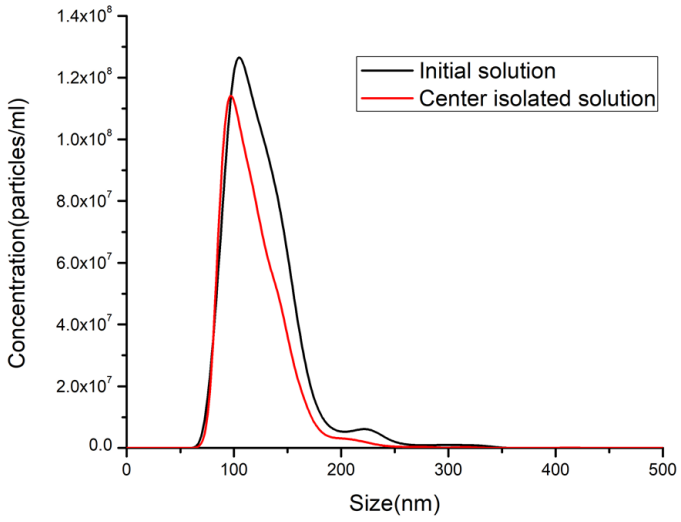

Figure 11 Size distribution for initial and center channel outlet solutions. From this graph, the recovery rate of liposomes was calculated.

The result from NTA measurement was used for qualification of the liposome concentrations. The volume of the center solution collected was twice of that of the initial solution. Liposome concentration in the center outlet was corrected by multiplying the dilution factor. The total number of liposomes (90 to 120 nm) from the center outlet was calculated at 3.12×10^9 per

microliter. The total number of liposomes (90 to 120 nm) in the initial solution was 3.37×10^9 per microliter. The recovery rate is defined as the fraction of the total numbers of isolated liposomes and the total numbers of liposomes in the initial solution. Overall, the present microfluidic platform showed a high recovery rate of 92.5% for liposome isolation.

In this study, a size-selective liposome isolation platform was conclusively developed and demonstrated. Polystyrene beads (representative of large particles), liposomes (representative of exosomes) and IgG antibody (representative of proteins) in the initial solutions were successfully separated with a liposome recovery rate of 92.5% with short processing time of less than 2 h.

2.5.2. Isolation of Cancer-Derived Extracellular Vesicles

EV isolation was conducted using ExoSMP with 30 and 100 nm membrane filters. Isolation efficacy was studied and compared under sample flow rates of 5, 10, and 20 μL/min. The size distribution and total number of EVs were measured by NTA and the averaged results of more than three times the measurements were plotted.

As shown in Figure 12a, the original sample solution (red line) exhibited a broad size distribution, with two specific peaks at approximately 108 and 154 nm representing two major EV subgroups: sEVs and mEVs. At the sample flow rate of 10 μL/min, the particle size distribution acquired from the center outlet (blue line) displayed a narrow range, between 50 and 150 nm, with a single peak at approximately 99 nm; this is consistent with the NTA results from the sample solution and predicted size of EVs based on the pore sizes of the nanomembrane filters. The peak concentration of sEVs in the center channel outlet solution was slightly higher than that of the sample solution. One possible reason could be that the total volume of the collected center outlet solution was slightly less than that of the sample solution (0.5 mL). Moreover, a slight shift in the

sEV distribution peaks acquired from the center channel outlet and original sample solutions was observed, which can be attributed to the detection limits of the NTA resolution due to the heterogeneity of the samples.

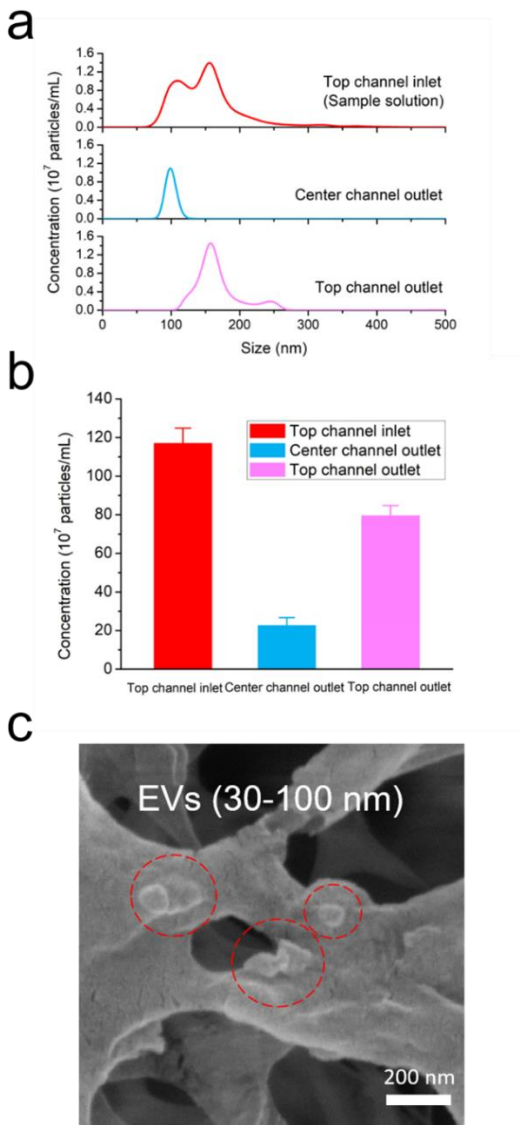

Figure 12 Isolation of EVs from cancer cell derived EVs with 30 and 100 nm nanoporous membranes at the sample flow rate of 10 μL/min. (a) The size distributions of the particles in top channel inlet (original sample solution, red line), center channel outlet (blue line), and top channel outlet (pink line) solutions. (b) The total numbers of particles at the top channel inlet (red bar), center channel outlet (blue bar), and top channel outlet (pink bar) are calculated from the NTA profiles. (c) SEM image of the isolated EVs loaded on a cellulose filter membrane.

The top channel outlet solution (pink line) exhibited a size distribution between approximately 100 and 280 nm with a single peak at about 156 nm, which corresponded to the other major subgroup of microvesicles. This result is also coincident with the particle distribution from the original sample solution. The total number of the particles in the top channel inlet (red bar), center channel outlet (blue bar), and top channel outlet (pink bar) solutions were 1.17×10^8 per mL, 2.26×10^8 per mL, and 7.95×10^8 per mL, respectively, as shown in Figure 12b. The total number of particles collected from both the center and top channel outlets as a fraction of those in the sample solution was 87.2%, suggesting that ExoSMP achieved a high sample yield with minor loss during the isolation process. The sample loss could be due to particles remaining in the microchannels or tubing that were not transported to the outlets. The morphology and size of the isolated EVs were confirmed and examined by SEM, as shown in Figure 12c and Figure 13.

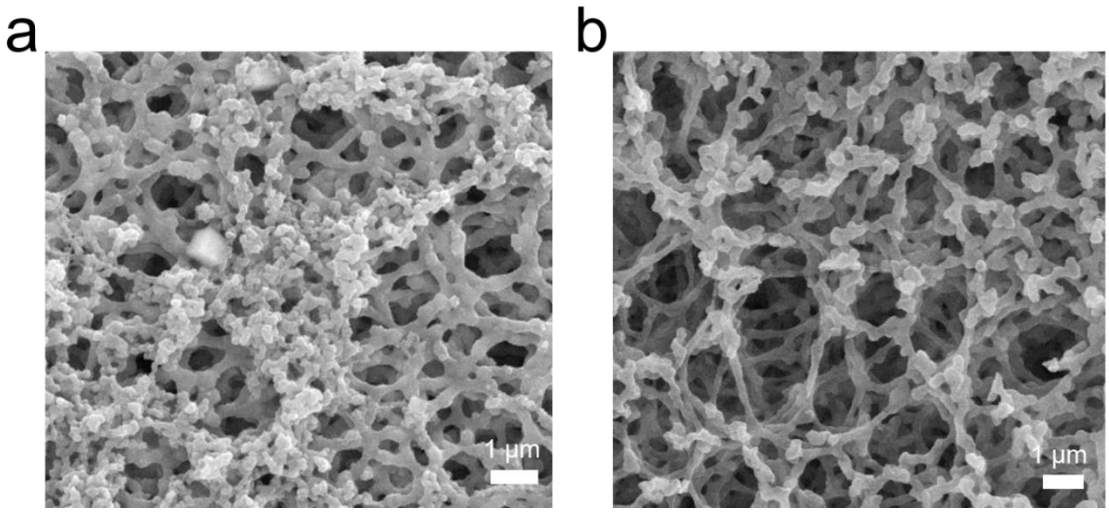

Figure 13 SEM images of the cancer derived EVs. (a) EVs in the sample solution. (b) The EVs isolated from the center channel outlet by the nanomembrane filters with pore sizes of 30 and 100 nm.

Significant variations in the size distribution profiles were observed under different sample flow rates, given the 0.5 mL volume of sample solution. At the sample flow rate of 20 μL/min, the

total number of EVs collected in the center outlet solution was too low to be accurately measured by the NTA. The size distribution of the particles collected from the top outlet (see Figure 14) was analyzed. It showed a similar broad size distribution with two peaks at 120 and 155 nm, which represented the sEV and mEV subgroups. The size distribution of the mEVs exhibited a profile close to that of the original sample solution, while the size distribution of the sEVs showed a low level of EV recovery, indicating that most of the particles were guided to the top outlet channel due to the fast sample flow rate.

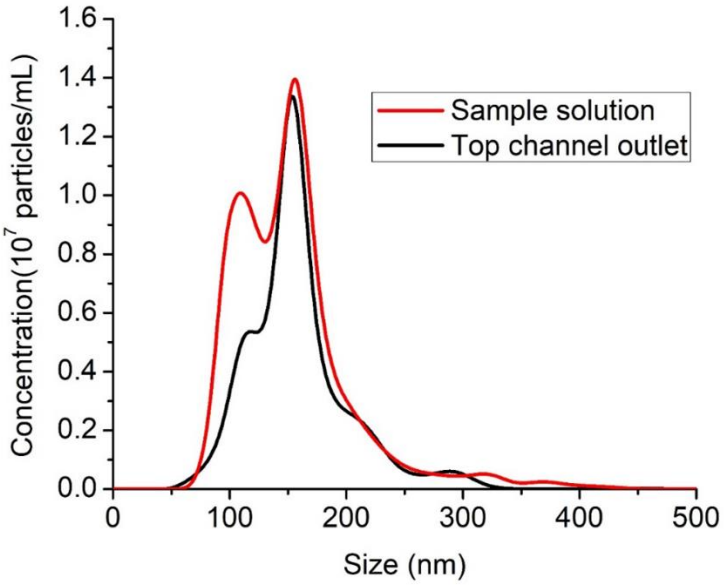

Figure 14 The size distribution of particles collected from the top channel outlet at a sample flow rate of 20 μL/min (black line). The size distribution of particles in the sample solution is shown in red line.

The size distribution of the particles collected from the center channel outlet (green line) at a sample flow rate of 5 μL/min is shown in Figure 15a. A broad size distribution was observed between 50 and 400 nm with two peaks at 113 and 202 nm representing the sEVs and mEVs. The peak at 202 nm indicates that EVs larger than the pore size (100 nm) of the first membrane filter

were collected in the center channel outlet. Particles took more residual time to pass through the nanomembrane filter area at this sample flow rate. This phenomenon can be explained by the deformability of EVs through the nanomembranes. EVs consist of soft and flexible membranous lipid structures, which enables them to pass through the membrane filter even if their diameter exceeds the physical size limitation of the pores.[78, 79] With a long residual time, some of the large vesicles (> 100 nm) may have had enough time to deform and penetrate through the nanomembrane filter with a pore size of 100 nm, resulting in the peak shift corresponding to sEVs and a broad distribution of mEVs. Coincidently, some small particles with diameters between 30 and 100 nm might also have had sufficient time to pass through the 30 nm membrane filter, thus reducing the number of sEVs recovered from the sample solution.

As shown in Figure 15 b, the total number of particles with dimensions between 30 and 100 nm isolated at the sample flow rate of 10 μL/min was calculated to be 1.29×10^8 per mL. This was much higher than that of the sample flow rate of 5 μL/min, which was calculated to be 6.58×10^7 per mL. The recovery rate was defined as a fraction of the total number of particles with dimensions between 30 and 100 nm that were recovered from the center channel solution and total number of particles in the original sample solution. The purity is defined as the fraction of the isolated particles among the collected particles of all sizes in the center solution.

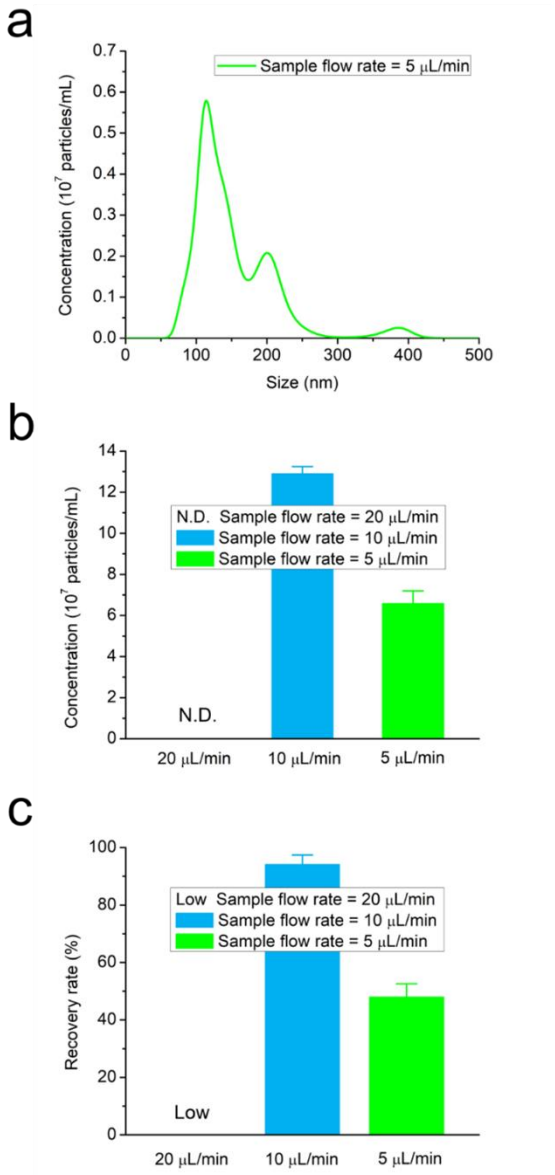

Figure 15 Isolation of EVs from cancer cell derived EVs at different sample flow rates. (a) The size distribution of the isolated EVs collected in the center channel outlet (green line) at the sample flow rates of 5 μL/min. (b) The numbers of particles with dimensions from 30 to 100 nm collected from the center channel outlet solution at different flow rates. N.D. refers to not detectable. (c) Recovery rates of the EVs with dimensions from 30 to 100 nm determined based on the NTA data.

As shown in Figure 15c, the recovery rate at a sample flow rate of 20 μL/min was low. From our calculations, at a sample flow rate of 10 μL/min, the total number of particles ranging from 30 to 100 nm collected in the center channel outlet solution and the number of particles with the same dimension range collected in the sample solution were 1.29×10^8 per mL and 1.37×10^8 per mL, respectively. The recovery rate in this situation was calculated as 94.2%, with a very small standard deviation of 3.2%. The results show that the EVs were isolated from the cancer cell culture media with high rates of recovery and reproducibility at the optimal sample flow rate. We also calculated that the purity of the isolated EVs ranging from 30 to 100 nm was estimated to be 56.3%, In the meanwhile, we calculated the recovery rate and the purity of the isolated EVs ranging from 30 to 110 nm to be 86.9% and 90.7%, respectively. The results implied that of a large proportion of the isolated EVs have size ranging from 100 to 110 nm. Similarly, at a sample flow rate of 5 μL/min, the total number of particles ranging from 30 to 100 nm collected in the center channel outlet solution was 6.58×10^7 per mL, and the recovery rate was calculated as 48.0%. Overall, the proposed microfluidic platform showed a high rate of recovery of 94.2%, at the optimum sample flow rate for particles ranging from 30 to 100 nm, while also offering the advantage of a short processing time (less than 1 h).

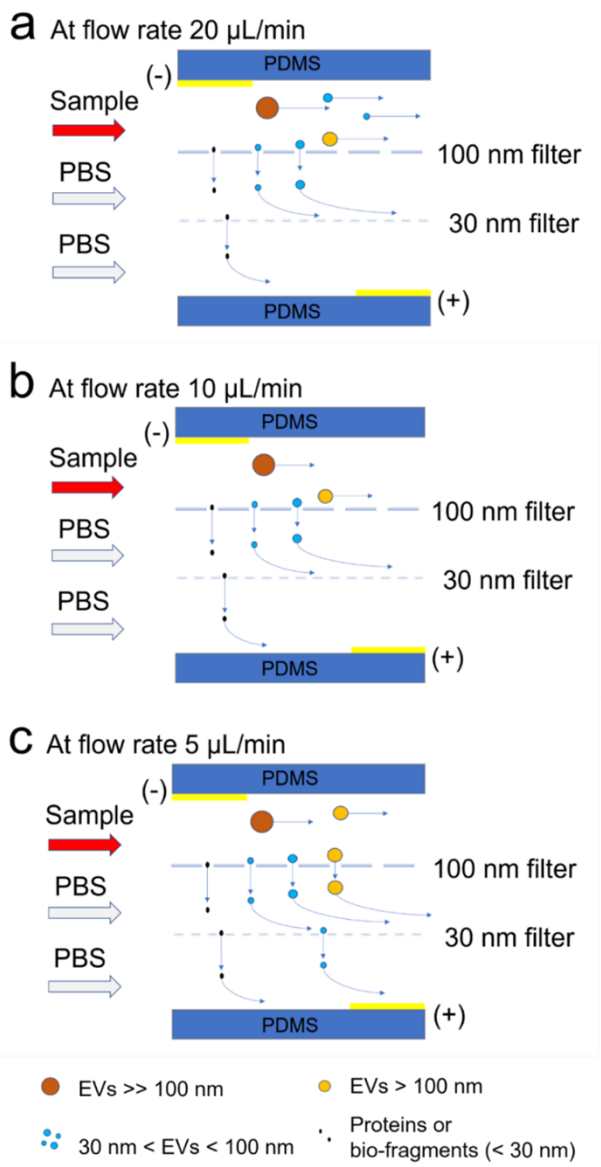

Figure 16 Schematic side view diagrams of the EV isolation processes at different sample flow rates. (a) 20 µL/min (b) 10 µL/min and (c) 5 µL/min sample flow rates. Schematic particle trajectories are labeled in blue arrows.

The schematic diagram of the isolation process at a sample flow rate of 20 µL/min is shown in Figure 16a. Under this condition, the EVs had less residual time to pass through the nanomembrane filters and most of the particles were quickly transported to the top channel outlet, which led to a low EV recovery. In contrast, the isolation mechanism at a sample flow rate of 10

μL/min is shown in Figure 16b. ExoSMP achieved a high particle recovery rate at the optimized sample flow rate. The schematic diagram of the isolation process is shown in Figure 16c at a sample flow rate of 5 μL/min. In this situation, the EVs took more residual time to pass through the nanomembranes due to their soft and flexible membranous structures, which led to the peak corresponding to microvesicles, and thus reduced the EV recovery compared to that at a sample flow rate of 10 μL/min.

2.5.3. Isolation of Subpopulations with Different Nanomembrane Combinations

We further demonstrated the microfluidic platform as a modular unit for sEV subpopulation and EV subgroup isolation with tunable size groups. The ExoSMP technique was used to separate subpopulations of sEVs and subgroups of EVs simply by altering the pore sizes of the nanomembrane filters. Size-selective isolation was investigated with different nanomembrane combinations: 50 and 100 nm, 30 and 50 nm, and 30 and 200 nm. The isolation process and parameters were same as those of the sEV isolation with 30 and 100 nm membrane filters.

The size distributions of the isolated EVs from the nanomembrane combinations of 50 and 100 nm and 30 and 200 nm were acquired by NTA, as shown in Figure 17a. The sEV subpopulation isolated by 50 and 100 nm nanomembrane filters displayed a narrow size distribution with a single peak at 100 nm, which corresponded to the major EV subgroup of sEVs. This size distribution profile was similar to that of sEVs isolated by nanomembranes with 30 and 100 nm pore sizes. The EV subgroup isolated by 30 and 200 nm nanomembrane filters exhibited a broad size distribution, between 50 and 400 nm. Single peaks at about 107 nm and 163 nm corresponded to the two major EV subgroups of sEVs and mEVs. The size distribution displayed a profile similar

to that of the original sample solution. A valley between two peaks at 132 nm was consistent with that of the original sample solution at 130 nm. A small peak at about 330 nm indicated that there might be a small amount of microvesicles penetrating through the 200 nm membrane filter, or some EV aggregation. The size distribution of the isolated EVs collected from the device with 30 and 50 nm membrane filters was not applicable, which was mainly attributable to the detection limit of NTA for heterogeneous samples of small dimensions.

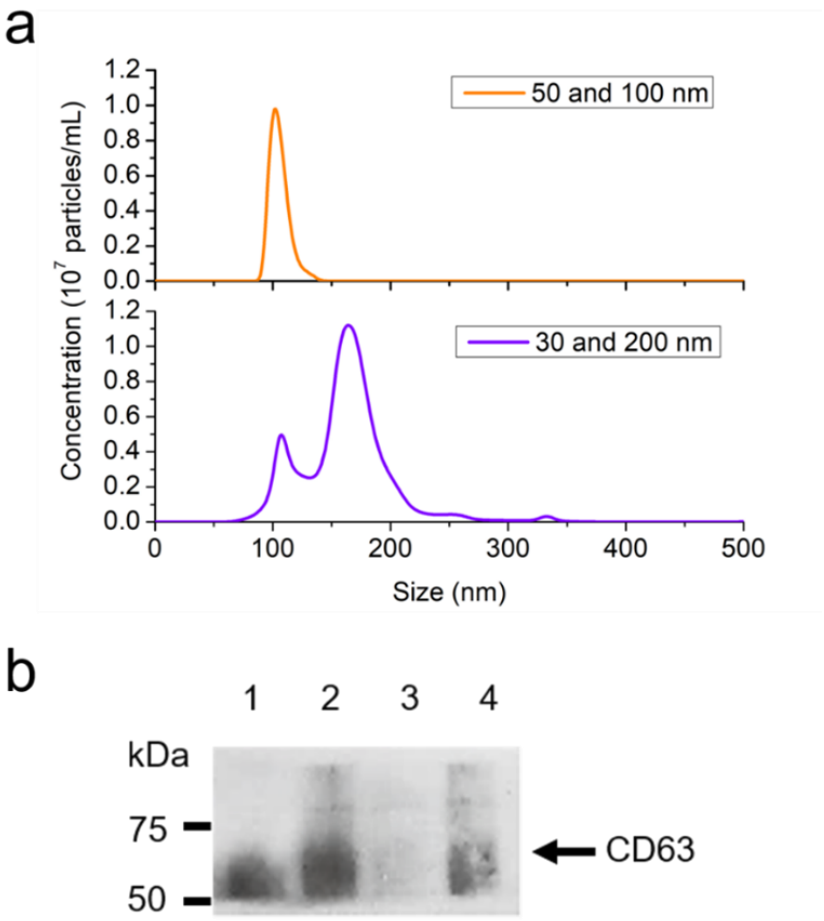

Figure 17 Isolation of sEV subpopulations and EV subgroups with ExoSMP and different pore sizes. (a) The size distributions of the isolated EVs with different nanoporous membrane combinations by NTA. (b) Western bolt analysis of EV biomarker CD63 in the isolated EVs with different nanomembrane combinations: (1) 50 and 100 nm, (2) 30 and 100 nm, (3) 30 to 200 nm, and (4) 30 and 50 nm.

For each size group, the EV transmembrane protein CD63 was studied by western blot analysis, as shown in Figure 17b. The isolated exosomal biomarker was confirmed by the smear patterns, which were observed for α-CD63, as expected.[56] The EVs were isolated with the following nanomembrane combinations: 30 and 100 nm, 30 and 200 nm, and 30 and 50 nm; they showed broad smear patterns ranging from 50 to above 75 kDa, while only the isolated EVs with the 50 and 100 nm nanomembrane combination showed narrow smear patterns in the range of 50 to 75 kDa. It is of note that the light smear patterns for the isolated EVs with the 30 and 200 nanomembrane combination were due to a low EV recovery, as shown by the size distribution measured by the NTA result (see Figure 17).

2.6. Summary

To summarize, a size-selective microfluidic platform (ExoSMP) was developed and demonstrated for automated, consistent, and reliable EV isolation. This unique platform offers an enhanced approach to the isolation of EV subgroups and sEV subpopulations, along with the additional advantage of being label-free, low-cost, and featuring a short processing time (< 1 h), and convenient integration with downstream analysis. This platform demonstrated a high recovery rate of 94.2% and reproducibility (a low standard deviation) from cancer cell culture media samples with an optimal sample flow rate. The size-selective isolation of EVs can easily be controlled by altering the pore sizes of the nanomembrane combinations. We further utilized ExoSMP with various combinations of nanomembrane pore sizes to demonstrate the isolation of EV subgroups and investigate sEV subpopulations of various size groups. The western blot analysis suggested the evidence of CD63 biomarker in the subgroups of the EVs. This improved technique will serve as a precise clinical tool for isolating EVs and addressing the heterogenicity

of EV subgroups. Additionally, with its efficient size-based isolation of EV subpopulations, ExoSMP shows broad promise for investigating the role of EVs in various point-of-care applications in disease monitoring, medical diagnosis, and drug delivery.

3. LOW-COST AND ENZYME-FREE PAPER SENSORS[†]

3.1. Introduction

3.1.1. Significance

Diabetes mellitus is a chronic condition that affects millions of people around the world. The disease develops as a result of either disrupted insulin production (type I) or altered insulin absorption (type II).[80] Diabetic patients must monitor their glucose concentration often to avoid complications, such as cardiovascular damage, nerve degeneration, and vision damage.[81, 82] For this purpose, current glucose sensors utilize electrochemical glucose detection with glucose oxidase (GO_x) to detect changes in glucose concentration and have been commercially available and commonly used for diabetic patients.[83, 84] This enzyme-based method is costly and sensitive to pH and temperature. Furthermore, electrochemical detection of glucose based on GO_x on a solid substrate is unreliable.[85] To improve such weakness, there have been multiple new glucose-sensing techniques, such as optical transducers,[86, 87] and electrical transducers[88-91] investigated; however, these approaches still require GO_x structures to recognize glucose, although their reliabilities have been improved. As one of the most expensive diseases to treat, it is

[†] Part of this chapter is reprinted with permission from "A Low-Cost Paper Glucose Sensor with Molecularly Imprinted Polyaniline Electrode" by Chen, Z., Wright, C., Dincel, O., Chi, T. Y., Kameoka, J., 2020. *Sensors*, 20 (4), 1098, Copyright 2020 by Multidisciplinary Digital Publishing Institute. "A Low-cost and Enzyme-free Glucose Paper Sensor", Chen, Z., Chi, T. Y., Dincel, O., Tong, L., Kameoka, J., 2020. *Annu Int Conf IEEE Eng Med Biol Soc*, 2020, 4097-410, Copyright 2020 by Institute of Electrical and Electronics Engineers.

important to reduce the cost of detecting glucose levels as much as possible without sacrificing reliability and accuracy.[92]

To address the need for easy, rapid, and reliable glucose sensing with low cost, various non-enzymatic methods have been investigated and developed.[93-95] Among these methods, molecularly imprinting (MIP) approach has attracted much attention. MIP is a promising process that works by the co-polymerization of functional monomers and cross-linking agents in the presence of a template molecule or its derivative.[96] MIP approach has shown great advantages, such as its simple preparation, potential reusability, long-term durability, and stability as well as low-cost production.

3.1.2. Low-Cost Paper Sensor Using MIP Technology

MIP technology has been applied in various fields, such as purification,[97] chromatographic separation,[98] chiral separation,[99] and solid-phase extraction.[100] MIP has also been investigated in chemical/biosensors.[96, 101-104] However, a simple, cost-efficient, and easy-operating way to transduce specific signals has yet to be established. Polyaniline (PANI) is one of the conductive polymers that has been widely used as a sensing electrode due to its characteristics of stability, high conductivity, and easy synthesis. MIP-PANI can act as both the sensing electrode and the conductive electrode, with the additional advantage of being low cost. The electrochemical polymerization of aniline has been reported as one of the most common approaches for biosensing,[105, 106] which demonstrates good selectivity and sensitivity. However, electro-polymerization has some drawbacks. The method requires monomers that can be oxidized electrochemically, and the substrate

must be conductive but inert to react during the electro-polymerization process. Moreover, conducting polymers tend to detach from the electrodes after suffering mechanical stress, sonication, and sterilization [107-109]. Such drawbacks limit its potential application in disposable glucose test strips with long durability and stability.

As common and low cost substrate, paper is recently replacing the conventional substrate in the microfluidics field.[110].Additionally, its bendable nature enables paper-based microfluidic sensors to be flexible and wearable.[111-113] Paper also has natural wicking force that enable transportation of fluids through the channel automatically.[114] Furthermore, a folded layout of paper, or called origami paper, is widely applied in paper microfluidic sensors including colorimetric assays,[115] potentiometric biosensors, and enzymatic glucose sensors.[111, 116, 117] Its three-dimensional configuration consisting of a sequence of panels allows vertical transportation, separated reaction sites, and time-controllable sensing.[118]

In this chapter, instead of utilizing enzymes, we developed and demonstrated a low-cost paper biosensor by direct MIP technology. This process enables a simple one-step approach to the fabrication of PANI by polymerization of the aniline monomer with the template on paper strips, providing a glucose-sensing electrode and a signal-transducing electrode at the same time. The proposed device was fabricated by MIP in a solution to create a glucose-binding site integrated with a conductive PANI electrode.[119, 120] As a proof of concept, glucose concentration was determined in both aqueous and bovine blood solutions to evaluate the performance of the PANI paper sensors. This simple and straightforward approach makes the production of easy, rapid, and robust glucose test

strips possible and provides low-cost and reliable glucose-monitoring access to diabetes patients.

3.2. Materials and Methods

A schematic diagram of molecular imprinting process is illustrated in Figure 18. The MIP process mainly consists of copolymerization of the functional monomers and template materials, and removal of template materials to form specific binding sites for target (template materials) sensing. Various target molecules such as glucose, C-reactive protein (CRP) can be used as the template materials and will be further discussed in this chapter.

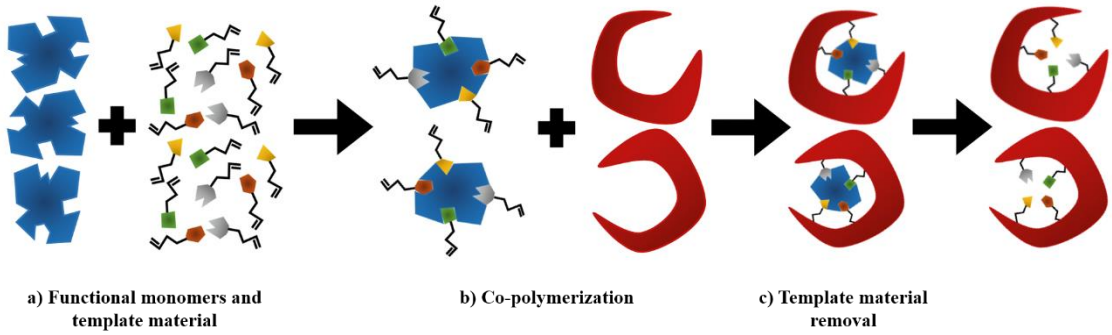

Figure 18 Schematics of molecular printing process. (a) Functional monomers (blue) and template material are mixed in the solution. (b) Functional monomers and templates co-polymerization. Aniline and glucose were used as the monomer and template materials. Glucose recognition sites/cavities were created during the polymerization of aniline. (c) Removal of template. Glucose template was removed by washing with the ethanol-water solution and followed by rinsing with DI water.

3.2.1. Synthesis of Molecularly Imprinted Polyaniline Paper

The polyaniline was synthesized from an aniline monomer solution (99%, Sigma-Aldrich, USA) as shown in Figure 19. 250 μL of the monomer solution was blended with

1 mL of 36.8% (w/v) hydrochloric acid (HCl, ACS grade, Macron, USA), which acts as the doping agent to increase the conductivity of PANI. An amount of 3 mL of DI water was added to the mixed solution to adjust the final concentration. Next, the template molecule, 50 mg of glucose (Sigma-Aldrich, USA), was blended into this solution to create glucose binding sites. To achieve the proper concentration for PANI polymerization, DI water was added until the total volume of the solution became 5 mL. For the final process, polyester paper substrates (iGage, USA) were cut into strips (7 × 4 mm, 250 μm in thickness) and dipped into the final solution to be soaked with the aniline-HCl solution, completely saturating the paper strips. The paper strips were soaked and stirred in the solution for at least 10 min before the oxidation process to ensure continuous saturation.

To prepare the oxidant solution, 0.609 mL of HCl was added into 4 mL DI water, followed by the addition of 409 mg of ammonium persulfate (APS, Sigma-Aldrich, USA). After 10 s of stirring, a bit more DI water was added to make the total volume of the prepared solution equal to 5 mL. HCl was also used to maintain the pH (pH = 0) and doping levels throughout the synthesis process.

Next, the synthesis process was initiated. While stirring the aniline solution, the oxidant solution was added drop by drop. The oxidant drops were dispensed in 5 s intervals from a pipette until the color of the solution changed from yellowish to dark blue (Figure 1e). The paper strips were kept immersed in the solution. To complete the synthesis process, the paper strips were removed from the solution, washed with DI water to remove

excess PANI as well as glucose templates (Figure 1b), and then left out to dry for at least 8 h before usage.

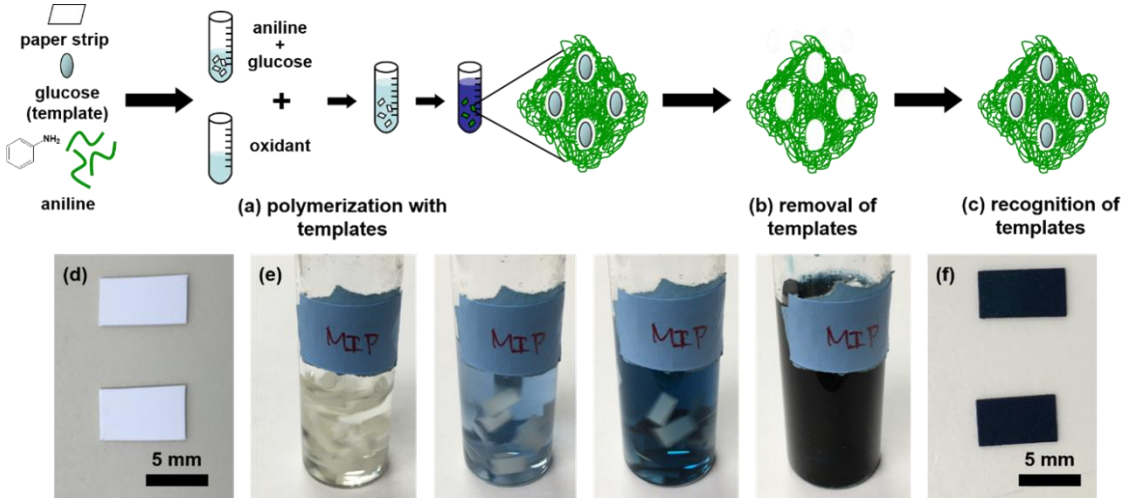

Figure 19 A schematic diagram of the molecular imprinting process for the fabrication of a paper sensor. The template represents glucose in this figure. (a) Polymerization with templates. Glucose templates were mixed with aniline solution, the monomer, prior to the addition of the oxidant solution. Glucose-imprinted PANI, represented as the green regiment embedding templates in the schematic diagram, was then synthesized on the paper substrate. (b) Removal of glucose templates by washing the paper strips with DI water. The cavities left in the polymer matrix create the specific recognition sites for the corresponding targets. (c) Recognition of templates on the paper sensor when conducting the glucose concentration measurement. (d) The polyester paper was cut into strips before polymerization. (e) The color of the polymerization solution changed from yellowish to light blue and finally became dark blue due to the doping process. The paper strips were completely immersed and were subject to vigorous stirring in the solution during polymerization. (f) The prepared paper strips with glucose imprinted PANI synthesized on both sides of the surface after the glucose removal process by washing with DI water.

3.2.2. Fabrication of the Paper Sensor

After the paper strips were fabricated (see Figure 19f), the electrodes were printed by an inkjet printer using the Fujifilm Dimatix Material Printer 2830 with Novacentrix JS

ADEV 291 ink. The operation parameters of the printer are listed in Appendix A. Silver traces were printed on a flat polyester film (Xerox, USA) with open space left for the PANI paper strips. The schematic diagram of the fabrication process of the PANI paper sensors were presented in Figure 20. The printed silver traces were cured at 110 °C for 1 h.

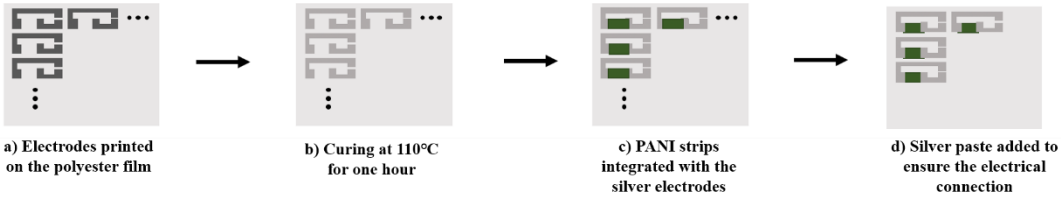

Figure 20 Schematics of the fabrication process of the PANI paper sensors. (a) Silver electrodes were printed on the polyester flexible film. (b) Curing of the printed silver electrodes at 110°C for one hour. (c) The prepared PANI strips were placed on the printed silver electrodes. (d) Conductive silver paste was applied to connect the silver electrodes and the PANI paper strips electrically.

Then, the PANI paper strips were fixed onto the open space and electrically connected to the silver traces via silver paste. Figure 21 showed the photographic image of the fabricated PANI paper sensor with glucose templates on the silver trace.

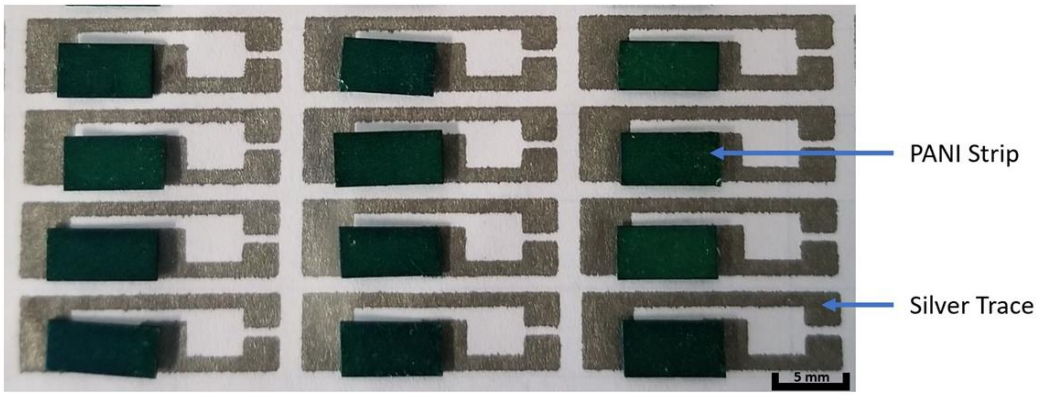

Figure 21 Photographic image of the paper sensor device after the initial silver traces were printed and before the secondary silver paste layer was formed to secure the strip to the device.

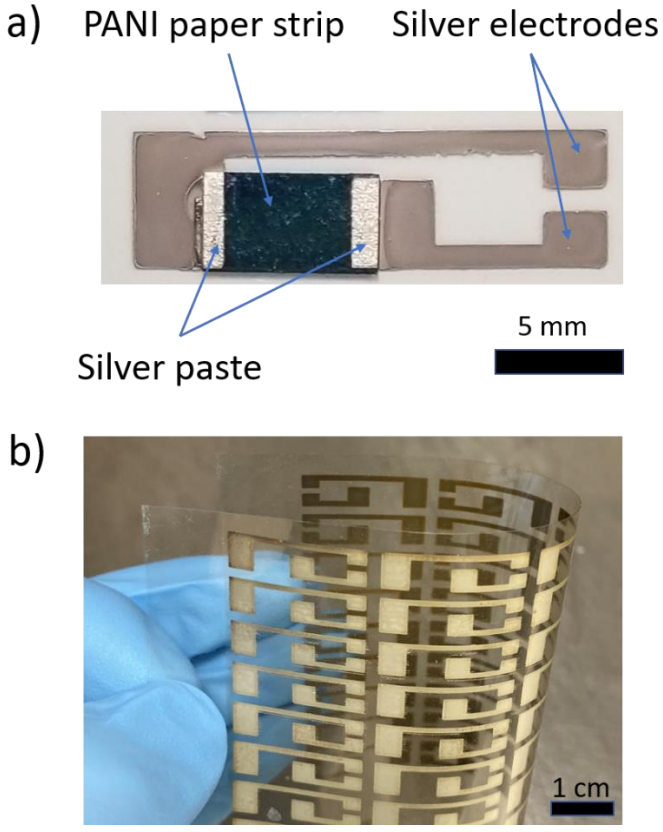

Figure 22 Photo images of the proposed PANI paper sensor. (a) A photo image of the paper sensor. (b) Silver electrodes on the flexible polyester film after curing.

3.3. Characterization and Measurement

3.3.1. MIP-PANI Characterization

An Attenuated Total Reflectance-Fourier-transform Infrared (ATR-FTIR) Spectrometer was used to confirm the presence of glucose captured by the PANI paper sensor. The paper strips were exposed to 0 to 12 mM glucose, then rinsed with DI water after 5 min of the sample dispensing on the PANI surface. The paper strips were washed and dried in a vacuum overnight at room temperature. ATR-FTIR spectra of the surface were measured using the ATR module of the Thermo Nicolet 380 (Thermo, USA) FTIR spectrometer.

Scanning electron microscopy (SEM) image of the PANI paper sensor was acquired by a Tescan scanning electron microscope. The surface of the paper strips was cut into small pieces and sputtered with a 5-nm-thick Pt/Pd film to improve the conductivity.

3.3.2. I-V Curve Measurement

After the sensor fabrication, the I-V curve of the paper sensor was investigated. The experiment set up is shown in Figure 23. A multimeter (Fluke 8846A, USA) was used for recording the current. A DC power supply (Agilent E3643A, USA) was used for applying the voltage on the two ends of the silver trace. The voltage was applied from 0 to 10 V with a 1 V interval. The I-V curve measurement was conducted under air after dispensing DI water, and after dispensing 12 mM glucose in DI water. The sample

volumes were the same (2 uL) and the measurement was conducted after 5 min of sample dispensing.

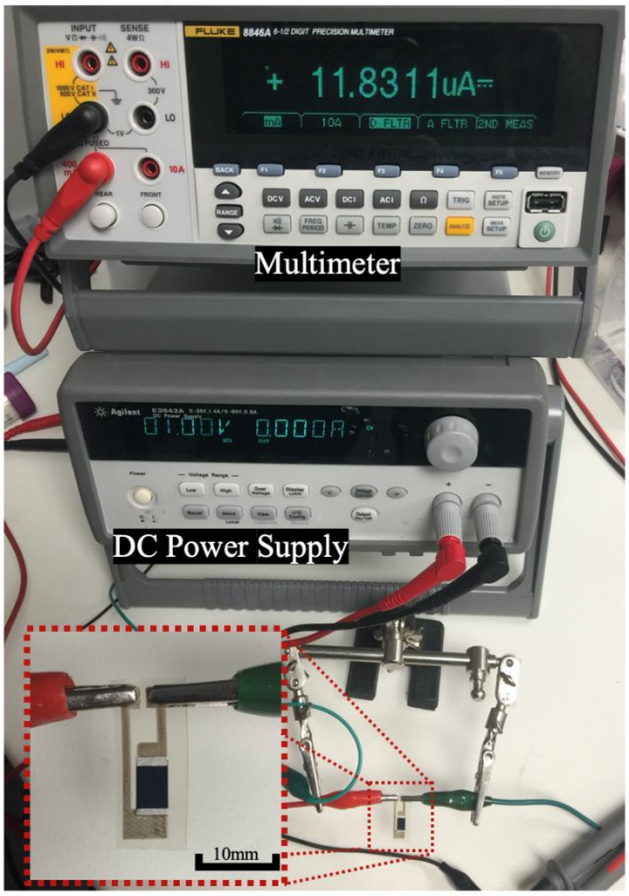

Figure 23 Photographic image of the experiment set-up for measuring the I-V curves of the paper sensor.

3.3.3. Glucose Concentration Determination

The determination of glucose concentration was conducted by measuring the resistance change by connecting the two electrodes to the paper sensor. This approach is simple in operation and cost-efficient compared to other methods with an additional reference electrode or gate electrode. The resistance of the paper sensor was measured by

a multimeter (Fluke 8846A) in a DC current mode. For glucose concentration determination in DI water, sample solutions with glucose concentrations from 0 mM to 12 mM were prepared. First, the direct current (DC) resistance of the device was measured as a reference level with DI water. An amount of 2 μL of the sample solutions with gradient glucose concentrations was dispensed on the surface of the PANI strips. All DC resistance was measured 5 min after sample dispensing. We compared the results based on the resistance change ratio (ΔR), which is the fraction of the sample with glucose solutions and the control samples.

Impedance (Z) of the paper sensor can be described as equation (1),

$$Z = R + j\,X \tag{1}$$

where R is the resistance and X is the reactance. The applied voltage reflects the impedance of the paper sensor in the equation (2),

$$Z = (|V| / |I|)\, e^{j\theta} \tag{2}$$

where θ is the phase difference between voltage and current. However, under low frequency condition, the real part of the impedance is dominant. We have obtained the resistivity from the equation (3),

$$Re(Z) = |Z| \cos\theta \tag{3}$$

The ratio of the impedance (ΔZ) can be approximately calculated by the equation (4) below.

$$\Delta Z = Re(Z_1) / Re(Z_2) \tag{4}$$

$Re(Z_1)$ represents the real part of the impedance of the PANI paper sensor after the sample solution dispensed. And $Re(Z_2)$ represents the initial real part of the impedance before exposed to the sample solution.

Each paper sensor was dispensed with the sample solution and the impedance change of the sensor was recorded. Three repeating measurements (n=3) on different paper sensors were conducted on each glucose concentration.

For glucose concentration determination in bovine blood, a 250 mL bovine blood sample solution containing 35 mL of anticoagulant Citrate Phosphate Dextrose was used to characterize the performance of the paper sensor. The bovine blood was obtained from a healthy bovine from the Department of Veterinary in Texas A&M University. The blood test was conducted immediately after receiving the blood sample. The bovine blood solutions were added with 0, 0.1, 0.5, 2.2, 4.4, 6.7, 8.9, and 11.1 mM glucose as the sample solutions. The sample solutions were gently stirred before dispensing onto the PANI electrodes for glucose concentration detection. The volume of the blood samples was kept the same at 10 uL.

The resistance change of the paper sensor was detected before and after the sample solution dispensing. The resistance change ratios of the samples with different glucose concentrations added were calculated and normalized to the original resistance ratio of the control samples. The regression analysis was conducted by using software (Origin). The regression analysis was also conducted with this software.

3.4. Results and Discussion

3.4.1. Glucose Detection by MIP-PANI Paper Sensors

As shown in Figure 24, the peaks around 3500 to 3800 cm^{-1} in the FTIR spectra correspond to the presence of O-H bonds of glucose. The intensity of the peak of the paper strip with 12 mM glucose was significant compared to that with the 0 mM sample (as control). The noise presented in this range might be attributed to moisture in the air. The result indicate that the glucose was captured and recognized by the PANI paper strip.

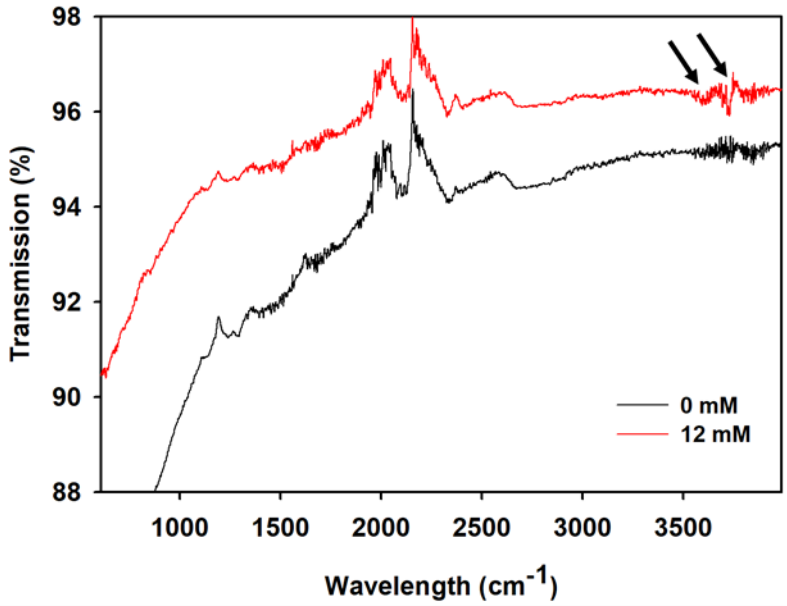

Figure 24 FTIR transmission result of the PANI paper strips after being dispensed with 0 mM (black line) and 12 mM (red line) of glucose in DI water solutions, respectively. The black arrows indicate the presence of an O-H bond that is contributed by glucose.

The impedances of the PANI paper sensors at low frequency were measured as control. These sensors were labeled with numbers from 1 to 24 and the Re(Z) of each sensor were measured before dispensing the glucose blood sample solutions. The Re(Z)

distribution of these paper sensors is shown in Figure 25. The prepared paper sensors presented a narrow distribution (within the pink band) of the Re(Z) with a mean value of 0.850 kΩ and a standard deviation of 0.059 kΩ. The maximum and minimum Re(Z) were measured to be 0.736 and 0.955 kΩ, respectively. The median value was 0.842 kΩ. The results showed that the original real part of the Z of the prepared paper sensors was distributed narrowly within a stable range under low frequency condition.

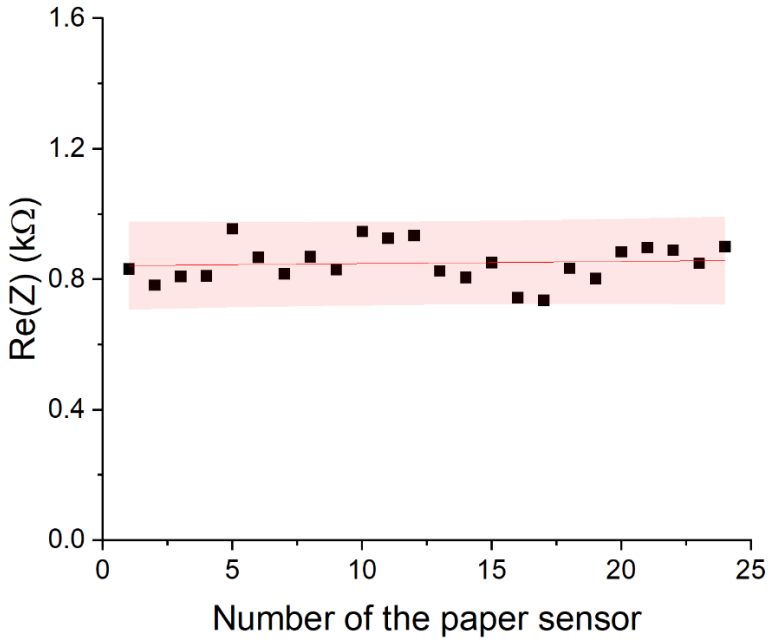

Figure 25 The real part of the original impedance of the prepared paper sensors. The red line represents the average value. The pink band shows the resistance was distributed within a narrow range.

The DC characteristics of the PANI paper sensors were investigated with gradient voltage increases from 0 to 10 V as shown in Figure 26. The results indicate that the PANI paper strips showed a linear and homogenous resistive response under uniformly increased DC voltage conditions with small standard deviations. A smaller current was observed in the paper sensor with the glucose in the DI water sample dispensed compared to those

exposed in the air and with DI water only. A relatively large standard deviation was observed with the sensor dispensed with the glucose in the DI water sample.

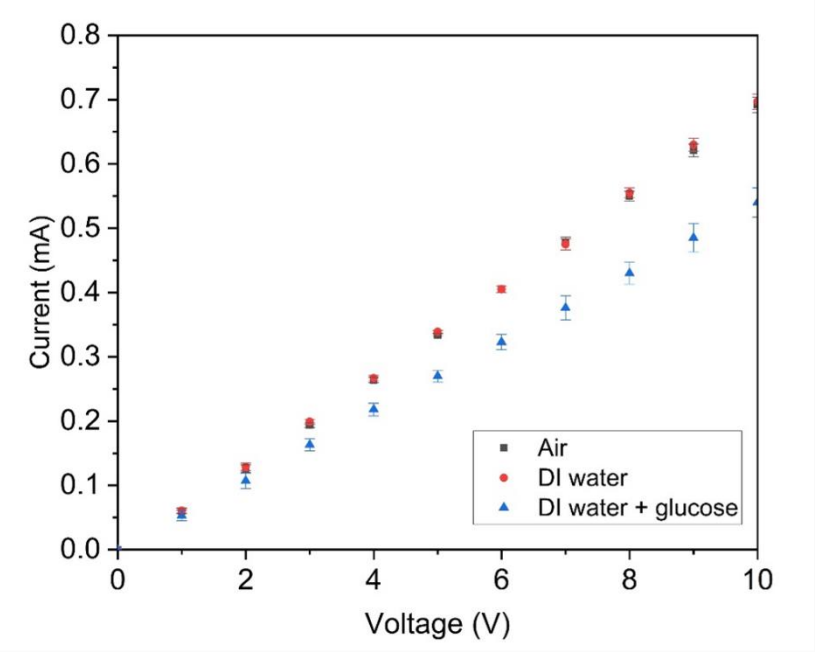

Figure 26 I-V curve of the PANI paper sensors. Each point represents an average of measurements of three identical PANI paper strips. The error bars represent the standard deviations of the three measurements. The black square, red circle and blue triangle represent the measurements under air, DI water and 12 mM of glucose in DI water.

Samples with glucose concentrations from 0 to 12 mM were prepared for investigating the sensor performance. Figure 27 shows a graphical representation of the resistance as a function of glucose concentration. This graph indicates a clear linear correlation between the resistivity of the sensor and the concentration of glucose in the sample. The correlation coefficient was estimated to be 0.989 by the software using linear regression. The linear regression model was obtained as $y = 0.0014x + 0.9993$.

The limit of blank (LOB) of glucose in DI water samples is calculated based on Equation (5)[121]:

$$\text{LOB} = \text{mean of blank} + 1.645\ (\text{SD of blank}) \quad (5)$$

where mean of blank is the average value at blank sample and SD of blank is the standard deviation of blank sample. The limit of detection (LOD) of glucose in DI water samples is calculated based on Equation (6)[121]:

$$\text{LOD} = \text{LOB} + 1.645\ (\text{SD of low concentration}) \quad (6)$$

where SD of low concentration is the standard deviation at low concentration sample. Based on the calculation, the LOD for the paper sensor with DI water samples is estimated to be 1.0048 mM.

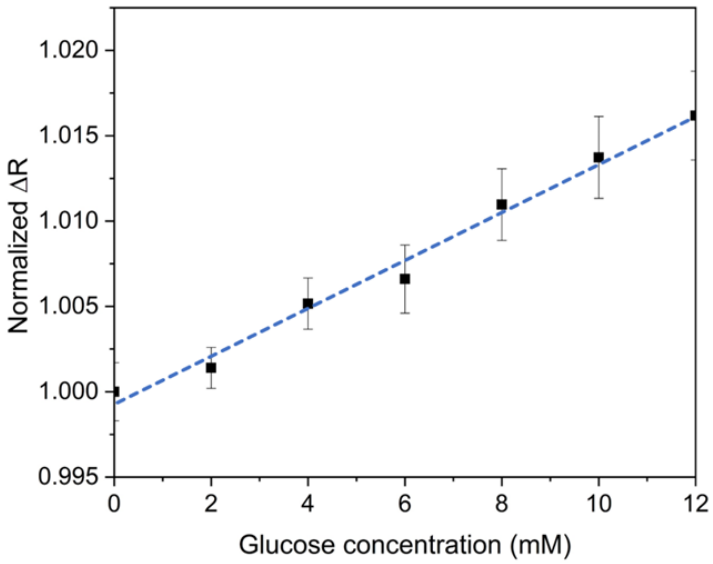

Figure 27 Graph of the normalized resistance change ratio as a function of glucose concentration in the DI water samples. The calibration curve (blue dash) of glucose concentration shows a linear correlation. Each point represents the average value of at least three identical tests in different paper sensors. The error bars are standard deviations calculated based on the resistance ratio measurements.

Figure 28 shows the photographic image for paper sensors with the blood samples dispensed on the PANI electrodes.

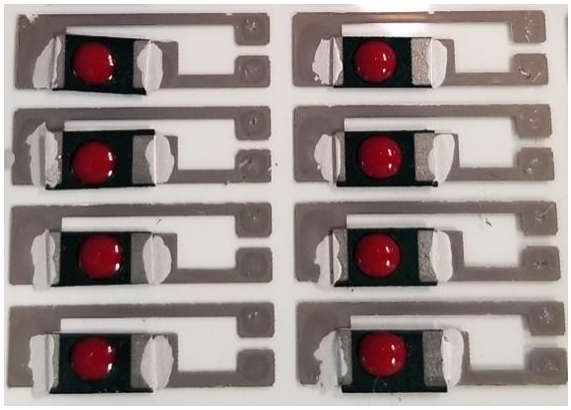

Figure 28 Photographic image of the paper sensor array devices after dispensing blood solution containing glucose.

As shown in Figure 29, the results for the determination of glucose concentration in the blood solutions indicated the linear increase of resistance changes as glucose concentrations increased. The result of this experiment also show that the normalized ratio of resistance change of the paper sensor was linearly correlated with the glucose concentrations ranging from 2.2 mM to 11.1 mM. However, the normalized resistance change was not significant due to low glucose concentrations of 0.1 and 0.5 mM. The glucose paper sensor showed a linear range of resistance ratio increase with a correlation coefficient of 0.984 with the added glucose concentrations ranging from 2.2 mM to 11.1 mM. In addition, the results show relatively large standard deviations compared to those in the DI water measurements.

The LOD of glucose detection in the blood samples was also studied by the same method mentioned in the DI water samples. Since the normalized resistance ratio at low glucose concentrations was not significant, the linear regression analysis was applied in the range of 2.2 to 11.1 mM of the added glucose. The linear model was obtained as $y = 0.0651x + 0.8381$. The LOD of the paper sensors in the blood samples was estimated to be 1.1713 mM.

The glucose detection mechanism can be simply explained by the change of resistivity if glucose binds to the MIP recognition sites on the PANI strips. For the detection of glucose in DI water (pH around 7), glucose captured on the PANI strips prevents holes from freely moving on the PANI surface. In this case, the decrease of the hole concentration in PANI results in the increase of the resistance as shown in Figure 27. With the same mechanism, the resistance increases linearly for a certain range of glucose concentrations as shown in Figure 29.

The I-V curve of the paper sensor with the glucose in the DI water sample dispensed showed reduced values compared to those exposed in the air and with DI water. The decrease of current indicated an increase in the resistance of the paper sensor at the given voltage. This is attributed to the binding of glucose when dispensing the glucose in DI water solution onto the paper sensor.

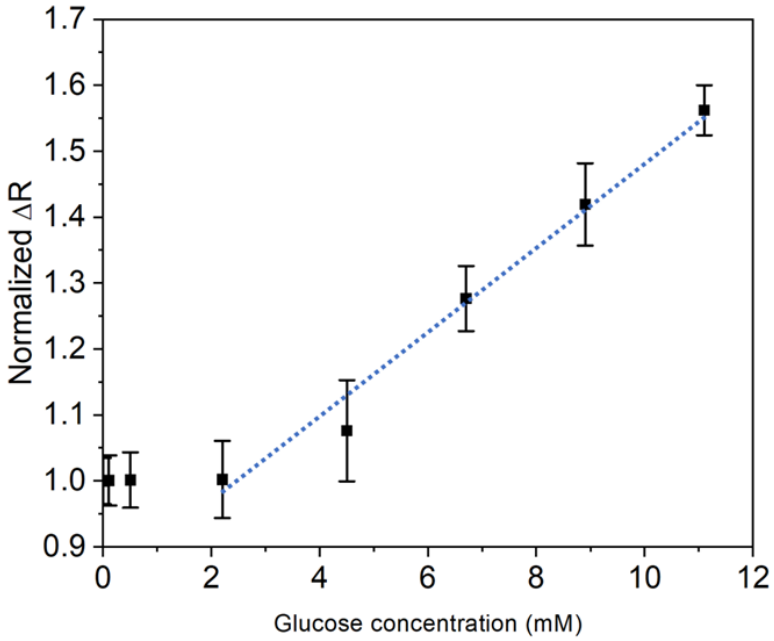

Figure 29 Graph of the normalized resistance change ratio as a function of the added glucose concentration in the bovine blood sample. The calibration curve (blue dash) of glucose concentration shows linear correlation ranging from 2.2 to 11.1 mM. Each point represents an average of at least three identical tests on different paper sensors. The error bars represent the standard deviations calculated based on the resistance ratio measurements.

The normalized ΔR for each glucose concentration measured in blood samples presents much higher standard deviations than those measured in DI water. This is due to the complexity of blood samples dispensed on the polymer electrode. The glucose recognition sites could also be captured with molecules in the blood with similar size, shape, and charge as glucose, which might cause large standard deviations in glucose concentration determination. Additionally, the measurement was conducted 5 min after dispensing the sample solution, allowing more small molecules other than glucose to be captured on the polymer electrodes, which results in large deviations and a signal increase

in the resistance measurement. In addition, blood cells or large biomolecules that tend to attach on the surface of the paper sensor might also affect the results.

The proposed PANI paper sensor is promising as disposable paper strips for glucose sensing. MIP-based glucose detection approach using expensive graphite/nanoparticle composites[101, 103] requires multiple fabrication steps and increases the cost sharply. A gate-electrode by MIP method was also reported, but the additional electrode increases the cost of the sensor[104]. The proposed paper sensor provides a low-cost routine assay to diabetic patients with a moderate detection limit. Furthermore, the paper sensor is enzyme-free, which enables a long shelf-time with stability and durability when exposed to temperature and pH variations.

A limitation of the work could be the detection limit of the paper sensor, which hinders the application in very low-concentration situations. Furthermore, the reaction time is longer compared to traditional electrochemical glucose sensors in several seconds. Moreover, the dimensions of the paper strips could be optimized. Future work will be focused on improving the sensitivity of the paper sensor and the miniaturization of paper sensors which could further reduce the cost.

In this work, we developed and demonstrated a molecularly imprinted paper biosensor that has great potential as a low-cost alternative to determine blood glucose levels. The linear resistance response of the paper sensor strip can provide a low-cost, highly durable, and accurate glucose measurement method in blood. Other benefits of the paper-sensing strips include much lower temperature and humidity dependence that allows for a longer shelf life and ease of fabrication. On the contrary, GOx based sensors are more

susceptible to temperature and pH fluctuations. The low-cost fabrication, accurate, and reproducible detection of paper sensor results can provide a new way of determining glucose concentration in the blood of diabetic patients.

3.5. Other Biomarker Detection Applications

3.5.1. Cardiovascular Disease Biomarker C-Reactive Protein Detection

C-reactive protein (CRP) was first discovered and described as the first acute-phase protein in 1930.[122] It has a molecular weight of approximately 115,000 with five identical non-glycosylated subunits associated as a flat cyclic pentameric disc.[123] Generally, CRP has been used as a sensitive biomarker of inflammation, and more recently, as a prognostic indicator of cardiovascular diseases (CVD).[124, 125] It also has been proven in multiple prospective studies to predict tissue necrosis, infections, surgery, cancers, and peripheral arterial disease.[126-128] Three CRP levels have been classified[129, 130]: low risk (<1 mg/L); average risk (1–3 mg/L); and high risk (>3 mg/L). A low-cost and instantaneous monitoring of CRP levels is critical for CVD clinical prognosis and diagnosis.

The basic biochemical reaction that constitutes CRP detection is the selective association of the protein with a specific analyte. As a result, conventional immunoassays techniques based on an antigen-antibody approach have been widely studied and applied. Enzyme linked Immuno-Sorbent Assay (ELISA) is the most used method.[131] Commercially available kit tests are used in most clinical procedures. However, this

method is expensive and limited to elevated concentrations of CRP. Enzymatic assays are also sensitive to pH and temperature, which requires carefully handling.

Emerging techniques based on the formation of plasmon and synthetic receptors by means of molecular imprinted polymer (MIP) are shown to be useful for the assessment of CRP with the advantage of low cost, rapid response and high sensitivity.[132, 133] Based on the general principle of molecular imprinting, monomers are polymerized in the presence of templates, followed by the removal of templates, leaving cavities/binding sites as complements to target analytes.[134-136] Conductive polymers are desirable as the MIP matrix due to their capability in electron-conducting through the bonding sites and matrix, leading the signal variation upon the recognition of target molecules. Polyaniline (PANI) is one of the most common conductive polymers that have been investigated and used in molecularly imprinted sensor applications.[119, 137-139] PANI is easy to synthesize by solution process on paper substrates, which promotes the development of portable and disposable paper-based device and dramatically reduces the cost. What's more, the excellent environmental durability and availability for operating in aqueous phase make PANI one of the best candidates among molecularly imprinted conductive polymers.[140]

In this part, a low-cost paper-based CRP sensor was prepared by molecularly imprinted polyaniline (CRP-MIP-PANI). CRP-MIP-PANI was synthesized on paper substrates in the presence of CRP, followed by the removal of the template molecules from the polymer matrix. Electronic response was evaluated in terms of the direct current resistance of the paper sensor before and after exposure to various CRP levels. The calibration curve of the resistivity change ratio of the paper sensor as a function of the

CRP concentrations was studied. This simple and disposable CRP paper sensor is a promising approach to prognostics and diagnostics of CVD and capable of serving as a low-cost and accurate tool for point-of-care CRP monitoring.

The surface of the sensing area was characterized by FTIR spectrometry. The spectra of NIP-PANI and CRP-MIP-PANI are shown in Figure 30. The spectra of both show the main bands at the wavenumber of 1590, 1508 and 1308 cm^{-1}, which correspond to the ring-stretching vibrations of the quinoid and benzenoid rings of aniline and nitro aniline, respectively.

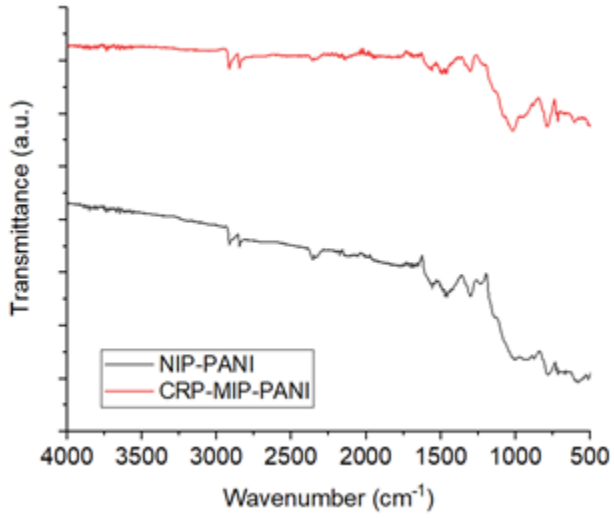

Figure 30 FTIR spectra of the CRP-MIP-PANI (red) and NIP-PANI (black). The transmission percentages are adjusted to arbitrary unit to compare the characteristic peaks.

The normalized $\Delta\rho$ as a function of the CRP concentration is shown in Figure 31. The normalized $\Delta\rho$ of the paper sensor shows a negatively linear correlation to the increase of the CRP concentration.

The fitted model of detecting CRP by the CRP-MIP-PANI paper sensor is

described by the following linear regression equation (5),

$$y = -0.0205x + 1.0034 \quad (7)$$

with the coefficient of determination (R^2) of 0.987. According to equation (3) and (4), the LOD of CRP-MIP-PANI paper sensor is estimated to be 0.390 mg/L.

As comparison, CRP concentration determination was also conducted with the NIP-PANI paper sensors. Similarly, the fitted model of the NIP-PANI paper sensors is shown in the equation (6),

$$y = -0.0053x + 0.9915 \quad (8)$$

with the R^2 to be 0.918. The LOD in the NIP-PANI paper sensor is estimated to be 7.64 mg/L accordingly.

The results show the CRP-MIP-PANI paper senor has much smaller LOD compared to the NIP-PANI one. The resistivity ratio of the CRP-MIP-PANI paper sensors presents larger decrease than that of NIP-PANI paper sensors when exposing to increased CRP concentrations, which suggests that the CRP-MIP-PANI obtained higher sensitivity than the NIP-PANI.

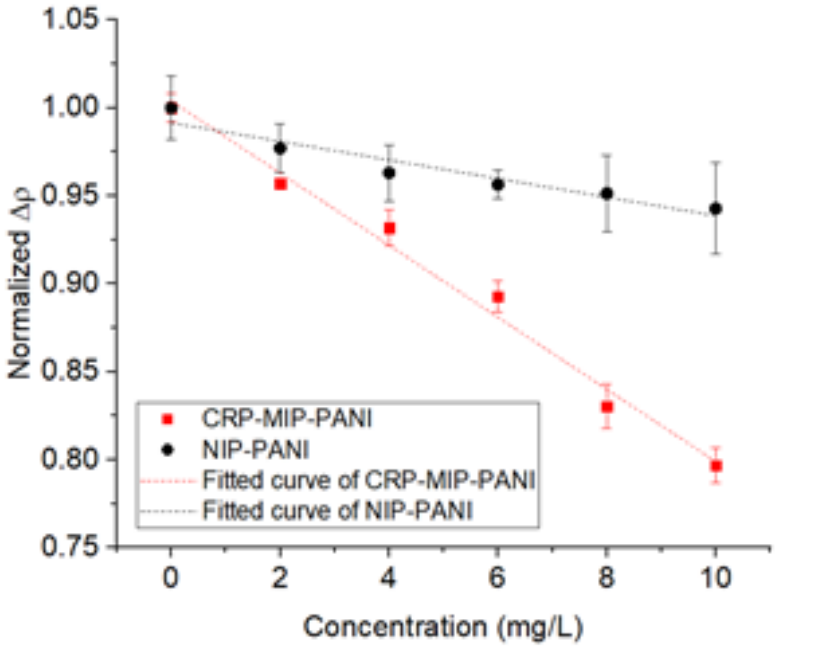

Figure 31 The resistivity ratio of the CRP-MIP-PANI (red square) and NIP-PANI (black circle) paper sensors exposed to various CRP concentrations. The red and black dash lines are the fitted calibration curves. Each point represents the average value of at least three identical measurements. The standard deviations are calculated and marked as the error bars.

3.5.2. Methylmalonic Acid Wireless Detection

In the past years, Methylmalonic acid (MMA) have been investigated as the biomarker for vitamin B12 deficiency. The accepted values of MMA in healthy humans are between 73 nM and 271 nM for vitamin B12.[141] MA detection is mostly conducted by conventional methods, liquid chromatography mass spectroscopy (LCMS)[141, 142] or gas chromatography mass spectroscopy (GCMS).[143] However, this approach requires extensive sample pre-treatment and large sample volume. It is also expensive and time consuming. Recently, MMA has been reported to promote tumor progression due to age-induced accumulation.[144] This research pointed out that MMA could be of vital

significance as a potential biomarker for cancer prognostics and diagnostics. MMA concentration in aged people could be as high as 80 µM. Nevertheless, most of the current research is focused on a small dynamic range. MIP approaches have been reported to sense MMA with selectivity, but the narrow linear detection ranges limit their application for high concentration MMA detection.[145, 146] Hence, simple, low cost and large linear range is in urgent need for MMA detection as a promising prognostic and diagnostic biomarker for cancer and vitamin B12 diagnostics.

When synthesizing MIP-PANI paper strips, MMA was employed as the template during the co-polymerization process. The MMA-MIP-PANI paper sensor was fabricated following the same method mentioned above. The resistance ratio change was measured by the multimeter. In the meanwhile, the sensors were also measured by a wireless Pokitmeter and the signals was read out through a cellphone. Figure 32 shows that MMA-MIP-PANI paper sensor can detected MMA with a wide linear range from 0 to 100 µM with a positive correlation with the increase of the MMA concentration. The resistance was also verified by a Pokitmeter with wireless signal readout. This also demonstrates this MIP-PANI paper sensor can be integrated with a mobile-based platform for wireless and portable sensing applications in the future.

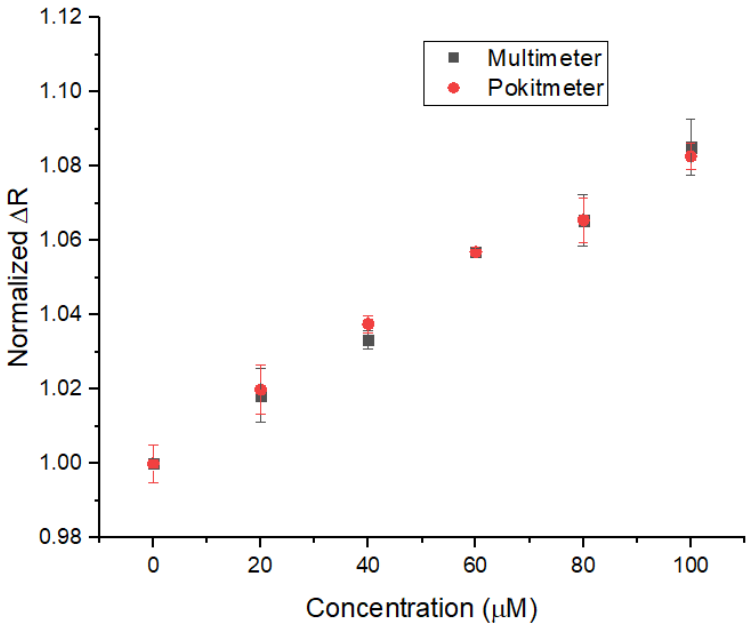

Figure 32 Normalized resistance ratio change with MMA concentration increase from 0 to 100 μM. The black squares represent data collected from a conventional multimeter. The red dots represent data measured by a wireless portable Pokitmeter. All data points represent the average value of at least three measurements with standard deviations.

3.6. Summary

In summary, the MIP-PANI paper sensors have broadened point-of-care applications in biomarker detection with advantages of being low-cost and enzyme-free. We developed and demonstrated a molecularly imprinted paper biosensor that has great potential as a low-cost alternative to determine various chemicals and biomarkers such as glucose, CRP, and MMA. This paper sensing platform can be also applied to detect environmental contaminates per- and polyfluoroalkyl substances (PFAS) such as perfluorooctanoic acid (PFOA) and perfluorooctanesulfonic acid (PFOS). The glucose LOD of the paper sensors in the bovine blood samples was estimated to be 1.1713 mM.

The CRP LOD of the CRP-MIP-PANI paper sensor was estimated to be 0.390 mg/L with the R^2 to be 0.987. This low-cost paper-based sensing platform is also applied to the detection of MMA with wireless signal readout with a wide linear range. The linear resistance response of the paper sensor strip can provide a low cost, long durable, and accurate analyte measurements method in blood and aqueous solutions.

4. MULTIPLEXED BARCODE HYDROGEL SENSING PLATFORM

4.1. Introduction

Biosensing technologies capable of simultaneously measuring multiple biomarkers associated with chronic diseases such as cancer, diabetes, cardiovascular disease, and chronic kidney disease are important to the future of personalized medicine, telemedicine, and can drastically improve the way healthcare is delivered.[147, 148] Multianalyte biosensors can provide even more comprehensive patient health insights that would allow for more efficient and tailored therapies that can lead to reduced healthcare costs and improved patient outcomes.[149] In addition to their role in personalized medicine, multianalyte biosensors can also be used to improve the accuracy and reliability of physiological measurements by providing redundancy even in biosensor systems intended to track a single disease.

4.1.1. Overview of Multianalyte Biosensors

Various types of multianalyte biosensors have been reported in the literature with applications in biotechnology,[150, 151] the nutrition industry,[152, 153] environmental analysis,[154, 155] and healthcare,[156] among others.[157-160] Multianalyte biosensors used in healthcare applications target a wide range of biomarkers associated with various pathological conditions, such as cancer, cardiovascular disease, and diabetes;[161-163] from a variety of biofluids including blood, interstitial fluid, saliva, and tear fluid.[158] Numerous signal transduction and detection techniques have been explored in the development of

multianalyte biosensing.[139, 164-169] Of the various modalities, enzymatic electrochemical biosensors are among the most common kinds of multianalyte biosensors. These systems operate by detecting a by-product of the reaction of an enzyme and an analyte. Due to the prevalence of diabetes mellitus around the world, multianalyte biosensors capable of the simultaneous measurement of glucose as one of the key target analytes are among the most widely studied.

Central to the development of multianalyte electrochemical biosensors are the selection of enzymes for use as a bioreceptor, which allows for the specific detection of target analytes of interest. Such systems have caught the interest of various research groups. One such ex vivo electrochemical multianalyte biosensor based on the immobilization of multiple enzymes in an electrode array was demonstrated by Yan et al.[170] Similarly, a multianalyte biosensor capable of glucose and uric acid detection using dual channels for individuals suffering from diabetes and gout was developed by Guo and Ma.[171] Another multi-enzyme sensor, developed by Perdomo et al, succeeded in detecting L-lactate and glucose using silicon chips with flow channels and achieved linear analyte responses in physiological ranges.[172] Similarly, Kotanen et. al, also developed a lactate and glucose dual biosensor using an electropolymerization biofabrication technique.[173] Lin et. al, also developed a microfluidic chip with a solid-state sensor capable of the simultaneous detection of glucose, urea and creatinine in human blood serum. This system used enzymes immobilized in alginate microbeads along with a magnetic powder to create a modular system to electrochemically measure the concentrations of target analytes.[174] Multianalyte biosensors are also very well suited for pathologies such as cardiovascular

disease where various metabolites are needed to be measured. These include immunoassays capable of the simultaneous detection of cardiac troponin I (cTnI) and C-reactive protein (CRP)[175] and a multianalyte immunoassay capable of detecting MMP-9 and IL-6 for ischemic stroke detection.[176]

While many multianalyte electrochemical biosensors perform well in ex vivo applications, they are generally not well suited for implantation applications due to the presence of interferents in vivo, the difficulty of transdermal signal transduction, and the difficulty of miniaturizing the electronics into an integrated biocompatible form factor suitable for implantation. Many electrochemical biosensors are vulnerable to interferences because the electrodes used for analyte detection are often not specific.[177] Many of these systems rely on the enzyme-induced oxidation of the metabolite and reduction of the electrode, which may be vulnerable to interferents. One such ex vivo electrochemical multianalyte biosensor based on the immobilization of multiple enzymes in an electrode array was demonstrated by Yan et al.[170]

What's more, commercially available transcutaneous electrochemical sensing products also suffer from drawbacks such as invasiveness, high expense, and the need for frequent sensor replacements. The first continuous glucose monitoring (CGM) device Dexcom G6 lasts only about 10 days before expiration. These sensors are required to be inserted beneath the skin to measure glucose levels and cost about $150 per sensor on average. Furthermore, all the devices are prone to the dislodging of the cannula from motion due to the soft tissue environment. Additionally, various drugs can falsely alter the

glucose reading for CGM's. These drawbacks offer a lot of room for improvement in reliably providing glucose data to patients.

Optical implantable multianalyte biosensors present possible solutions to these issues. A multianalyte optical biosensor capable of detecting changes in glucose, uric acid, urea, and creatinine by fluorescent intensity was reported by Tsai and Doong.[178] In this system, hydrolase and oxidase enzymes, along with horseradish peroxidase immobilized using a sol-gel method.[178] However, the detection of this array biosensor depends on two different principles based on the pH change and the reduction of the Am red reagent. The fluorescent readout could be affected by the possible fluctuation of the environment and defocusing issues. What's more, the violet excitation light cannot penetrate the tissue far enough, which further limits its application in implantable continuous multianalytes monitoring under deep dermal layer.[179]

4.1.2. Significance

Herein, we present a multianalyte optical biosensor platform based on oxidoreductase enzymes coupled with oxygen-sensitive metalloporphyrin phosphors immobilized within nanofilm-coated alginate microparticles embedded in discrete compartments of a barcode hydrogel implant made of poly(ethylene glycol) diacrylate (PEGDA). The biosensing assay, which was previously developed by McShane et al., indirectly detects changes in analytes through oxidase-induced local oxygen depletion to produce changes in phosphorescence lifetime via the oxygen-sensitive phosphors.[180] Therefore, by changing the selection of oxidase enzymes used in the assay, the system can

be used to target various analytes of interest and in the development of multi analyte biosensors. Particularly, since the immobilized phosphors are collisionally quenched in the presence of oxygen, the reduction in oxygen results in an increase in phosphorescence lifetime that is used to calculate the concentration of the analyte of interest. A key advantage of measuring phosphorescence lifetime instead of luminescence intensity is the capability to conduct transcutaneous interrogation more effectively without significant optical interference from autofluorescence and background noise. This is especially valuable in the development of implantable biosensors where scattering and light absorption from the surrounding tissue is likely to be a factor.

In this work, we demonstrate the capability of a multianalyte optical sensing platform to encapsulate discrete assays into an implantable and biocompatible hydrogel system fabricated using a soft lithography technique. To demonstrate the capability of the system to target unique analytes with minimal crosstalk, oxygen and glucose were selected as the initial target analytes. The time-lapse fluorescent intensity of the oxygen and glucose sensing compartments was studied and analyzed under different oxygen concentration conditions. To measure the system response to glucose and oxygen changes, the phosphorescence lifetime as a function of oxygen and glucose concentration were also studied. Overall, this multiplexed and implantable barcode hydrogel platform has great potential in the diagnosis, monitoring, management, and treatment of various pathological conditions and can be a valuable tool in personalized medicine.

4.2. Materials and Methods

4.2.1. Materials

Poly(ethylene glycol) diacrylate (PEGDA, average Mw ~ 3.4 kDa) was purchased from Alfa Aesar (Haverhill, MA, USA). 2,2- dimethoxy-2-phenylacetophenone ($C_6H_5COC(OCH_3)_2C_6H_5$, >99%), 1-vinyl-2-pyrrolidinone (C_6H_9NO, >99%) were obtained from Sigma-Aldrich (St. Louis, MO, USA). The two phosphors, Pd(II) meso-Tetra (sulfophenyl) Tetrabenzoporphyrin Sodium Salt (Group A, Hulk) and Pd(II) meso-Tetra(4-carboxyphenyl)porphine) (Group B, PdP) were obtained from Frontier Scientific (Logan, UT, USA). Glucose oxidase from Aspergillus Niger was obtained from BBI solutions (Cardiff, UK) while catalase from bovine liver was obtained from Calzyme Laboratories, Inc. (San Luis Obispo, CA, USA). Alginic acid sodium salt, poly(allylamine hydrochloride) (PAH, average Mw ~ 17.5 kDa), poly(sodium-4-styrenesulfonate) (PAH, average Mw 70 kDa), calcium carbonate, TRIZMA Base (Tris[hydroxymethyl]aminomethane), and dimethyl sulfoxide (DMSO) were purchased from Sigma Aldrich (St. Louis, MO, USA). The surfactant, Sorbitan trioleate (SPAN 85), was obtained from Tokyo Chemical Industry (Tokyo, Japan), while polyoxyethylene sorbitan trioleate (TWEEN 85) was obtained from Sigma Aldrich (St. Louis, MO, USA). 2,2,4-Trimethylpentane (isooctane) was purchased from Tokyo Chemical Industry (Tokyo, Japan). Tris HCl (Tris-(hydroxymethyl) aminomethane hydrochloride) was purchased from VWR (Radnor, PA, USA). Finally, calcium chloride ($CaCl_2$) and β-D-glucose were purchased from Macron Fine Chemicals (Center Valley, PA, USA).

4.2.2. Oxygen and Glucose Sensing Microparticle Synthesis

Two groups of alginate microparticles were fabricated for use in the barcode sensors, which contained two types of compartments and four compartments in total. The alginate microparticles placed in compartment Group A were designed for the detection of changes in glucose concentrations and oxygen concentrations while those in Compartment B Group were designed to be glucose irresponsive but oxygen responsive. A similar emulsion-based procedure was used to make alginate microparticles in both Group A (Hulk) and Group B (PdP). Here, alginic acid was combined with the porphyrin molecules Hulk and PdP to create the aqueous phase of the emulsion. The chemical structures are shown in Figure 32. For glucose-sensing particles, glucose oxidase (GOx) and catalase (CAT) were combined with this aqueous phase.

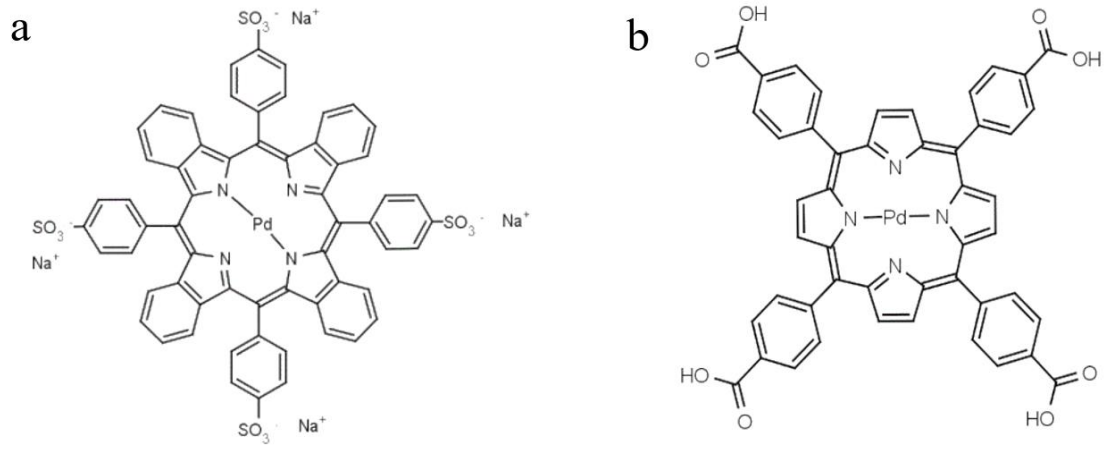

Figure 33 Chemical structures of the oxygen-sensitive metalloporphyrin phosphor molecules. (a) Group A, Hulk. (b) Group B, PdP.

The alginate-dye-enzyme mixture was then added to an organic phase of isooctane along with surfactants and emulsified using a homogenizer after the addition of surfactants

TWEEN85 and SPAN85, which stabilize the emulsion by reducing the surface tension of the microparticle droplets as they crosslink within the alginate microparticles. After the crosslinking of the microparticles, a 5-layer alternating nanofilm of poly (styrene sulfonate) (PSS) and poly (allylamine hydrochloride) (PAH) was deposited on the particles using layer-by-layer deposition. These microparticles were suspended in 1 mL TRIS buffer solution (50 mM) and stored at 4 ℃ for future use.

4.2.3. Barcode Hydrogel Sensor Fabrication

To create discrete compartments in a single barcode hydrogel, a bottom master mold and a top master mold were fabricated by replica molding polydimethylsilonxane (PDMS) from the master molds printed by a 3D printer (EnvisionTEC).[181, 182] Alignment markers were also designed and fabricated on the master molds for precisely matching the bottom and top master molds. PDMS precursor was prepared by mixing the prepolymer and curing agent at a ratio of 10:1. The solution was well mixed and degassed before casting into the molds.

The hydrogel solution was prepared by mixing 10% (w/v) PEGDA and 2% (v/v) photo-initiator solution. The photo-initiator solution was prepared by adding 2,2-dimethoxy-2-phenylacetophenone into 1-vinyl-2-pyrrolidinone with a concentration of 100 mg/mL. The bottom and top PDMS master molds were pre-treated with oxygen plasma for 2 min to make the surface hydrophilic. Immediately after the surface treatment, the hydrogel solution was loaded into the bottom master mold. The top master mold was aligned on top of the bottom master mold with the help of the alignment markers. Then,

the hydrogel polymerization was conducted by cross-linking under 365 nm ultra-violate (UV) exposure for 5 min. The barcode hydrogel with a 2x2 array of discrete compartments was peeled off the master molds and rinsed by deionized (DI) water (resistivity ~ 18.2 MΩ/cm) for at least three times.

The oxygen and glucose sensing assays were mixed with the hydrogel solution at a ratio of 3:1. The well-dispersed hydrogel and the sensing assay mixtures were loaded into each compartment with a volume of 0.64 μL by a pipette followed by the polymerization of the mixed precursors under 365 nm UV for 5 min. The as-fabricated barcode hydrogel containing multiplexed sensing assays were then rinsed by DI water for at least three times and kept in DI water at 4 ℃.

4.3. Experimental Section

4.3.1. Testing System

Each of the four barcode samples were tested in a single flow cell. Each barcode sample contained four compartments loaded with alginate microparticles, two of the four compartments contained alginate microparticles encapsulating Hulk dye and the two remaining compartments contained alginate microparticles encapsulating PdP dye. Although each of the four barcode samples was tested for responses to changes in oxygen concentration, three of the four samples were tested for changes in the lifetime of the Hulk dye using readers with an excitation wavelength of 630 nm while the last compartment was tested with a reader with an excitation wavelength of 530 nm to observe changes in PdP. For each oxygen concentration, the barcode samples were tested for roughly 90

minutes to allow for the normalization of oxygen concentration and for the phosphorescence lifetime to reach a steady state.

Absorbance and emission measurements were performed using an Infinite 200 PRO 96-well plate reader (Tecan, Männedorf, Switzerland). Radical crosslinking was initiated using a Blak-Ray B-100SP UV lamp from UVP (Upland, CA, USA). Flow-through experiments were conducted using peristaltic pumps (L/S 7550 pump drive), pump heads (Easy Load 3), and precision tubing (L/S Norprene Tubing A60 G, L/S 13, 50 ft) purchased from MasterFlex (Gelsenkirchen, Germany). Oxygen concentrations were adjusted using mass flow controllers (Type 1179A General Purpose Mass-Flo Controller) and a pressure control unit (PR 4000 F) from MKS Instruments (Andover, MA, USA). Optical interrogation of hydrogel samples was conducted using custom optical readers, described in previous studies.[183, 184] Each reader contained a red LED (Lumileds LUXEON Rebel, $\lambda ex = 630$ nm) for excitation and silicon photomultiplier tubes (SiPMT, SensL) for emission detection. During oxygen and glucose response testing, samples were housed in a custom designed Delrin flow cell capable of holding four hydrogel samples and four optical readers. Changes in oxygen concentration during the oxygen response tests were verified using an OX-500 oxygen microsensor and PA2000 picoammeter (Unisense, Aarhus, Denmark)

4.3.2. Optical and Fluorescent Images

The optical and fluorescent images of the barcode hydrogel sensor were taken by a Leica SP8 confocal microscope. The time-lapse fluorescent images of the barcode

hydrogel sensor with oxygen and glucose sensing compartments were analyzed. A chamber was created by two cover glasses with an adhesive spacer to confine the specimen. The barcode hydrogel sensor sample was put inside the chamber. DI water was first injected into the chamber so that the sample was immersed in an ambient oxygen concentration environment as control. Fresh glucose solution with a concentration of 100 mg/dL was then added into the chamber. The glucose sensing assays were excited by 630 nm and the wavelength of the emission filter ranges from 750 nm to 800 nm. The oxygen sensing assays were excited by 530 nm and the wavelength of the emission filter ranges from 660 nm to 700 nm. The total duration for taking the time-lapse fluorescent images was set as 2h with 654s interval. The mean fluorescent intensity of the glucose and oxygen sensing compartment with the same area of region of interest was analyzed by Leica Application Suite X core 3.7.4. 23463.

4.3.3. Microparticle Size Distribution

The size distribution of the microparticles was characterized by a Cellometer (Nexcelom Bioscience, Massachusetts, USA). The sample solution was prepared by diluting the microparticle stock solution at a ratio of 1:10 by TRIS buffer solution (50 mM) and well suspended. The concentration as a function of the size of the microparticles was plotted and analyzed.

4.4. Results and Discussion

4.4.1. Design and Working Principle

The schematic diagram of the barcode hydrogel sensor with discrete compartments containing oxygen and glucose sensing assays is shown in Figure 33a and the dimension of the barcode hydrogel is described in Figure 34. To achieve this target geometry, the bottom and top master molds were designed with the following parameters. The bottom PDMS master mold for the fabrication of the barcode hydrogel had arrays of hollow cuboid structures with the dimension of 3.5 mm in length, 3.1 mm in width, and 1 mm in height. The top PDMS master mold for the creation of the discrete compartments had arrays of bulge cuboids with the dimension of 1 mm in length, 0.8 mm in width, and 0.8 mm in height. The distance between each compartment was designed at 0.5 mm.

The schematic diagram of the microparticles is shown in Figure 33b. The two types of the sensing assays contain an aqueous phase emulsion by combining alginic acid with the porphyrin molecules Hulk and PdP followed by crosslinking to form microparticle droplets. Especially for glucose sensing assays, glucose oxidase (GO_x) and catalase (CAT) were added into the aqueous phase. GO_x serves as a highly selective bioreceptor while CAT reduces hydrogen peroxide (H_2O_2), which is known to deactivate enzymes such as GO_x.[185] Polyelectrolyte multilayer (PEM) thin films were coated on the surface of these microparticles to control oxygen and glucose diffusion. A 5-layer alternating nanofilm of poly (styrene sulfonate) (PSS) and poly (allylamine hydrochloride) (PAH) was deposited by a layer-by-layer deposition approach. The size distribution of the microparticles is shown in Figure 35.

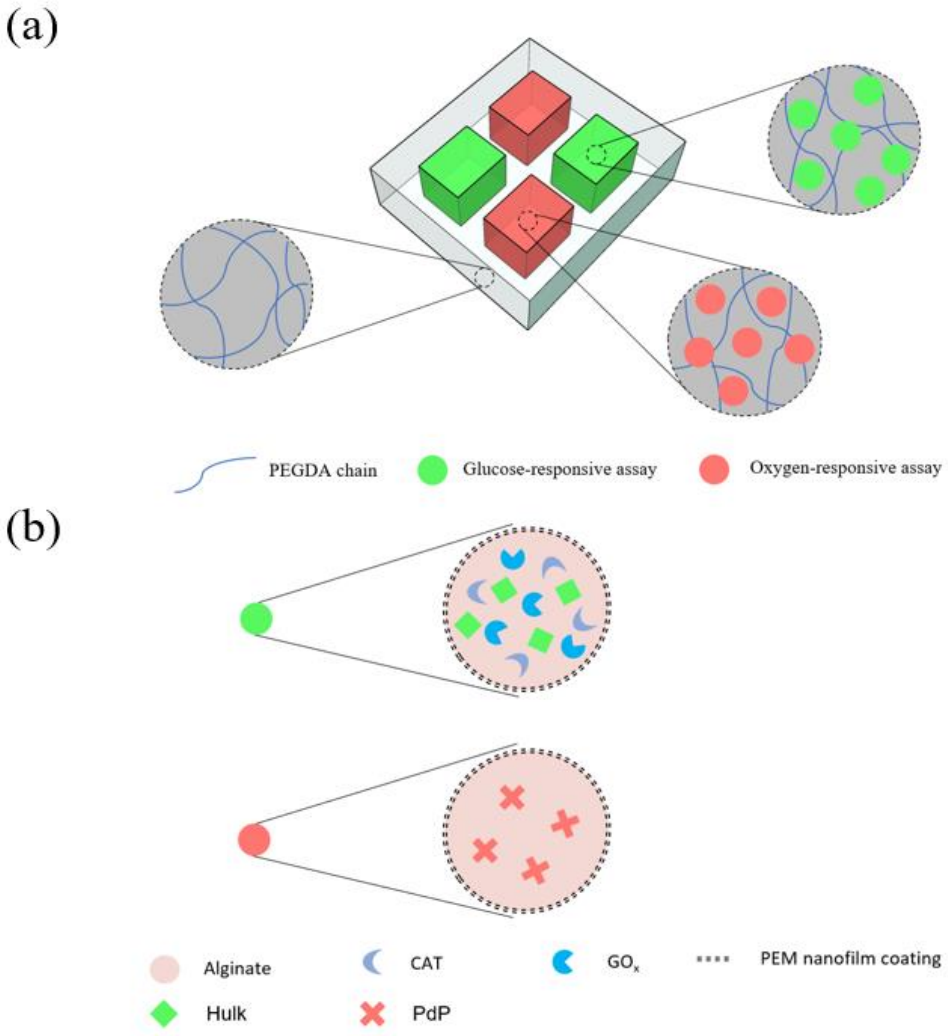

Figure 34 Schematic diagram of the barcode hydrogel platform. (a) The 2x2 array barcode hydrogel sensor. (b) The composition and structure of the glucose-responsive (green) and oxygen-responsive (red) microparticles.

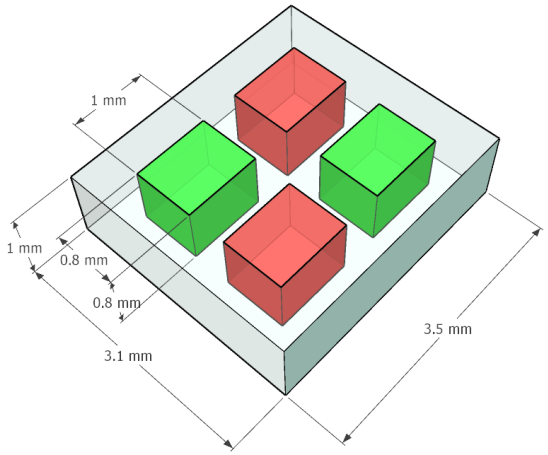

Figure 35 Dimension of the 2x2 array barcode hydrogel platform.

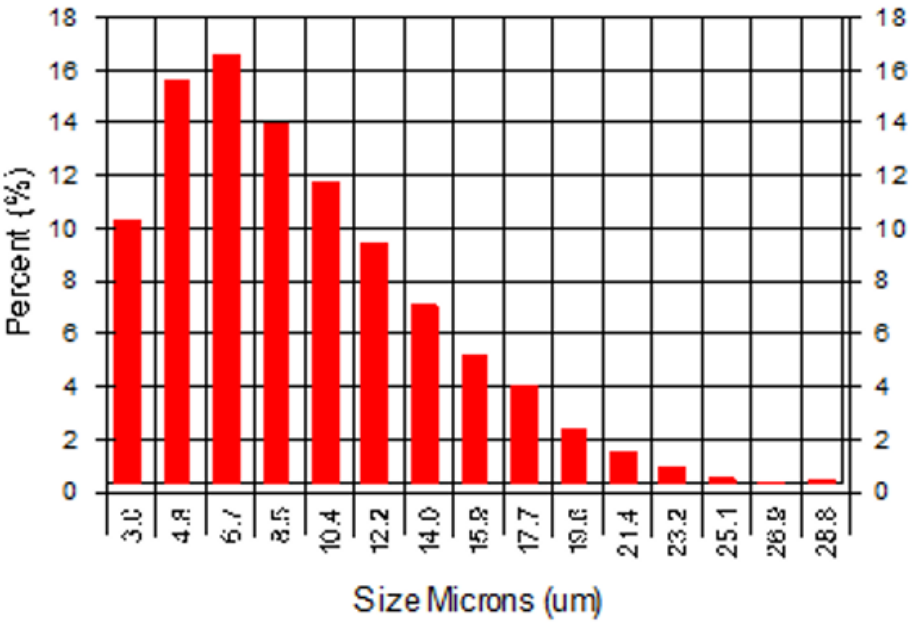

Figure 36 Size distribution of the synthesized microparticles.

For a 2x2-array barcode hydrogel platform, four discrete compartments were created by replica molding using soft lithography from the top and bottom master molds printed by a 3D printer The side view of the fabrication process flow is shown in Figure 37, more details are described in the experimental section. A photographic image of the as-fabricated barcode hydrogel sensors was shown in Figure 37f.

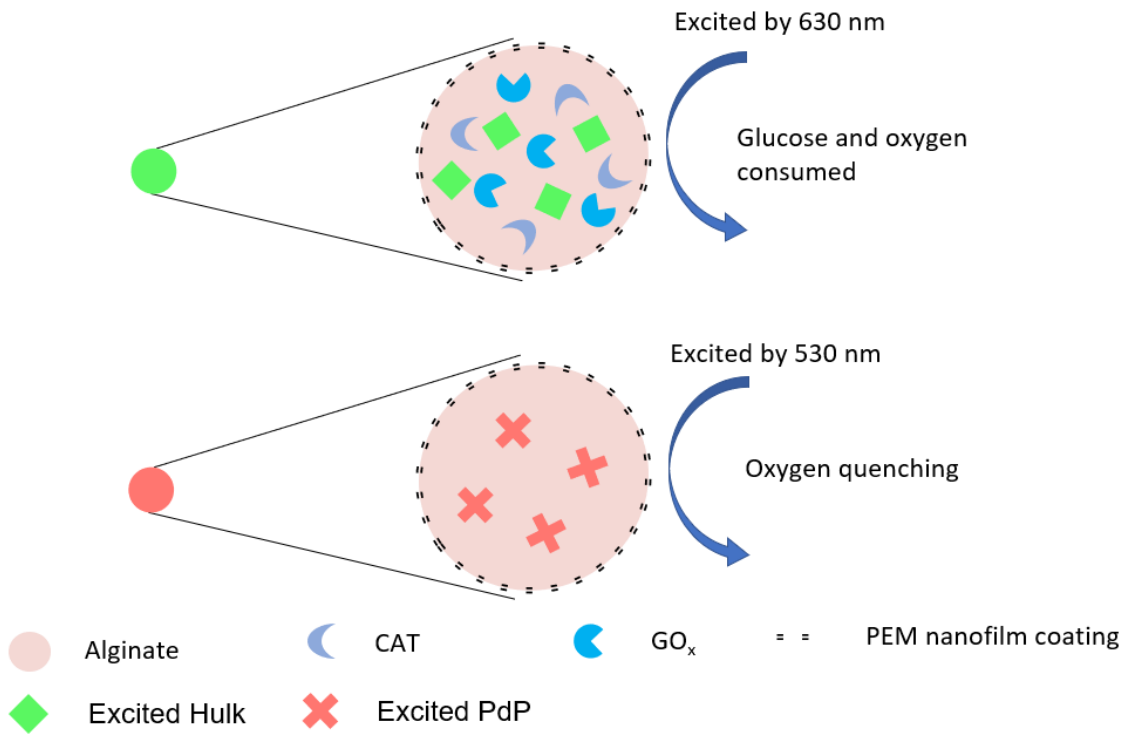

Figure 37 Schematics of the working principle of the glucose-responsive (green) and oxygen-responsive (red) microparticles.

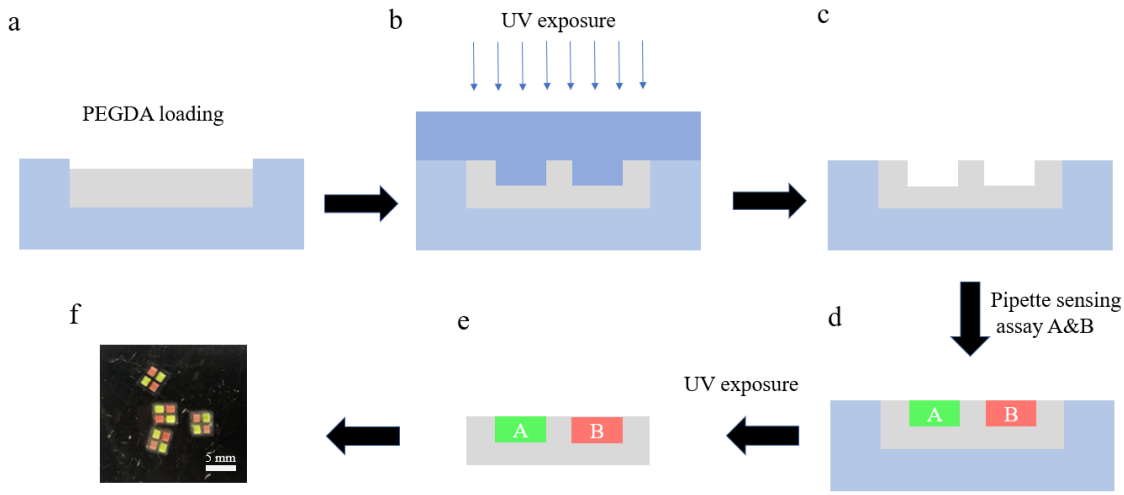

Figure 38 Fabrication process flow of the barcode hydrogel sensor. (a) Load PEGDA precursor solution into the bottom mold. (b) The top mold was aligned with the bottom mold. The PEGDA solution was crosslinked by UV exposure. (c) Removed the top mold. Discrete 2x2 array of compartments were formed in the hydrogel. (d) Multi-sensing assays (A: glucose, B: oxygen) mixed with PEGDA solution were pipetted into each compartment. (e) The oxygen and glucose sensing assays were crosslinked by UV exposure. (f) A Photographic image of the 2x2 barcode hydrogel sensors containing discrete oxygen and glucose sensing compartments. Scale bar, 5 mm.

4.4.2. Brightfield and Fluorescence Images

The dimension of the single barcode hydrogel with 2x2 arrays was confirmed by the top view microscopic image was shown in Figure 38a. The color image was also taken and presented in Figure 38b. The glucose responsive compartments (Group A) were in dark green, and the oxygen responsive compartments (Group B) were in red. The confocal fluorescent image of each compartment was shown in Figure 38c, d, e, and f.

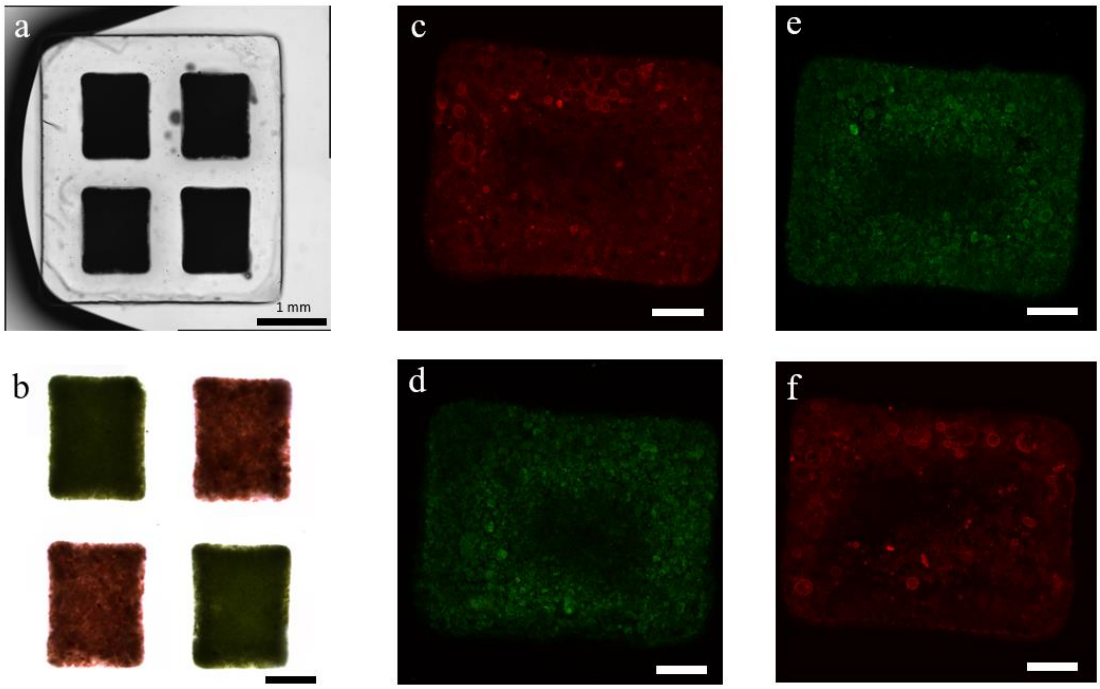

Figure 39 Brightfield and fluorescence images of the barcode hydrogel sensor. (a) Microscopic image of the barcode sensor immersed in DI water. Scale bar, 1 mm. (b) Color image of the barcode sensor. The green compartments contain glucose responsive assays, and the red compartments contain oxygen responsive assays. Scale bar, 500 µm. (c) and (f) The fluorescence images of the oxygen responsive compartments at the top right and bottom left. (d) and (e) The fluorescence images of the glucose responsive compartments at the top left and bottom right. Scale bars in (c), (d), (e), and (f): 200 µm.

The time-lapse fluorescence images in the oxygen and glucose responsive compartments were taken when the barcode hydrogel sensor was immersed in 100 mg/dL glucose solution in a sealed chamber. The mean fluorescence intensity was calculated by the average intensity in the region of interest minus the background mean intensity. As shown in Figure 39, the mean fluorescence intensity of the glucose responsive compartment increased about 23.6% after exposure to glucose solution for 2h. The mean intensity started to saturate after around 90 min. This is due to the consumption of oxygen

in the glucose responsive compartment when glucose was added in the sealed environment, it formed a low oxygen condition. When the porphyrin was quenched by oxygen, the fluorescence intensity increased as the oxygen concentration decreased. When the oxygen concentration became very low in the glucose responsive compartment locally, the mean intensity tended to be saturated as the oxygen concentration became constant. However, the mean intensity of the oxygen responsive compartment showed only about 7.2% increase, which suggests the oxygen concentration in the oxygen responsive compartment was barely affected by the oxygen consumption in the nearby glucose responsive compartments.

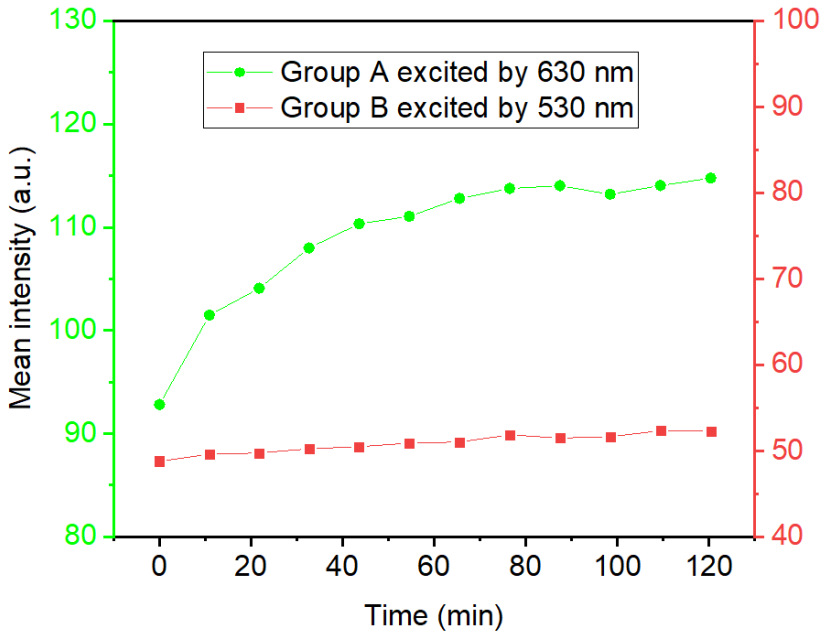

Figure 40 Time-lapse mean fluorescence intensity changes of the oxygen and glucose responsive compartments. The barcode sensor was immersed in glucose solution with a concentration of 100 mg/dL.

4.4.3. Multiplexed Oxygen and Glucose Sensing

The response of the barcode hydrogel sensors to the changes in oxygen concentrations was measured. Specifically, the phosphorescence lifetimes changes associated with both Group A and Group B compartments were analyzed as a function of oxygen concentration. An oxygen concentration ranging from 0 to 21% (0 - 206.8 μM) was used, to represent oxygen concentrations up to ambient oxygen levels.

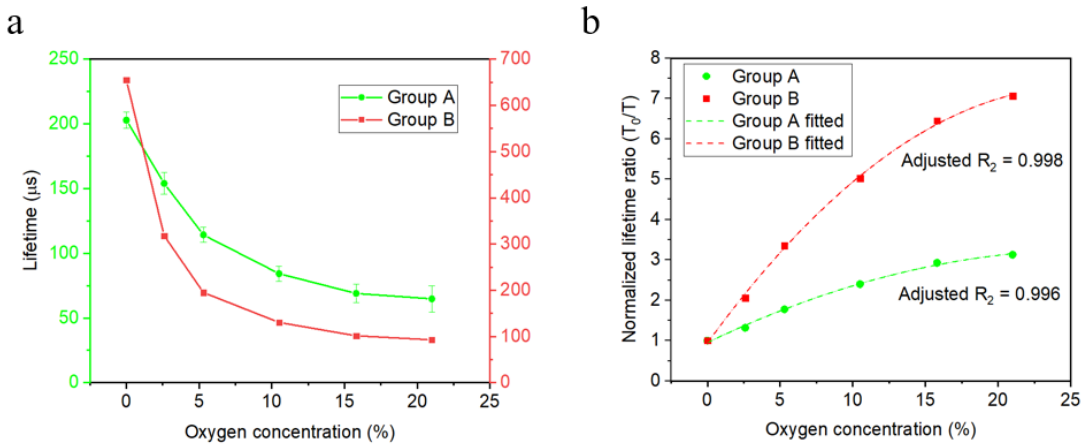

Figure 41 Phosphorescence lifetime response of the barcode hydrogel sensor under different oxygen concentrations. (a) Phosphorescence lifetime changes of the glucose (Group A, green) and oxygen (Group B, red) responsive assays under different oxygen concentrations. (b) Normalized lifetime ratio and the fitted curve associated with the two types of sensing compartments (Glucose in green color, oxygen in red color) as a function of oxygen concentration. Green circles represent an average of the phosphorescence lifetime response from Group A compartments from three identical samples while red squares represent compartments in Group B from a single barcode sample. Error bars represent the associated standard deviations.

Each barcode array consisted of four compartments, two compartments containing alginate microparticles loaded with Hulk dye and two compartments containing alginate microparticles loaded with PdP dye. The sensitivity of each barcode compartment to

oxygen is quantified by the Stern-Volmer constant, Ksv, which was calculated as the slope of the normalized oxygen response graph in Figure 40 and reported in Table 1.

Both Compartment Group A and B showed pronounced responses to the changes in oxygen concentration in Figure 6a as expected. However, the phosphorescence lifetime differed significantly between the two compartments due to the difference in the natural lifetime range of the phosphors contained in each compartment group. Compartment Group A, which contained Hulk (phosphor) and GO_x, showed a phosphorescence lifetime range of 65 to 203 μs (138 μs) and a K_{sv} value of 11.3 $(\%^{-1}\ O_2) * 10^{-2}$. Conversely, the oxygen sensitivity of Group B, which contained PdP (phosphor) and no GO_x, had a much higher phosphorescence lifetime range of 93 to 655 μs (562 μs) and a K_{sv} value of 32.4 $(\%^{-1}\ O_2) * 10^{-2}$. However, in both compartment types, the changes in phosphorescence lifetime are more pronounced in low oxygen concentrations and begin to plateau in higher oxygen concentrations, which is illustrated by the upward concave trends of normalized lifetime ratio seen in Figure 40b.

Table 1 Stern-Volmer constants of the oxygen- and glucose-responsive assays.

Group	**Phosphor**	$\boldsymbol{K_{sv}}$ **$(\%^{-1}\ O_2) * 10^{-2}$**
A	Hulk	11.3
B	PdP	32.4

The normalized phosphorescence lifetime ratios of the two types of sensing assays show positive correlations with oxygen concentration increasing. The normalized lifetime

ratio (T_0/T) of the glucose and oxygen sensing compartments were fitted by polynomial regression with adjusted R square of 0.996 and 0.998, respectively.

It should be noted that although the phosphorescence lifetime range for PdP was greater than Hulk, the later phosphor was selected for glucose sensing due to its near IR excitation wavelength (~ 630 nm), which is within the optical window where light absorption by both proteins and water is low.[186] Conversely, PdP has an excitation wavelength close to 530 nm, which would make in vivo excitation of the phosphor more difficult due to the absorption and scattering of light by pigments present in vivo. For clinical translation, it may be necessary to select phosphors that operate in the "optical window" (600 - 950 nm).

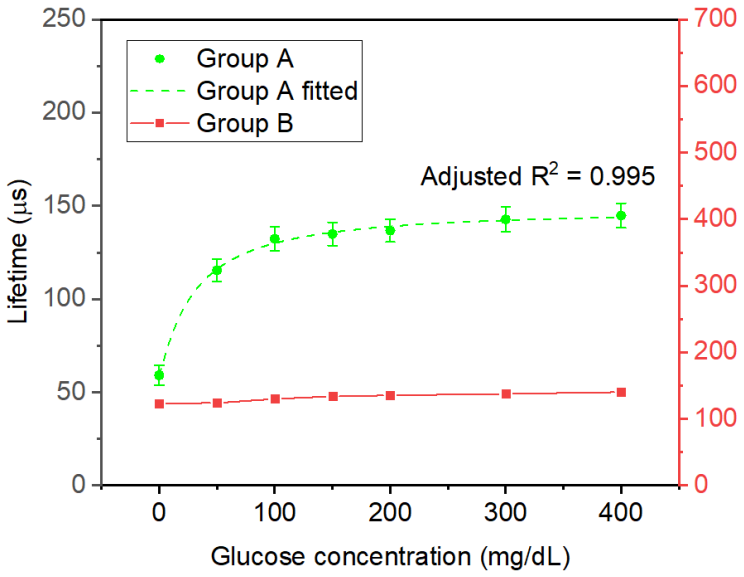

Figure 42 Phosphorescence lifetime response of the barcode hydrogel sensor under different oxygen concentrations. (a) Phosphorescence lifetime changes of the glucose (Group A, green) and oxygen (Group B, red) responsive assays under different oxygen concentrations. (b) Normalized lifetime ratio and the fitted curve associated with the two types of sensing compartments (Glucose in green color, oxygen in red color) as a function of oxygen concentration. Green circles represent an average of the phosphorescence lifetime response from Group A compartments from three

identical samples while red squares represent compartments in Group B from a single barcode sample. Error bars represent the associated standard deviations.

The glucose response was obtained by measuring the phosphorescence lifetime as a function of glucose concentration from the barcode sensors (Figure 41). Each barcode array consists of four compartments, two glucose-sensitive compartments (Compartment Group A) and two glucose-insensitive compartments (Compartment Group B). As expected, Compartment Group A showed a much more pronounced response (phosphorescence lifetime range: 86 μs) to changes in glucose concentration than Compartment Group B (phosphorescence lifetime range ~36 μs). It's worth noting that the natural lifetime range of PdP is much greater than that of Hulk as shown in Figure 41. As such, the lifetime responses during glucose challenges are better reported as a percentage change than an absolute phosphorescence lifetime change. Compartment Group A showed a 62% change in phosphorescence lifetime while Compartment Group B showed only a 6% change in phosphorescence lifetime. This is as expected and consistent with the time-lapse fluorescent intensity testing results mentioned in Figure 39.

Although Compartment Group A showed a significant increase in phosphorescence lifetime during glucose challenges, it does not achieve the lifetime range seen in the oxygen tests. This implies that the glucose response is enzyme-limited, as there is a plateau in the lifetime response lower than the maximum achievable lifetime, despite increases in glucose concentration. In other words, the enzyme-induced oxygen depletion by all available enzymes does not consume all local oxygen within the barcode

compartments. To achieve a higher lifetime range and achieve a higher lifetime range in future studies, the concentration of GOx can be increased.

A logistic regression model was used to fit the phosphorescence lifetime change as a function of glucose concentration with an adjusted R square of 0.995. The model is described as $y = 148.63 - 89.62/(1 + (x/30.36)^{1.12})$. The limit of blank (LOB) of glucose is calculated based on Equation (1):

$$\text{LOB} = \text{mean of blank} + 1.645\ (\text{SD of blank}) \quad (1)$$

where mean of blank is the average value at blank sample and SD of blank is the standard deviation of blank sample. The limit of detection (LOD) of glucose is calculated based on Equation (2):

$$\text{LOD} = \text{LOB} + 1.645\ (\text{SD of low concentration}) \quad (2)$$

where SD of low concentration is the standard deviation at low concentration sample. Based on the calculation, the LOD for glucose by the barcode hydrogel sensor is estimated to be 9.21 mg/dL.

The presence of a very low response in Compartment Group B also demonstrates a low level of crosstalk in the barcode system, since the glucose-sensitive compartment responded to the change in oxygen while the glucose insensitive compartment did not show a significant response.

4.4.4. Stability Assessment

Stability tests were conducted on the barcode sensor to evaluate the glucose response over multiple cycles. The barcode biosensors were exposed to 10 consecutive

cycles of 0 mg/dL glucose and 200 mg/dL glucose. Phosphorescence lifetime measurements were conducted throughout this process and the percent change in the phosphorescence lifetime response over the cycles was calculated. The samples were exposed to each glucose concentration for 1 hour to allow enough time for diffusion-reaction to reach a dynamic equilibrium (~10 mins) and data collection (30 mins).

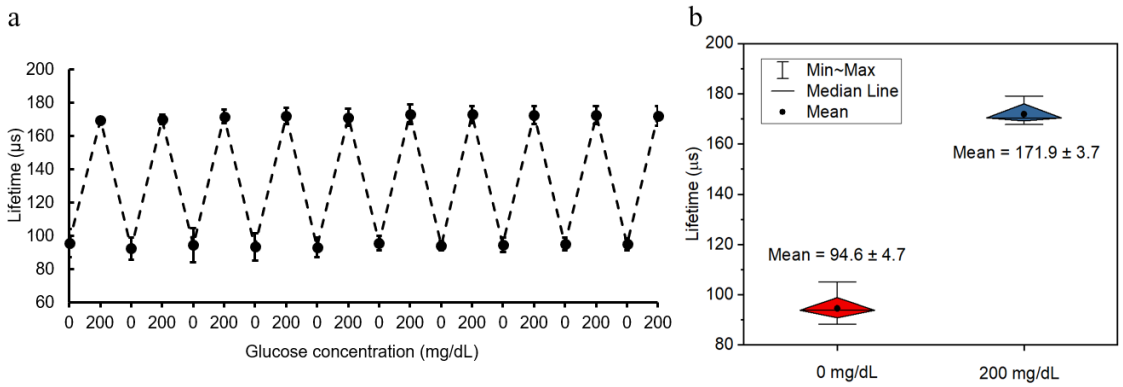

Figure 43 Stability assessment of the barcode sensors. Stability assessment of the barcode hydrogel sensor. (a) Each point represents an average of three samples. The phosphorescence lifetime was only collected from Compartment Group A of each barcode sensor. Each data point represents an average of the phosphorescence lifetime response of at least three identical samples. Error bars represent 95% confidence intervals. (b) Grouped box chart of the phosphorescence lifetime at 0 (red) and 200 (blue) mg/dL glucose concentration over 10 cycles. The diamond box represents 25 to 75% percentile.

This graph shows that the average phosphorescence lifetime rage gradually decreased and resulted in a 16% decrease in phosphorescence lifetime over the 10 cycles. A possible reason for the decrease in phosphorescence lifetime response is the deactivation of GO_x by H_2O_2, which is produced during glucose catalysis. To mitigate this phenomenon, catalase (CAT) was included in the sensing compartments. However, the emulsion-based fabrication method limited the amount of CAT that was used in particle

fabrication. A greater concentration of CAT might be necessary to further preserve enzymatic activity.

Figure 42a and b show no significant changes in the phosphorescence lifetime over the 10 cycles. Specifically, the phosphorescence responses to a 200 mg/dL glucose solution showed an average of 171.9 μs with a standard deviation of 3.7 μs in lifetime over 10 cycles while the phosphorescence responses to a 0 mg/dL glucose solution showed an average of 94.6 μs with a standard deviation of 3.7 μs in phosphorescence responses over 10 cycles. The relative stability of the barcode system may be due to the inclusion of catalase (CAT) in the sensing compartments. This enzyme has been reported to reduce the deactivation of GO_x by H_2O_2, which is produced during glucose catalysis.

4.5. Summary

In this study, an implantable optical sensing platform was developed based on oxidoreductase enzymes coupled with oxygen-sensitive metalloporphyrin phosphors immobilized within nanofilm-coated alginate microparticles embedded in discrete compartments of a single barcode hydrogel. The barcode hydrogel optical sensing platform was fabricated by replica molding from the master molds printed by a 3D printer. Optical and fluorescent images of the sensors were taken by a fluorescent microscope. Time-lapse mean fluorescent intensity of the barcode hydrogel sensor was studied and analyzed under different oxygen concentration conditions. Continuous oxygen and glucose monitoring were demonstrated by phosphorescence lifetime change of the metalloporphyrin phosphors in oxygen and glucose responsive compartment. The oxygen

responsive assays showed a constant phosphorescence lifetime while the glucose responsive assays showed increased phosphorescence lifetime with the glucose concentration increased from 0 to 400 mg/dL, which demonstrates no crosstalk between the nearby oxygen and glucose responsive compartments. Finally, the sensors were exposed to 10 consecutive cycles of 0 mg/dL glucose and 200 mg/dL glucose and demonstrated a good glucose response stability.

5. CONCLUSIONS

5.1. Summary

In the size selective microfluidic platform, we developed and demonstrated a size-selective microfluidic platform (ExoSMP) for automated, consistent, and reliable EV isolation. This unique platform offers an enhanced approach to the isolation of EV subgroups and sEV subpopulations, along with the additional advantage of being label-free, low-cost, and featuring a short processing time (< 1 h), and convenient integration with downstream analysis. This platform demonstrated a high recovery rate of 94.2% and reproducibility (a low standard deviation) from cancer cell culture media samples with an optimal sample flow rate. The size-selective isolation of EVs can easily be controlled by altering the pore sizes of the nanomembrane combinations.

Isolation of liposomes from mixed solution were validated. A size-selective liposome isolation platform was conclusively developed and demonstrated. Polystyrene beads (representative of large particles), liposomes (representative of exosomes) and IgG antibody (representative of proteins) in the initial solutions were successfully separated with a liposome recovery rate of 92.5% with short processing time of less than 2 h.

We further utilized ExoSMP with various combinations of nanomembrane pore sizes to demonstrate the isolation of EV subgroups and investigate sEV subpopulations of various size groups. The western blot analysis suggested the evidence of CD63 biomarker in the subgroups of the EVs. This improved technique will serve as a precise clinical tool for isolating EVs and addressing the heterogenicity of EV subgroups. Additionally, with

its efficient size-based isolation of EV subpopulations, ExoSMP shows broad promise for investigating the role of EVs in various point-of-care applications in disease monitoring, medical diagnosis, and drug delivery.

In the low-cost and enzyme-free paper sensor platform, we developed and demonstrated a molecularly imprinted paper biosensor that has great potential as a low-cost alternative to determine various chemicals and biomarkers. The linear resistance response of the paper sensor strip can provide a low cost, long durable, and accurate analyte measurements method in blood and aqueous solutions. Other benefits of the paper-sensing strips include much lower temperature and humidity dependence that leads to longer shelf life, easy to fabricate. The low-cost fabrication, accurate and reproducible detection of paper sensor result can provide a new way of the determination of glucose concentration in blood for diabetic patients. We have developed a paper-based electrical sensor with molecularly imprinted glucose recognition sites and demonstrated the determination of various glucose concentrations in bovine blood solutions. The sensing electrode is integrated with molecular recognition sites in conductive polymer. A calibration graph as a function of glucose concentration in aqueous solution has been acquired for each concentration and matched with a correlation coefficient of 0.989. We have also demonstrated the determination of glucose concentrations in bovine blood samples.

We have broadened the application of MIP technology to other biomarkers such as CRP and MMA. We developed and demonstrated CRP-MIP-PANI and MMA-MIP-PANI paper sensors. The results show the CRP-MIP-PANI paper senor has much smaller

LOD compared to the NIP-PANI one. The resistivity ratio of the CRP-MIP-PANI paper sensors presents larger decrease than that of NIP-PANI paper sensors when exposing to increased CRP concentrations, which suggests that the CRP-MIP-PANI obtained higher sensitivity than the NIP-PANI. MMA-MIP-PAPNI paper sensors also shows a positive correlation with increased MMA concentration. Wireless detection by a Pokitmeter also demonstrates the MIP paper sensors can be integrated in a mobile-based and wireless platform for multianalyte diagnostics. These non-enzymatic disposable paper sensors have the potential to reduce the health care cost of test strips as well as make test strips more accessible to underserved communities.

In the barcode hydrogel optical sensing platform, we proposed a multiplexed and implantable optical sensing platform based on oxidoreductase enzymes coupled with oxygen-sensitive metalloporphyrin phosphors immobilized within nanofilm-coated alginate microparticles embedded in discrete compartments of a single barcode hydrogel. Continuous multiplex oxygen and glucose monitoring were demonstrated through the measurement of phosphorescence lifetime changes of the metalloporphyrin phosphors. The phosphorescence lifetime showed a negative correlation with increases in the oxygen concentration and a positive correlation with increases in glucose concentration. The oxygen responsive assays showed a constant phosphorescence lifetime and the glucose responsive assays showed increased phosphorescence lifetime with the glucose concentration increased from 0 to 400 mg/dL, which demonstrates no crosstalk between the nearby oxygen and glucose responsive compartments. The sensors were also exposed to 10 consecutive cycles of 0 mg/dL glucose and 200 mg/dL glucose and demonstrated

high stability during glucose challenges. The presented barcode hydrogel platform has the potential to be broadly applied in multiplexed and implantable applications.

5.2. Future Work

For the size-selective microfluidic platform, future work may include optimizing the microfluidic device design for large volume sample isolation, studying EV isolation using patient samples (whole blood or human body fluids) and investigating integration with other downstream analysis platforms such as EV detection, PCR chips and mRNA analysis on a single platform. The molecular and cargo information of EVs could be studied based on specific size of subgroups and provide biological information for prognostic and diagnostics. Besides, the proteins or other bio-fragments collected in the bottom channel could be analyzed.

For the paper-based biosensors, future work may include optimizing the parameters for polyaniline synthesis with more template cavities/binding sites with increased surface areas. Other conductive monomers could be also studied as the material for co-polymerization, such as polypyrrole, polyacetylene, and polyindole. Furthermore, the paper strips could be integrated with filter papers on 3D paper-based microfluidic point-of-care testing platform for clinical applications. Human whole blood could be studied as the samples to analyze the accuracy of this proposed paper sensor for glucose detection. Besides, this paper sensing platform could be further studied for other biomarkers such as CRP and MMA in serum and patient samples.

For the barcode hydrogel optical sensing platform, future work may include optimizing the dimension of the 1x4 array barcode hydrogel sensor for miniaturized implantation. The dye concentration, enzyme concentration and catalyze concentration could be further optimized to achieve high sensitivity at high glucose concentrations. With the development of miniaturized barcode hydrogel sensor, future efforts will be focused on collaborating with UCLA and Rice University groups in developing wearable imaging platform towards animal test. Other sensing assays based on phosphorescence lifetime could be also immobilized in the compartments for multianalyte biosensing such as lactate, uric acid, and cholesterol. Fluorescence resonance energy transfer (FRET) based glucose sensing assays could be also embedded in this barcode hydrogel platform.

REFERENCES

1. Henning, A. K., Microfluidic MEMS. *Aerosp Conf Proc* **1998**, 471-486.

2. Nguyen, N. T.; Wereley, S.; Shaegh, S. A. M., Fundamentals and Applications of Microfluidics, Third Edition. *Artech Hse Integr Mi* **2019**, 1-548.

3. Azizipour, N.; Avazpour, R.; Rosenzweig, D. H.; Sawan, M.; Ajji, A., Evolution of Biochip Technology: A Review from Lab-on-a-Chip to Organ-on-a-Chip. *Micromachines-Basel* **2020,** *11* (6).

4. Culbertson, C. T.; Mickleburgh, T. G.; Stewart-James, S. A.; Sellens, K. A.; Pressnall, M., Micro Total Analysis Systems: Fundamental Advances and Biological Applications. *Anal Chem* **2014,** *86* (1), 95-118.

5. Haneveld, J.; Jansen, H.; Berenschot, E.; Tas, N.; Elwenspoek, M., Wet anisotropic etching for fluidic 1D nanochannels. *J Micromech Microeng* **2003,** *13* (4), S62-S66.

6. Scholten, K.; Meng, E., Electron-beam lithography for polymer bioMEMS with submicron features. *Microsyst Nanoeng* **2016,** *2*.

7. van Kan, J. A.; Bettiol, A. A.; Watt, F., Three-dimensional nanolithography using proton beam writing. *Appl Phys Lett* **2003,** *83* (8), 1629-1631.

8. Mappes, T.; Achenbach, S.; Mohr, J., Process conditions in X-ray lithography for the fabrication of devices with sub-micron feature sizes. *Microsyst Technol* **2007,** *13* (3-4), 355-360.

9. Wu, B. Q.; Kumar, A., Extreme ultraviolet lithography and three dimensional integrated circuit-A review. *Appl Phys Rev* **2014,** *1* (1).

10. Wua, B. Q.; Kumar, A., Extreme ultraviolet lithography: A review. *J Vac Sci Technol B* **2007,** *25* (6), 1743-1761.

11. Kovacs, G. T. A.; Maluf, N. I.; Petersen, K. E., Bulk micromachining of silicon. *P Ieee* **1998,** *86* (8), 1536-1551.

12. Tormen, M.; Carpentiero, A.; Vaccari, L.; Altissimo, M.; Ferrari, E.; Cojoc, D.; Di Fabrizio, E., Fabrication of three-dimensional stamps for embossing techniques by lithographically controlled isotropic wet etching. *J Vac Sci Technol B* **2005,** *23* (6), 2920-2924.

13. Donnelly, V. M.; Kornblit, A., Plasma etching: Yesterday, today, and tomorrow. *J Vac Sci Technol A* **2013,** *31* (5).

14. Mijatovic, D.; Eijkel, J. C. T.; van den Berg, A., Technologies for nanofluidic systems: top-down vs. bottom-up - a review. *Lab on a Chip* **2005,** *5* (5), 492-500.

15. Budhe, S.; Banea, M. D.; de Barros, S.; da Silva, L. F. M., An updated review of adhesively bonded joints in composite materials. *Int J Adhes Adhes* **2017,** *72*, 30-42.

16. Knowles, K. M.; van Helvoort, A. T. J., Anodic bonding. *Int Mater Rev* **2006,** *51* (5), 273-311.

17. Ko, C. T.; Chen, K. N., Wafer-level bonding/stacking technology for 3D integration. *Microelectronics Reliability* **2010,** *50* (4), 481-488.

18. Ageorges, C.; Ye, L.; Hou, M., Advances in fusion bonding techniques for joining thermoplastic matrix composites: a review. *Compos Part a-Appl S* **2001,** *32* (6), 839-857.

19. Tsao, C. W., Polymer Microfluidics: Simple, Low-Cost Fabrication Process Bridging Academic Lab Research to Commercialized Production. *Micromachines-Basel* **2016,** *7* (12).

20. McDonald, J. C.; Whitesides, G. M., Poly(dimethylsiloxane) as a material for fabricating microfluidic devices. *Accounts Chem Res* **2002,** *35* (7), 491-499.

21. Matellan, C.; Hernandez, A. E. D., Cost-effective rapid prototyping and assembly of poly(methyl methacrylate) microfluidic devices. *Sci Rep-Uk* **2018,** *8*.

22. Pentecost, A. M.; Martin, R. S., Fabrication and characterization of all-polystyrene microfluidic devices with integrated electrodes and tubing. *Anal Methods-Uk* **2015,** *7* (7), 2968-2976.

23. Ogonczyk, D.; Jankowski, P.; Garstecki, P., A Method for Simultaneous Polishing and Hydrophobization of Polycarbonate for Microfluidic Applications. *Polymers-Basel* **2020,** *12* (11).

24. Zhang, X. J.; Zhu, Z. X.; Ni, Z. H.; Xiang, N.; Yi, H., Inexpensive, rapid fabrication of polymer-film microfluidic autoregulatory valve for disposable microfluidics. *Biomedical Microdevices* **2017,** *19* (2).

25. Lin, D.; Li, B. W.; Qi, J.; Ji, X. F.; Yang, S. X.; Wang, W. H.; Chen, L. X., Low cost fabrication of microfluidic paper-based analytical devices with water-based

polyurethane acrylate and their application for bacterial detection. *Sensor Actuat B-Chem* **2020,** *303*.

26. Yarin, A. L., Novel nanofluidic and microfluidic devices and their applications. *Curr Opin Chem Eng* **2020,** *29*, 17-25.

27. Songjaroen, T.; Dungchai, W.; Chailapakul, O.; Laiwattanapaisal, W., Novel, simple and low-cost alternative method for fabrication of paper-based microfluidics by wax dipping. *Talanta* **2011,** *85* (5), 2587-2593.

28. Reboud, J.; Xu, G. L.; Garrett, A.; Adriko, M.; Yang, Z. G.; Tukahebwa, E. M.; Rowell, C.; Cooper, J. M., Paper-based microfluidics for DNA diagnostics of malaria in low resource underserved rural communities. *P Natl Acad Sci USA* **2019,** *116* (11), 4834-4842.

29. Wichterle, O.; Lim, D., Hydrophilic Gels for Biological Use. *Nature* **1960,** *185* (4706), 117-118.

30. Zhang, X.; Li, L.; Luo, C., Gel integration for microfluidic applications. *Lab Chip* **2016,** *16* (10), 1757-76.

31. Haraguchi, K.; Takada, T.; Haraguchi, R., Nanocomposite Gels by Initiator-Free Photopolymerization: Role of Plasma-Treated Clay in the Synthesis and Network Formation. *Acs Appl Nano Mater* **2018,** *1* (1), 418-425.

32. Kam, D.; Braner, A.; Abouzglo, A.; Larush, L.; Chiappone, A.; Shoseyov, O.; Magdassi, S., 3D Printing of Cellulose Nanocrystal-Loaded Hydrogels through Rapid Fixation by Photopolymerization. *Langmuir* **2021,** *37* (21), 6451-6458.

33. Dendukuri, D.; Gu, S. S.; Pregibon, D. C.; Hatton, T. A.; Doyle, P. S., Stop-flow lithography in a microfluidic device. *Lab on a Chip* **2007,** *7* (7), 818-828.

34. Jang, J. H.; Dendukuri, D.; Hatton, T. A.; Thomas, E. L.; Doyle, P. S., A route to three-dimensional structures in a microfluidic device: Stop-flow interference lithography. *Angew Chem Int Edit* **2007,** *46* (47), 9027-9031.

35. Properzi, F.; Logozzi, M.; Fais, S., Exosomes: the future of biomarkers in medicine. *Biomark Med* **2013,** *7* (5), 769-778.

36. EL Andaloussi, S.; Maeger, I.; Breakefield, X. O.; Wood, M. J. A., Extracellular vesicles: biology and emerging therapeutic opportunities. *Nat Rev Drug Discov* **2013,** *12* (5), 348-358.

37. Thery, C.; Zitvogel, L.; Amigorena, S., Exosomes: Composition, biogenesis and function. *Nat Rev Immunol* **2002,** *2* (8), 569-579.

38. Caponnetto, F.; Manini, I.; Skrap, M.; Palmai-Pallag, T.; Di Loreto, C.; Beltrami, A. P.; Cesselli, D.; Ferrari, E., Size-dependent cellular uptake of exosomes. *Nanomedicine* **2017,** *13* (3), 1011-1020.

39. Paulaitis, M.; Agarwal, K.; Nana-Sinkam, P., Dynamic Scaling of Exosome Sizes. *Langmuir* **2018,** *34* (32), 9387-9393.

40. Yanez-Mo, M.; Siljander, P. R. M.; Andreu, Z.; Zavec, A. B.; Borras, F. E.; Buzas, E. I.; Buzas, K.; Casal, E.; Cappello, F.; Carvalho, J.; Colas, E.; Cordeiro-da Silva, A.; Fais, S.; Falcon-Perez, J. M.; Ghobrial, I. M.; Giebel, B.; Gimona, M.; Graner, M.; Gursel, I.; Gursel, M.; Heegaard, N. H. H.; Hendrix, A.; Kierulf, P.; Kokubun, K.; Kosanovic, M.; Kralj-Iglic, V.; Kramer-Albers, E. M.; Laitinen, S.;

Lasser, C.; Lener, T.; Ligeti, E.; Line, A.; Lipps, G.; Llorente, A.; Lotvall, J.; Mancek-Keber, M.; Marcilla, A.; Mittelbrunn, M.; Nazarenko, I.; Nolte-t' Hoen, E. N. M.; Nyman, T. A.; O'Driscoll, L.; Olivan, M.; Oliveira, C.; Pallinger, E.; del Portillo, H. A.; Reventos, J.; Rigau, M.; Rohde, E.; Sammar, M.; Sanchez-Madrid, F.; Santarem, N.; Schallmoser, K.; Ostenfeld, M. S.; Stoorvogel, W.; Stukelj, R.; Van der Grein, S. G.; Vasconcelos, M. H.; Wauben, M. H. M.; De Wever, O., Biological properties of extracellular vesicles and their physiological functions. *J Extracell Vesicles* **2015,** *4*.

41. Di Vizio, D.; Kim, J.; Hager, M. H.; Morello, M.; Yang, W.; Lafargue, C. J.; True, L. D.; Rubin, M. A.; Adam, R. M.; Beroukhim, R.; Demichelis, F.; Freeman, M. R., Oncosome Formation in Prostate Cancer: Association with a Region of Frequent Chromosomal Deletion in Metastatic Disease. *Cancer Res* **2009,** *69* (13), 5601-5609.

42. Zhang, H. Y.; Freitas, D.; Kim, H. S.; Fabijanic, K.; Li, Z.; Chen, H. Y.; Mark, M. T.; Molina, H.; Martin, A. B.; Bojmar, L.; Fang, J.; Rampersaud, S.; Hoshino, A.; Matei, I.; Kenific, C. M.; Nakajima, M.; Mutvei, A. P.; Sansone, P.; Buehring, W.; Wang, H. J.; Jimenez, J. P.; Cohen-Gould, L.; Paknejad, N.; Brendel, M.; Manova-Todorova, K.; Magalhaes, A.; Ferreira, J. A.; Osorio, H.; Silva, A. M.; Massey, A.; Cubillos-Ruiz, J. R.; Galletti, G.; Giannakakou, P.; Cuervo, A. M.; Blenis, J.; Schwartz, R.; Brady, M. S.; Peinado, H.; Bromberg, J.; Matsui, H.; Reis, C. A.; Lyden, D., Identification of distinct nanoparticles and subsets of extracellular vesicles by asymmetric flow field-flow fractionation. *Nat Cell Biol* **2018,** *20* (3), 332-343.

43. Choi, D.; Spinelli, C.; Montermini, L.; Rak, J., Oncogenic Regulation of Extracellular Vesicle Proteome and Heterogeneity. *Proteomics* **2019,** *19* (1-2).

44. Kaplan, R. N.; Riba, R. D.; Zacharoulis, S.; Bramley, A. H.; Vincent, L.; Costa, C.; MacDonald, D. D.; Jin, D. K.; Shido, K.; Kerns, S. A.; Zhu, Z. P.; Hicklin, D.; Wu, Y.; Port, J. L.; Altorki, N.; Port, E. R.; Ruggero, D.; Shmelkov, S. V.; Jensen, K. K.; Rafii, S.; Lyden, D., VEGFR1-positive haematopoietic bone marrow progenitors initiate the pre-metastatic niche. *Nature* **2005,** *438* (7069), 820-827.

45. Peinado, H.; Aleckovic, M.; Lavotshkin, S.; Matei, I.; Costa-Silva, B.; Moreno-Bueno, G.; Hergueta-Redondo, M.; Williams, C.; Garcia-Santos, G.; Ghajar, C. M.; Nitadori-Hoshino, A.; Hoffman, C.; Badal, K.; Garcia, B. A.; Callahan, M. K.; Yuan, J. D.; Martins, V. R.; Skog, J.; Kaplan, R. N.; Brady, M. S.; Wolchok, J. D.; Chapman, P. B.; Kang, Y. B.; Bromberg, J.; Lyden, D., Melanoma exosomes educate bone marrow progenitor cells toward a pro-metastatic phenotype through MET. *Nat Med* **2012,** *18* (6), 883-891.

46. Thery, C.; Amigorena, S.; Raposo, G.; Clayton, A., Isolation and characterization of exosomes from cell culture supernatants and biological fluids. *Curr Protoc Cell Biol* **2006,** *Chapter 3*, Unit 3 22.

47. Momen-Heravi, F.; Balaj, L.; Alian, S.; Mantel, P. Y.; Halleck, A. E.; Trachtenberg, A. J.; Soria, C. E.; Oquin, S.; Bonebreak, C. M.; Saracoglu, E.; Skog, J.; Kuo, W. P., Current methods for the isolation of extracellular vesicles. *Biol Chem* **2013,** *394* (10), 1253-1262.

48. Andre, F.; Schartz, N. E.; Movassagh, M.; Flament, C.; Pautier, P.; Morice, P.; Pomel, C.; Lhomme, C.; Escudier, B.; Le Chevalier, T.; Tursz, T.; Amigorena, S.; Raposo, G.; Angevin, E.; Zitvogel, L., Malignant effusions and immunogenic tumour-derived exosomes. *Lancet* **2002,** *360* (9329), 295-305.

49. Gamez-Valero, A.; Monguio-Tortajada, M.; Carreras-Planella, L.; Franquesa, M.; Beyer, K.; Borras, F. E., Size-Exclusion Chromatography-based isolation minimally alters Extracellular Vesicles' characteristics compared to precipitating agents. *Sci Rep* **2016,** *6*, 33641.

50. Shin, S.; Han, D.; Park, M. C.; Mun, J. Y.; Choi, J.; Chun, H.; Kim, S.; Hong, J. W., Separation of extracellular nanovesicles and apoptotic bodies from cancer cell culture broth using tunable microfluidic systems. *Sci Rep* **2017,** *7* (1), 9907.

51. Taylor, D. D.; Zacharias, W.; Gercel-Taylor, C., Exosome isolation for proteomic analyses and RNA profiling. *Methods Mol Biol* **2011,** *728*, 235-46.

52. Woo, H. K.; Sunkara, V.; Park, J.; Kim, T. H.; Han, J. R.; Kim, C. J.; Choi, H. I.; Kim, Y. K.; Cho, Y. K., Exodisc for Rapid, Size-Selective, and Efficient Isolation and Analysis of Nanoscale Extracellular Vesicles from Biological Samples. *ACS Nano* **2017,** *11* (2), 1360-1370.

53. Liang, L. G.; Kong, M. Q.; Zhou, S.; Sheng, Y. F.; Wang, P.; Yu, T.; Inci, F.; Kuo, W. P.; Li, L. J.; Demirci, U.; Wang, S., An integrated double-filtration microfluidic device for isolation, enrichment and quantification of urinary extracellular vesicles for detection of bladder cancer. *Sci Rep* **2017,** *7*, 46224.

54. Davies, R. T.; Kim, J.; Jang, S. C.; Choi, E. J.; Gho, Y. S.; Park, J., Microfluidic filtration system to isolate extracellular vesicles from blood. *Lab on a Chip* **2012,** *12* (24), 5202-5210.

55. He, M.; Crow, J.; Roth, M.; Zeng, Y.; Godwin, A. K., Integrated immunoisolation and protein analysis of circulating exosomes using microfluidic technology. *Lab Chip* **2014,** *14* (19), 3773-80.

56. Van Deun, J.; Mestdagh, P.; Sormunen, R.; Cocquyt, V.; Vermaelen, K.; Vandesompele, J.; Bracke, M.; De Wever, O.; Hendrix, A., The impact of disparate isolation methods for extracellular vesicles on downstream RNA profiling. *J Extracell Vesicles* **2014,** *3* (1).

57. Taylor, D. D.; Shah, S., Methods of isolating extracellular vesicles impact down-stream analyses of their cargoes. *Methods* **2015,** *87*, 3-10.

58. Momen-Heravi, F.; Balaj, L.; Alian, S.; Mantel, P. Y.; Halleck, A. E.; Trachtenberg, A. J.; Soria, C. E.; Oquin, S.; Bonebreak, C. M.; Saracoglu, E.; Skog, J.; Kuo, W. P., Current methods for the isolation of extracellular vesicles. *Biol Chem* **2013,** *394* (10), 1253-62.

59. Liu, F.; Vermesh, O.; Mani, V.; Ge, T. J.; Madsen, S. J.; Sabour, A.; Hsu, E. C.; Gowrishankar, G.; Kanada, M.; Jokerst, J. V.; Sierra, R. G.; Chang, E.; Lau, K.; Sridhar, K.; Bermudez, A.; Pitteri, S. J.; Stoyanova, T.; Sinclair, R.; Nair, V. S.; Gambhir, S. S.; Demirci, U., The Exosome Total Isolation Chip. *ACS Nano* **2017,** *11* (11), 10712-10723.

60. Yasui, T.; Yanagida, T.; Ito, S.; Konakade, Y.; Takeshita, D.; Naganawa, T.; Nagashima, K.; Shimada, T.; Kaji, N.; Nakamura, Y.; Thiodorus, I. A.; He, Y.; Rahong, S.; Kanai, M.; Yukawa, H.; Ochiya, T.; Kawai, T.; Baba, Y., Unveiling massive numbers of cancer-related urinary-microRNA candidates via nanowires. *Sci Adv* **2017,** *3* (12), e1701133.

61. Wang, Z.; Wu, H. J.; Fine, D.; Schmulen, J.; Hu, Y.; Godin, B.; Zhang, J. X.; Liu, X., Ciliated micropillars for the microfluidic-based isolation of nanoscale lipid vesicles. *Lab Chip* **2013,** *13* (15), 2879-82.

62. Lee, K.; Shao, H.; Weissleder, R.; Lee, H., Acoustic purification of extracellular microvesicles. *ACS Nano* **2015,** *9* (3), 2321-7.

63. Wu, M.; Ouyang, Y.; Wang, Z.; Zhang, R.; Huang, P. H.; Chen, C.; Li, H.; Li, P.; Quinn, D.; Dao, M.; Suresh, S.; Sadovsky, Y.; Huang, T. J., Isolation of exosomes from whole blood by integrating acoustics and microfluidics. *Proc Natl Acad Sci U S A* **2017,** *114* (40), 10584-10589.

64. Wunsch, B. H.; Smith, J. T.; Gifford, S. M.; Wang, C.; Brink, M.; Bruce, R. L.; Austin, R. H.; Stolovitzky, G.; Astier, Y., Nanoscale lateral displacement arrays for the separation of exosomes and colloids down to 20 nm. *Nat Nanotechnol* **2016,** *11* (11), 936-940.

65. Santana, S. M.; Antonyak, M. A.; Cerione, R. A.; Kirby, B. J., Microfluidic isolation of cancer-cell-derived microvesicles from hetergeneous extracellular shed vesicle populations. *Biomed Microdevices* **2014,** *16* (6), 869-77.

66. Liu, C.; Guo, J.; Tian, F.; Yang, N.; Yan, F.; Ding, Y.; Wei, J.; Hu, G.; Nie, G.; Sun, J., Field-Free Isolation of Exosomes from Extracellular Vesicles by Microfluidic Viscoelastic Flows. *ACS Nano* **2017,** *11* (7), 6968-6976.

67. Cho, S.; Jo, W.; Heo, Y.; Kang, J. Y.; Kwak, R.; Park, J., Isolation of extracellular vesicle from blood plasma using electrophoretic migration through porous membrane. *Sensor Actuat B-Chem* **2016,** *233*, 289-297.

68. Ibsen, S. D.; Wright, J.; Lewis, J. M.; Kim, S.; Ko, S. Y.; Ong, J.; Manouchehri, S.; Vyas, A.; Akers, J.; Chen, C. C.; Carter, B. S.; Esener, S. C.; Heller, M. J., Rapid Isolation and Detection of Exosomes and Associated Biomarkers from Plasma. *Acs Nano* **2017,** *11* (7), 6641-6651.

69. Chen, Z. Y.; Yang, Y.; Yamaguchi, H.; Hung, M. C.; Kameoka, J., Isolation of cancer-derived extracellular vesicle subpopulations by a size-selective microfluidic platform. *Biomicrofluidics* **2020,** *14* (3).

70. Harvey, D. Mordern Analytical chemistry. McGraw-Hill: New York, 2010; pp 598-600.

71. Israelachvili, J. Intermolecular & Surface Forces. Academic Press: Cambridge, 2011; pp 291-316.

72. Salgin, S.; Salgin, U.; Bahadir, S., Zeta Potentials and Isoelectric Points of Biomolecules: The Effects of Ion Types and Ionic Strengths. *Int J Electrochem Sc* **2012,** *7* (12), 12404-12414.

73. Wu, M. X.; Ouyang, Y. S.; Wang, Z. Y.; Zhang, R.; Huang, P. H.; Chen, C. Y.; Li, H.; Li, P.; Quinn, D.; Dao, M.; Suresh, S.; Sadovsky, Y.; Huang, T. J.,

Isolation of exosomes from whole blood by integrating acoustics and microfluidics. *P Natl Acad Sci USA* **2017,** *114* (40), 10584-10589.

74. Beit-Yannai, E.; Tabak, S.; Stamer, W. D., Physical exosome:exosome interactions. *J Cell Mol Med* **2018,** *22* (3), 2001-2006.

75. Z. Chen, H. Yamaguchi and J. Kameoka, "Development of size-selective microfluidic platform," 2019 41st Annual International Conference of the IEEE Engineering in Medicine and Biology Society (EMBC), Berlin, Germany, 2019, pp. 5661-5664.

76. Yang, Y.; Li, C. W.; Chan, L. C.; Wei, Y.; Hsu, J. M.; Xia, W.; Cha, J. H.; Hou, J.; Hsu, J. L.; Sun, L.; Hung, M. C., Exosomal PD-L1 harbors active defense function to suppress T cell killing of breast cancer cells and promote tumor growth. *Cell Res* **2018,** *28* (8), 862-864.

77. Chen, Z. Y.; Yamaguchi, H.; Kameoka, J., Development of size-selective microfluidic platform. *2019 41st Annual International Conference of the Ieee Engineering in Medicine and Biology Society (Embc)* **2019**, 5661-5664.

78. Doyle, L. M.; Wang, M. Z., Overview of Extracellular Vesicles, Their Origin, Composition, Purpose, and Methods for Exosome Isolation and Analysis. *Cells* **2019,** *8* (7).

79. Heinemann, M. L.; Ilmer, M.; Silva, L. P.; Hawke, D. H.; Recio, A.; Vorontsova, M. A.; Alt, E.; Vykoukal, J., Benchtop isolation and characterization of functional exosomes by sequential filtration. *J Chromatogr A* **2014,** *1371*, 125-35.

80. GlucoWatch approved for children with diabetes. *FDA Consum* **2002,** *36* (6), 6.

81. American Diabetes, A., Diagnosis and classification of diabetes mellitus. *Diabetes Care* **2004,** *27 Suppl 1*, S5-S10.

82. Coster, S.; Gulliford, M. C.; Seed, P. T.; Powrie, J. K.; Swaminathan, R., Monitoring blood glucose control in diabetes mellitus: a systematic review. *Health Technol Assess* **2000,** *4* (12), 1-93.

83. Bruen, D.; Delaney, C.; Florea, L.; Diamond, D., Glucose Sensing for Diabetes Monitoring: Recent Developments. *Sensors-Basel* **2017,** *17* (8).

84. Yoo, E. H.; Lee, S. Y., Glucose Biosensors: An Overview of Use in Clinical Practice. *Sensors-Basel* **2010,** *10* (5), 4558-4576.

85. Toghill, K. E.; Compton, R. G., Electrochemical Non-enzymatic Glucose Sensors: A Perspective and an Evaluation. *Int J Electrochem Sc* **2010,** *5* (9), 1246-1301.

86. Burmeister, J. J.; Arnold, M. A.; Small, G. W., Noninvasive blood glucose measurements by near-infrared transmission spectroscopy across human tongues. *Diabetes Technol Ther* **2000,** *2* (1), 5-16.

87. Saiga, N.; Hamada, C.; Ikeda, J., Near infrared spectroscopy assessment of the glucose solution processed by ultrasonic cavitation. *Ultrasonics* **2006,** *44 Suppl 1*, e101-4.

88. Clark, L. C., Jr.; Lyons, C., Electrode systems for continuous monitoring in cardiovascular surgery. *Ann N Y Acad Sci* **1962,** *102*, 29-45.

89. Heller, A.; Feldman, B., Electrochemistry in Diabetes Management. *Accounts Chem Res* **2010,** *43* (7), 963-973.

90. Bao, S. J.; Li, C. M.; Zang, J. F.; Cui, X. Q.; Qiao, Y.; Guo, J., New nanostructured TiO2 for direct electrochemistry and glucose sensor applications. *Adv Funct Mater* **2008,** *18* (4), 591-599.

91. Jing, W.; Yang, Q., Mediator-free amperometric determination of glucose based on direct electron transfer between glucose oxidase and an oxidized boron-doped diamond electrode. *Anal Bioanal Chem* **2006,** *385* (7), 1330-1335.

92. Oliver, N. S.; Toumazou, C.; Cass, A. E. G.; Johnston, D. G., Glucose sensors: a review of current and emerging technology. *Diabetic Med* **2009,** *26* (3), 197-210.

93. Hwang, D. W.; Lee, S.; Seo, M.; Chung, T. D., Recent advances in electrochemical non-enzymatic glucose sensors - A review. *Anal Chim Acta* **2018,** *1033*, 1-34.

94. Lee, W. C.; Kim, K. B.; Gurudatt, N. G.; Hussain, K. K.; Choi, C. S.; Park, D. S.; Shim, Y. B., Comparison of enzymatic and non-enzymatic glucose sensors based on hierarchical Au-Ni alloy with conductive polymer. *Biosens Bioelectron* **2019,** *130*, 48-54.

95. Amin, B. G.; Masud, J.; Nath, M., A non-enzymatic glucose sensor based on a CoNi2Se4/rGO nanocomposite with ultrahigh sensitivity at low working potential. *J Mater Chem B* **2019,** *7* (14), 2338-2348.

96. Erturk, G.; Mattiasson, B., Molecular Imprinting Techniques Used for the Preparation of Biosensors. *Sensors-Basel* **2017,** *17* (2).

97. Asliyuce, S.; Uzun, L.; Rad, A. Y.; Unal, S.; Say, R.; Denizli, A., Molecular imprinting based composite cryogel membranes for purification of anti-hepatitis B

surface antibody by fast protein liquid chromatography. *J Chromatogr B Analyt Technol Biomed Life Sci* **2012,** *889-890*, 95-102.

98. Ma, C. M.; Sun, Z.; Chen, C. B.; Zhang, L. L.; Zhu, S. H., Simultaneous separation and determination of fructose, sorbitol, glucose and sucrose in fruits by HPLC-ELSD. *Food Chem* **2014,** *145*, 784-788.

99. Kempe, M.; Mosbach, K., Molecular Imprinting Used for Chiral Separations. *Journal of Chromatography A* **1995,** *694* (1), 3-13.

100. Manzoor, S.; Buffon, R.; Rossi, A. V., Molecularly imprinted solid phase extraction of fluconazole from pharmaceutical formulations. *Talanta* **2015,** *134*, 1-7.

101. da Silva, H.; Pacheco, J. G.; Magalhaes, J. M. C. S.; Viswanathan, S.; Delerue-Matos, C., MIP-graphene-modified glassy carbon electrode for the determination of trimethoprim. *Biosens Bioelectron* **2014,** *52*, 56-61.

102. Deng, H.; Lin, L.; Ji, M. Z.; Zhang, S. M.; Yang, M. B.; Fu, Q., Progress on the morphological control of conductive network in conductive polymer composites and the use as electroactive multifunctional materials. *Prog Polym Sci* **2014,** *39* (4), 627-655.

103. Farid, M. M.; Goudini, L.; Piri, F.; Zamani, A.; Saadati, F., Molecular imprinting method for fabricating novel glucose sensor: Polyvinyl acetate electrode reinforced by MnO2/CuO loaded on graphene oxide nanoparticles. *Food Chem* **2016,** *194*, 61-67.

104. Yoshimi, Y.; Narimatsu, A.; Nakayama, K.; Sekine, S.; Hattori, K.; Sakai, K., Development of an enzyme-free glucose sensor using the gate effect of a molecularly imprinted polymer. *J Artif Organs* **2009,** *12* (4), 264-70.

105. Sharma, P. S.; Pietrzyk-Le, A.; D'Souza, F.; Kutner, W., Electrochemically synthesized polymers in molecular imprinting for chemical sensing. *Anal Bioanal Chem* **2012,** *402* (10), 3177-3204.

106. Luo, J.; Huang, J.; Wu, Y. N.; Sun, J.; Wei, W.; Liu, X. Y., Synthesis of hydrophilic and conductive molecularly imprinted polyaniline particles for the sensitive and selective protein detection. *Biosens Bioelectron* **2017,** *94*, 39-46.

107. Bessaire, B.; Mathieu, M.; Salles, V.; Yeghoyan, T.; Celle, C.; Simonato, J. P.; Brioude, A., Synthesis of Continuous Conductive PEDOT:PSS Nanofibers by Electrospinning: A Conformal Coating for Optoelectronics. *ACS Appl Mater Interfaces* **2017,** *9* (1), 950-957.

108. Boehler, C.; Oberueber, F.; Schlabach, S.; Stieglitz, T.; Asplund, M., Long-Term Stable Adhesion for Conducting Polymers in Biomedical Applications: IrOx and Nanostructured Platinum Solve the Chronic Challenge. *ACS Appl Mater Interfaces* **2017,** *9* (1), 189-197.

109. Bhagwat, N.; Murray, R. E.; Shah, S. I.; Kiick, K. L.; Martin, D. C., Biofunctionalization of PEDOT films with laminin-derived peptides. *Acta Biomater* **2016,** *41*, 235-46.

110. Martinez, A. W.; Phillips, S. T.; Butte, M. J.; Whitesides, G. M., Patterned paper as a platform for inexpensive, low-volume, portable bioassays. *Angewandte Chemie* **2007,** *119* (8), 1340-1342.

111. Cao, Q.; Liang, B.; Tu, T.; Wei, J.; Fang, L.; Ye, X., Three-dimensional paper-based microfluidic electrochemical integrated devices (3D-PMED) for wearable electrochemical glucose detection. *RSC advances* **2019,** *9* (10), 5674-5681.

112. Qi, X.; Li, X.; Jo, H.; Bhat, K. S.; Kim, S.; An, J.; Kang, J.-W.; Lim, S., Mulberry paper-based graphene strain sensor for wearable electronics with high mechanical strength. *Sensors and Actuators A: Physical* **2020,** *301*, 111697.

113. Liu, C.; Xu, T.; Wang, D.; Zhang, X., The role of sampling in wearable sweat sensors. *Talanta* **2020,** *212*, 120801.

114. Mao, K.; Min, X.; Zhang, H.; Zhang, K.; Cao, H.; Guo, Y.; Yang, Z., based microfluidics for rapid diagnostics and drug delivery. *Journal of Controlled Release* **2020**.

115. Zhang, H.; Chen, Z. Y.; Dai, J.; Zhang, W.; Jiang, Y. Q.; Zhou, A. H., A low-cost mobile platform for whole blood glucose monitoring using colorimetric method. *Microchem J* **2021,** *162*.

116. Liu, H.; Xiang, Y.; Lu, Y.; Crooks, R. M., Aptamer-based origami paper analytical device for electrochemical detection of adenosine. *Angewandte Chemie* **2012,** *124* (28), 7031-7034.

117. Ding, J.; Li, B.; Chen, L.; Qin, W., A Three-Dimensional Origami Paper-Based Device for Potentiometric Biosensing. *Angewandte Chemie International Edition* **2016,** *55* (42), 13033-13037.

118. Liang, B.; Zhu, Q.; Fang, L.; Cao, Q.; Liang, X.; Ye, X., An origami paper device for complete elimination of interferents in enzymatic electrochemical biosensors. *Electrochemistry Communications* **2017,** *82*, 43-46.

119. Chen, Z. Y.; Wright, C.; Dincel, O.; Chi, T. Y.; Kameoka, J., A Low-Cost Paper Glucose Sensor with Molecularly Imprinted Polyaniline Electrode. *Sensors-Basel* **2020,** *20* (4).

120. Chen, Z. Y.; Chi, T. Y.; Dincel, O.; Tong, L.; Kameoka, J., A Low-cost and Enzyme-free Glucose Paper Sensor. *42nd Annual International Conferences of the Ieee Engineering in Medicine and Biology Society: Enabling Innovative Technologies for Global Healthcare Embc'20* **2020**, 4097-4100.

121. Borysiak, M. D.; Thompson, M. J.; Posner, J. D., Translating diagnostic assays from the laboratory to the clinic: analytical and clinical metrics for device development and evaluation. *Lab Chip* **2016,** *16* (8), 1293-313.

122. Tillett, W. S.; Francis, T., Serological Reactions in Pneumonia with a Non-Protein Somatic Fraction of Pneumococcus. *J Exp Med* **1930,** *52* (4), 561-71.

123. Zen, Q.; Zhong, W. J.; Mortensen, R. F., Binding site on human C-reactive protein (CRP) recognized by the leukocyte CRP-receptor. *J Cell Biochem* **1997,** *64* (1), 140-151.

124. Schulz, R.; Heusch, G., C-Reactive Protein Just a Biomarker of Inflammation or a Pathophysiological Player in Myocardial Function and Morphology? *Hypertension* **2011,** *57* (2), 151-153.

125. Anand, I. S.; Latini, R.; Florea, V. G.; Kuskowski, M. A.; Rector, T.; Masson, S.; Signorini, S.; Mocarelli, P.; Hester, A.; Glazer, R.; Cohn, J. N.; Investigators, V.-H., C-reactive protein in heart failure - Prognostic value and the effect of valsartan. *Circulation* **2005,** *112* (10), 1428-1434.

126. Pepys, M. B.; Hirschfield, G. M., C-reactive protein: a critical update. *J Clin Invest* **2003,** *111* (12), 1805-1812.

127. Danesh, J.; Wheeler, J. G.; Hirschfield, G. M.; Eda, S.; Eiriksdottir, G.; Rumley, A.; Lowe, G. D. O.; Pepys, M. B.; Gudnason, V., C-reactive protein and other circulating markers of inflammation in the prediction of coronary heart disease. *New Engl J Med* **2004,** *350* (14), 1387-1397.

128. Lau, D. C. W.; Dhillon, B.; Yan, H. Y.; Szmitko, P. E.; Verma, S., Adipokines: molecular links between obesity and atheroslcerosis. *Am J Physiol-Heart C* **2005,** *288* (5), H2031-H2041.

129. Pearson, T. A.; Mensah, G. A.; Alexander, R. W.; Anderson, J. L.; Cannon, R. O., 3rd; Criqui, M.; Fadl, Y. Y.; Fortmann, S. P.; Hong, Y.; Myers, G. L.; Rifai, N.; Smith, S. C., Jr.; Taubert, K.; Tracy, R. P.; Vinicor, F.; Centers for Disease, C.; Prevention; American Heart, A., Markers of inflammation and cardiovascular disease: application to clinical and public health practice: A statement for healthcare professionals from the Centers for Disease Control and Prevention and the American Heart Association. *Circulation* **2003,** *107* (3), 499-511.

130. Smith, S. C., Jr.; Amsterdam, E.; Balady, G. J.; Bonow, R. O.; Fletcher, G. F.; Froelicher, V.; Heath, G.; Limacher, M. C.; Maddahi, J.; Pryor, D.; Redberg, R. F.;

Roccella, E.; Ryan, T.; Smaha, L.; Wenger, N. K., Prevention Conference V: Beyond secondary prevention: identifying the high-risk patient for primary prevention: tests for silent and inducible ischemia: Writing Group II. *Circulation* **2000,** *101* (1), E12-6.

131. Ouyang, M. X.; Tu, D. D.; Tong, L.; Sarwar, M.; Bhimaraj, A.; Li, C. Z.; Cote, G. L.; Di Carlo, D., A review of biosensor technologies for blood biomarkers toward monitoring cardiovascular diseases at the point-of-care. *Biosens Bioelectron* **2021,** *171*.

132. Chou, P. C.; Rick, J.; Chou, T. C., C-reactive protein thin-film molecularly imprinted polymers formed using a micro-contact approach. *Anal Chim Acta* **2005,** *542* (1), 20-25.

133. Liu, X.; Lin, W. F.; Xiao, P.; Yang, M. J.; Sun, L. P.; Zhang, Y.; Xue, W.; Guan, B. O., Polydopamine-based molecular imprinted optic microfiber sensor enhanced by template-mediated molecular rearrangement for ultra-sensitive C-reactive protein detection. *Chem Eng J* **2020,** *387*.

134. Gopalan, A. I.; Komathi, S.; Muthuchamy, N.; Lee, K. P.; Whitcombe, M. J.; Dhana, L.; Sai-Anand, G., Functionalized conjugated polymers for sensing and molecular imprinting applications. *Prog Polym Sci* **2019,** *88*, 1-129.

135. Haupt, K.; Mosbach, K., Molecularly imprinted polymers and their use in biomimetic sensors. *Chem Rev* **2000,** *100* (7), 2495-2504.

136. Fakanya, W. M.; Tothill, I. E., Detection of the Inflammation Biomarker C-Reactive Protein in Serum Samples: Towards an Optimal Biosensor Formula. *Biosensors-Basel* **2014,** *4* (4), 340-357.

137. Regan, B.; Boyle, F.; O'Kennedy, R.; Collins, D., Evaluation of Molecularly Imprinted Polymers for Point-of-Care Testing for Cardiovascular Disease. *Sensors-Basel* **2019,** *19* (16).

138. Chi, T. Y.; Chen, Z. Y.; Kameoka, J., Perfluorooctanesulfonic Acid Detection Using Molecularly Imprinted Polyaniline on a Paper Substrate. *Sensors-Basel* **2020,** *20* (24).

139. Chen, Z.; Chi, T. Y.; Dincel, O.; Tong, L.; Kameoka, J., A Low-cost and Enzyme-free Glucose Paper Sensor. *Annu Int Conf IEEE Eng Med Biol Soc* **2020,** *2020,* 4097-4100.

140. Majumdar, S.; Saikia, U.; Mahanta, D., Polyaniline-Coated Filter Papers: Cost Effective Hybrid Materials for Adsorption of Dyes. *J Chem Eng Data* **2015,** *60* (11), 3382-3391.

141. Tecleab, A. G.; Schofield, R. C.; Ramanathan, L. V.; Carlow, D. C., A Simple and Sensitive Method for Quantitative Measurement of Methylmalonic Acid by Turbulent Flow Chromatography and Tandem Mass Spectrometry. *J Chromatogr Sep Tech* **2016,** *7* (5).

142. Schroder, T. H.; Quay, T. A.; Lamers, Y., Methylmalonic acid quantified in dried blood spots provides a precise, valid, and stable measure of functional vitamin B-12 status in healthy women. *J Nutr* **2014,** *144* (10), 1658-63.

143. Obeid, R.; Geisel, J.; Herrmann, W., Comparison of two methods for measuring methylmalonic acid as a marker for vitamin B12 deficiency. *Diagnosis* **2015,** *2* (1), 67-72.

144. Gomes, A. P.; Ilter, D.; Low, V.; Endress, J. E.; Fernandez-Garcia, J.; Rosenzweig, A.; Schild, T.; Broekaert, D.; Ahmed, A.; Planque, M.; Elia, I.; Han, J.; Kinzig, C.; Mullarky, E.; Mutvei, A. P.; Asara, J.; de Cabo, R.; Cantley, L. C.; Dephoure, N.; Fendt, S. M.; Blenis, J., Age-induced accumulation of methylmalonic acid promotes tumour progression. *Nature* **2020,** *585* (7824), 283-+.

145. Akshaya, K. B.; Anitha, V.; Nidhin, M.; Sudhakar, Y. N.; Louis, G., Electrochemical sensing of vitamin B12 deficiency marker methylmalonic acid using PdAu-PPy tailored carbon fiber paper electrode. *Talanta* **2020,** *217*, 121028.

146. Deepa, J. R.; Anirudhan, T. S.; Soman, G.; Sekhar, V. C., Electrochemical sensing of methylmalonic acid based on molecularly imprinted polymer modified with graphene oxide and gold nanoparticles. *Microchem J* **2020,** *159*.

147. Hamburg, M. A.; Collins, F. S., The path to personalized medicine. *N Engl J Med* **2010,** *363* (4), 301-4.

148. Field, M. J.; Grigsby, J., Telemedicine and remote patient monitoring. *JAMA* **2002,** *288* (4), 423-5.

149. Mascini, M.; Tombelli, S., Biosensors for biomarkers in medical diagnostics. *Biomarkers* **2008,** *13* (7), 637-57.

150. Adachi, T.; Kitazumi, Y.; Shirai, O.; Kano, K., Development Perspective of Bioelectrocatalysis-Based Biosensors. *Sensors (Basel)* **2020,** *20* (17).

151. Saberian-Borujeni, M.; Johari-Ahar, M.; Hamzeiy, H.; Barar, J.; Omidi, Y., Nanoscaled aptasensors for multi-analyte sensing. *Bioimpacts* **2014,** *4* (4), 205-15.

152. Sempionatto, J. R.; Montiel, V. R.; Vargas, E.; Teymourian, H.; Wang, J., Wearable and Mobile Sensors for Personalized Nutrition. *ACS Sens* **2021,** *6* (5), 1745-1760.

153. Hou, X. D.; Xu, H.; Zhen, T. Y.; Wu, W., Recent developments in three-dimensional graphene-based electrochemical sensors for food analysis. *Trends Food Sci Tech* **2020,** *105*, 76-92.

154. Arduini, F.; Cinti, S.; Scognamiglio, V.; Moscone, D.; Palleschi, G., How cutting-edge technologies impact the design of electrochemical (bio)sensors for environmental analysis. A review. *Anal Chim Acta* **2017,** *959*, 15-42.

155. Gonzalez-Martinez, M. A.; Puchades, R.; Maquieira, A., Optical immunosensors for environmental monitoring: how far have we come? *Anal Bioanal Chem* **2007,** *387* (1), 205-18.

156. Gupta, S.; Kaushal, A.; Kumar, A.; Kumar, D., Recent advances in biosensors for diagnosis of celiac disease: A review. *Biotechnol Bioeng* **2019,** *116* (2), 444-451.

157. Chang, C. C., Recent Advancements in Aptamer-Based Surface Plasmon Resonance Biosensing Strategies. *Biosensors (Basel)* **2021,** *11* (7).

158. Pakchin, P. S.; Nakhjavani, S. A.; Saber, R.; Ghanbari, H.; Omidi, Y., Recent advances in simultaneous electrochemical multi-analyte sensing platforms. *Trac-Trend Anal Chem* **2017,** *92*, 32-41.

159. Goode, J. A.; Rushworth, J. V.; Millner, P. A., Biosensor Regeneration: A Review of Common Techniques and Outcomes. *Langmuir* **2015,** *31* (23), 6267-76.

160. Monton, M. R. N.; Forsberg, E. M.; Brennan, J. D., Tailoring Sol–Gel-Derived Silica Materials for Optical Biosensing. *Chem Mater* **2012,** *24* (5), 796-811.

161. Ouyang, M.; Tu, D.; Tong, L.; Sarwar, M.; Bhimaraj, A.; Li, C.; Cote, G. L.; Di Carlo, D., A review of biosensor technologies for blood biomarkers toward monitoring cardiovascular diseases at the point-of-care. *Biosens Bioelectron* **2021,** *171*, 112621.

162. Moore, T. J.; Moody, A. S.; Payne, T. D.; Sarabia, G. M.; Daniel, A. R.; Sharma, B., In Vitro and In Vivo SERS Biosensing for Disease Diagnosis. *Biosensors (Basel)* **2018,** *8* (2).

163. Deniz, S.; Khosrow, S.; Mohammad Reza, T.-k.; Ahmad Yari, K.; Mohammad, H., Development of electrochemical biosensors for tumor marker determination towards cancer diagnosis: Recent progress. *TrAC Trends in Analytical Chemistry* **2019,** *118*, 73-88.

164. Sanvicens, N.; Pastells, C.; Pascual, N.; Marco, M. P., Nanoparticle-based biosensors for detection of pathogenic bacteria. *Trac-Trend Anal Chem* **2009,** *28* (11), 1243-1252.

165. Omowunmi, A. S.; Austin, O. A.; Ailing, Z., Status of biomolecular recognition using electrochemical techniques. *Biosensors and Bioelectronics* **2009,** *24* (9), 2749-2765.

166. Chen, Z.; Wright, C.; Dincel, O.; Chi, T. Y.; Kameoka, J., A Low-Cost Paper Glucose Sensor with Molecularly Imprinted Polyaniline Electrode. *Sensors (Basel)* **2020,** *20* (4).

167. Falohun, T.; McShane, M. J., An Optical Urate Biosensor Based on Urate Oxidase and Long-Lifetime Metalloporphyrins. *Sensors (Basel)* **2020,** *20* (4).

168. Yang, H., Enzyme-based ultrasensitive electrochemical biosensors. *Curr Opin Chem Biol* **2012,** *16* (3-4), 422-8.

169. Dai, J.; Zhang, H.; Huang, C.; Chen, Z. Y.; Han, A., A Gel-Based Separation-Free Point-of-Care Device for Whole Blood Glucose Detection. *Anal Chem* **2020,** *92* (24), 16122-16129.

170. Yan, J.; Pedrosa, V. A.; Simonian, A. L.; Revzin, A., Immobilizing enzymes onto electrode arrays by hydrogel photolithography to fabricate multi-analyte electrochemical biosensors. *ACS Appl Mater Interfaces* **2010,** *2* (3), 748-55.

171. Guo, J.; Ma, X., Simultaneous monitoring of glucose and uric acid on a single test strip with dual channels. *Biosens Bioelectron* **2017,** *94*, 415-419.

172. Perdomo, J.; Hinkers, H.; Sundermeier, C.; Seifert, W.; Martinez Morell, O.; Knoll, M., Miniaturized real-time monitoring system for L-lactate and glucose using microfabricated multi-enzyme sensors. *Biosens Bioelectron* **2000,** *15* (9-10), 515-22.

173. Christian, N. K.; Olukayode, K.; Fouzan, A.; Catherine, F. T. U.; Anthony, G.-E., Fabrication and in vitro performance of a dual responsive lactate and glucose biosensor. *Electrochim Acta* **2018,** *267*, 71-79.

174. Lin, Y. H.; Wang, S. H.; Wu, M. H.; Pan, T. M.; Lai, C. S.; Luo, J. D.; Chiou, C. C., Integrating solid-state sensor and microfluidic devices for glucose, urea and creatinine detection based on enzyme-carrying alginate microbeads. *Biosens Bioelectron* **2013,** *43*, 328-35.

175. Zhou, F.; Lu, M.; Wang, W.; Bian, Z. P.; Zhang, J. R.; Zhu, J. J., Electrochemical immunosensor for simultaneous detection of dual cardiac markers based on a poly(dimethylsiloxane)-gold nanoparticles composite microfluidic chip: a proof of principle. *Clin Chem* **2010,** *56* (11), 1701-7.

176. Shi, J. J.; He, T. T.; Jiang, F.; Abdel-Halim, E. S.; Zhu, J. J., Ultrasensitive multi-analyte electrochemical immunoassay based on GNR-modified heated screen-printed carbon electrodes and PS@PDA-metal labels for rapid detection of MMP-9 and IL-6. *Biosens Bioelectron* **2014,** *55*, 51-6.

177. Marquette, C. A.; Degiuli, A.; Blum, L. J., Electrochemiluminescent biosensors array for the concomitant detection of choline, glucose, glutamate, lactate, lysine and urate. *Biosens Bioelectron* **2003,** *19* (5), 433-9.

178. Hsiao-chung, T.; Ruey-an, D., Simultaneous determination of renal clinical analytes in serum using hydrolase- and oxidase-encapsulated optical array biosensors. *Anal Biochem* **2004,** *334* (1), 183-192.

179. Rennie, M. Y.; Dunham, D.; Lindvere-Teene, L.; Raizman, R.; Hill, R.; Linden, R., Understanding Real-Time Fluorescence Signals from Bacteria and Wound Tissues Observed with the MolecuLight i:X(TM). *Diagnostics (Basel)* **2019,** *9* (1).

180. Bornhoeft, L. R.; Biswas, A.; McShane, M. J., Composite Hydrogels with Engineered Microdomains for Optical Glucose Sensing at Low Oxygen Conditions. *Biosensors* **2017,** *7* (1), 8.

181. Chen, Z.; Yang, Y.; Yamaguchi, H.; Hung, M. C.; Kameoka, J., Isolation of cancer-derived extracellular vesicle subpopulations by a size-selective microfluidic platform. *Biomicrofluidics* **2020,** *14* (3), 034113.

182. Huang, P. J.; Hwangbo, M.; Chen, Z.; Liu, Y.; Kameoka, J.; Chu, K. H., Reusable Functionalized Hydrogel Sorbents for Removing Long- and Short-Chain Perfluoroalkyl Acids (PFAAs) and GenX from Aqueous Solution. *Acs Omega* **2018,** *3* (12), 17447-17455.

183. Andrus, L. P.; Unruh, R.; Wisniewski, N. A.; McShane, M. J., Characterization of Lactate Sensors Based on Lactate Oxidase and Palladium Benzoporphyrin Immobilized in Hydrogels. *Biosensors (Basel)* **2015,** *5* (3), 398-416.

184. Unruh, R. M.; Roberts, J. R.; Nichols, S. P.; Gamsey, S.; Wisniewski, N. A.; McShane, M. J., Preclinical Evaluation of Poly(HEMA-co-acrylamide) Hydrogels Encapsulating Glucose Oxidase and Palladium Benzoporphyrin as Fully Implantable Glucose Sensors. *J Diabetes Sci Technol* **2015,** *9* (5), 985-92.

185. Ozyilmaz, G.; Tukel, S. S., Simultaneous co-immobilization of glucose oxidase and catalase in their substrates. *Prikl Biokhim Mikrobiol* **2007,** *43* (1), 36-41.

186. Staudinger, C.; Borisov, S. M., Long-wavelength analyte-sensitive luminescent probes and optical (bio)sensors. *Methods Appl Fluoresc* **2015,** *3* (4).

APPENDIX A

OPERATION PARAMETERS FOR INKJET PRINTER

Table A Summary of the settings used in the inkjet printer for silver electrode printing.

Parameter	Nozzle Spacing	Nozzles Activated	Nozzle Diameter	Frequency	Cartridge Size
Value	254 µm	16	21 µm	30 kHz	10 pL
Parameter	Substrate Temperature	Jetting Frequency	Applied Voltage	Drop Spacing	Drop Angle
Value	30 °C	5 Hz	30 V	20 µm	4.4°